INVESTIGATION OF VOLUME DIFFUSION HYDRODYNAMICS: APPLICATION TO TIGHT POROUS MEDIA

Chariton Christou

Submitted for the degree of Doctor of Philosophy

Heriot-Watt University

Institute of Mechanical, Process and Energy Engineering

School of Engineering and Physical Sciences

2017

Declaration of author's rights

The present thesis is the result of the author's original research. It has been composed by the author and has not been previously submitted for examination which will led to the award of a degree.

Chariton Christou

2017

Abstract

Various engineering problems imply rarefied gas flows that rely in the transition and free molecular regimes, e.g., micro and nano devices. The recent expansion of shale gas production where rarefied conditions are found in reservoirs exposed another area of application with a major importance. Continuum based methods like standard Navier-Stokes equations break down in the transition regime and free molecular regime. In order to model such flows discrete methods are usually adopted. Boltzmann equation can theoretically be used to simulate rarefied gas flows. However, complexity of its collision integral limits its applications mostly to simple cases (i.e., one dimension problems). The direct simulation Monte Carlo method which mimics the Boltzmann equation is the dominant method for simulating rarefied gas flows. It has been tested in several engineering problems, ranging from nano scale flow to re-entry vehicles with very consistent results in comparison with experimental data and analytical solutions. Its computational cost is, however, enormous for complex cases. Observations from Crookes radiometer inspired extending the continuum methods so that they could capture non-equilibrium phenomena in small scales. In the present thesis two different hydrodynamic model are presented. The first one is based on the Korteweg expression and the second one is called “Bi-velocity”. Firstly, the two models are presented in their mathematical forms. The proposed models are then developed in open-source computational fluid dynamics solvers. The models are tested and benchmarked in different rarefied gas flows problems in the whole range of Knudsen number. We used problems that are found in micro and nano systems and tight porous media. Results from the hydrodynamic models are compared against experimental data where available and the direct simulation Monte Carlo method. The two extended hydrodynamic models show improved results in comparison with standard Navier-Stokes.

Acknowledgements

First of all, I would like to thank my supervisor Dr S. Kokou Dadzie for his invaluable help during my PhD research for the past 3 years. He was ensuring that I was in the correct path of my research during this period. In addition, he did everything so he could be assuring that I was happy about what I was studying and this was the key for being happy all this time and enjoying my research.

I would like to thank also my university, Heriot-Watt for providing me with all the necessary equipment that was needed to complete a PhD.

Great Alexander said "I am indebted to my parents for living, but to my teacher for living well". My parents Ioannis and Anna are my teachers as well so I indebted to them for living and living well (everything). My nephews, Panayiotis, Anna, Ioanna and the newborn Antonia that I have been missing them while I was living far away from them. I hope that in the next few years I will have more time with them not only to play but to make such unforgettable laughs. To my sisters, Theophano and Christina who were supporting me and waiting until I return for holidays in Greece and Cyprus.

I would like to thank my friend, Andreas Economou, PhD student at UCL for the long discussions during our PhD's. Our everyday discussions regarding our research and plans helped both to bring out the stress that everyone has during the PhD. Special thanks to my friend, Stefanos while he was in Scotland for the everyday discussion after his work. The long talks regarding my research, my plans, my achievements my balance in life and our thoughts about life will be missed.

Last but not least my other half Mrs Smaragda Christodoulou for being next to me every single day and every single minute. Being away from her the last four years was one of the toughest decisions that I ever made. Her help, encourage to continue and patience for all this period was the most crucial. Furthermore, I would like to thank her for reviewing the design of my posters and presentation in the attended conferences around the world, from Qatar to US, Scotland and Canada.

ACADEMIC REGISTRY
Research Thesis Submission

Name*:*	Chariton Christou		
School:	Engineering and Physical Sciences		
Version: *(i.e. First, Resubmission, Final)*	Final	Degree Sought:	PhD

Declaration

In accordance with the appropriate regulations I hereby submit my thesis and I declare that:

1) the thesis embodies the results of my own work and has been composed by myself
2) where appropriate, I have made acknowledgement of the work of others and have made reference to work carried out in collaboration with other persons
3) the thesis is the correct version of the thesis for submission and is the same version as any electronic versions submitted*.
4) my thesis for the award referred to, deposited in the Heriot-Watt University Library, should be made available for loan or photocopying and be available via the Institutional Repository, subject to such conditions as the Librarian may require
5) I understand that as a student of the University I am required to abide by the Regulations of the University and to conform to its discipline.
6) I confirm that the thesis has been verified against plagiarism via an approved plagiarism detection application e.g. Turnitin.

* *Please note that it is the responsibility of the candidate to ensure that the correct version of the thesis is submitted.*

Signature of Candidate*:*	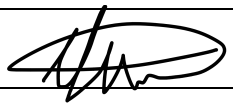	Date:	22/09/2017

Submission

Submitted By *(name in capitals):*	YEAW CHU LEE
Signature of Individual Submitting:	
Date Submitted:	22/09/2017

For Completion in the Student Service Centre (SSC)

Received in the SSC by *(name in capitals):*			
Method of Submission *(Handed in to SSC; posted through internal/external mail):*			
E-thesis Submitted (mandatory for final theses)			
Signature:		Date:	

Contents

List of Figures

List of Tables

Nomenclature

Latin symbols

C_v	Specific heat capacity at constant volume
E_{tr}	Translational Energy
G_m	Dimensionless Mass Flow Rate
J_u	Energetic Heat Flux
k_a	Permeability
k_B	Boltzmann Constant
k_m	Transport Coefficient
$\dot{M}$	Mass Flow Rate
$\dot{N}$	Molecular Flux
$\overline{N}$	Number of DSMC particles
q_{ve}	Entropic Heat Flux
V_{cell}	Cell Volume
$-J_c$	Volume Diffusive Flux
c	Molecular velocity
d	Molecule diameter
F_{ij}	Intermolecular force
f	Velocity Distribution Function
J	Heat Flux Vector
Kn	Knudsen number
L	Computational Domain Length
m	Molecule Mass
Ma	Mach Number
n	Number Density
P	Probability Collision
p	Pressure
Pa	Pascal [kg/m^2]
Pr	Prandtl Number
q	Heat Flux Vector
R13	Regularised 13 moment equations
R26	Regularised 26 moment equations
T	Temperature
t	Time
U	Freestream Velocity

Greek symbols

σ_u	Tangential momentum accommodation coefficient
α	Accommodation Coefficient
β	Material Coefficient
Δt	Time step
θ	Angle, Degree
λ	Mean free path
μ	Shear viscosity
ξ	Fraction
Π	Shear Stress Tensor
ρ	Density
Σ	Sum
σ	Collision cross section
τ	Stress Tensor
Ω	Solid Angle
ω	Dynamic Viscosity index

Subscripts

coll	Collision
g	Gas Conditions
in	Inlet
ref	Reference
rot	Rotational
tra	Translational
vib	Vibrational
w	Wall Conditions

Superscripts

*	Post-collision values

Acronyms

BGK	Bhatnagar-Gross-Krook
CFD	Computational Fluid Dynamics
CL	Cercigianni-Lampis
CLL	Cercigianni Lampis Lord
CPU	Central Processing Unit
DSMC	Direct simulation Monte Carlo method
EIA	Energy Information Administration
ESA	European Space Agency
FIB	Focus Ion Bean
FV	Finite Volume
GPU	Graphic Processing Unit
HPC	High Performance Computer
LB	Lattice Boltzmann
MD	Molecular Dynamics
MEMS	Micro Electromechanical Systems
Micro-CT	Micro Computed Tomography
NEMS	Nano Electromechanical Systems
NS	Navier-Stokes
NSF	Navier-Stokes-Fourier
NTC	No-Time Counter
OpenFOAM	Open Field Operation and Manipukation
SEM	Scanning Electron Microscopy
TCF	Trillion Cubic Feet
VHS	Variable Hard Sphere
VSS	Variable Soft Sphere

Chapter 1

1.Introduction

1.1. Motivation

The aim of the current thesis is to present extended hydrodynamic models that are in pure continuum regime and are able to describe non-equilibrium flows. Continuum assumption is valid when the mean free path of moecules is smaller than the characteristic dimensions of the flow domain [1]. Thermodynamic equilibrium implies that the shear stress is linearly dependent on the rate of strain and the heat flux is linearly proportional to the temperature gradient[2]. The degree of non-equilibrium is described by the dimensionless Knudsen number which will be defined later. The inapplicability of existing continuum methods like the standard Navier-Stokes dates back to the 19^{th} century, when Maxwell studied stresses in rarefied gases[3]. Hilbert identified the need of a continuum model that can describe non-equilibrium phenomena in his 6^{th} problem in a series of mathematical problems [4].
In the current study, we investigate the unconventional behavior of rarefied gas flows. Such problems can be found in cases where the length scale L is comparable to the mean free path λ of the gas molecules. In the area of problems where environmental pressure occurs, we can find problems in nano or micro scales. The use of micro- and nano-electromechanical systems (MEMS/NEMS) has faced rapid increase as it has generated extensive research in fluid flows in ultra-small devices. Gas flows at micro- and nano-scale involve complex processes due to rarefaction, important gas-surface interactions, and inter-molecular collisions [5]. Usually, this is in the scale of some μm. Applications are related, for example, to solid-state hard drive heat transfer, micro-fuel cells, micro-pumps, and micro-turbines. Other applications where rarefied gas flows are found include nano-bridges, speed sensors, accelerometers and vacuum pumps.

In such applications the standard continuum model, the Navier-Stokes set of equations, cannot accurately predict the gas behaviour. The failure of the continuum models starts when the heat flux and shear stress in the conservation of energy and momentum respectively can no longer be characterized by the macroscopic magnitude. Even with velocity slip and temperature jump boundary conditions the standard continuum method does not always accurately capture non-equilibrium flows.

The use of statistical method starts with the kinetic theory of gases as represented in the Boltzmann equation that the famous Austrian physicist derived in 1872 [6]. Collisionless form of the Boltzmann equation is usually used in cases where the gas is in the free molecular regime. The study of rarefied gas requires also investigation of the interaction between the gas molecules and surrounding solid surface which is another area of research on its own. The Boltzmann kinetic equation should be accompanied with these boundary conditions. First numerical simulations regarding the Boltzmann equation appeared in late 1960s[7]. This was due to the rapid expansion of the aerospace industry. The Boltzmann equation became a practical tool through the direct simulation Monte Carlo (DSMC) method for aerospace engineers in order to further investigate the problem in the upper atmosphere when there is a decrease in the ambient density with increasing height. The increase of height was followed with an increase of the speed and a peak in heat. Applications of these simulations have been applied to the Columbia space shuttle disaster in 2003 [8].

It is widely accepted that in order to describe rarefied gas flows, discrete methods should be adopted. On the other hand, such methods are computationally intensive (and expensive) and even if they can be used in complex geometries, the need of High Performance (HPC) computer is required. Several extended hydrodynamics equations have been proposed in order to achieve consistent results and reduce dramatically the computational cost. Higher-order models such as Grad's moments method [9], Burnett and super-Burnett [10], R13 [11, 12] or R26 [13]. Such models are able to describe rarefied gas flows and non-equilibrium effects in the case of nano-cavity for a $Kn < 0.1$. Comeaux *et al*. [14] showed that Burnett equations can violate the second law of thermodynamics and this finding may account past attempts to solve the Burnett equations. In addition, these models suffer from instability problems when using linearized stability analysis [15]. Garcia-Colin et al [16] claim that these problems with the Burnett equations are in reality limitations of those methods and they highlighted the need of better theories. Poisson [17], Maxwell [3], Gibbs [18] and Van der Waals [19] observed that fluid interface actually represents a rapid but smooth transition of physical quantities between the bulk fluid values. Van der Waals

proposed gradient theories for the interface based on thermodynamic principles and developed his idea that the interface has non-zero thickness and it is diffuse. He stated his theory of the interface based on his equation of state in order to predict the thickness of the interface. Based on this, Korteweg [20], proposed a model for transition phenomena in fluid mechanics by incorporating in the stress tensor the gradient of density ρ. Among other attempts are the extensions of higher-order models [21, 22]. Brenner firstly proposed the Volume Diffusion (or Bivelocity) theory [23] based on the thermophoresis phenomenon [23] and showed the existence of two different velocities. Brenner introduced the volume velocity. The Bivelocity fluids incorporates the mass and the volume velocity while the monovelocity fluids obey the Navier-Stokes-Fourier (NSF) equations. The Volume Diffusion equation model can also be viewed as extension to the Navier-Stokes.

The recent developments in petrochemical industry and shale and tight gas reservoirs have generated a new area of research as applied to rarefied gases. According to the Energy Information Administration (EIA) the unproved technically recoverable resources of tight and shale gas on planet Earth are estimated as 7577 trillion cubic feet (tcf). Conventional gas reservoirs consist of pore size in the range of 1 to 100 micrometers where shale gas reservoirs can have pores in the range of 1 to 200 nanometers [24]. Micropore can be classified as pores with diameter less than 2 nm and mesopore as pores with diameter less than 50 nm [25]. Pore networks in unconventional gas reservoirs consist of pore networks from mineral matrix and organic matter. Mineral matrix pores vary from nanoscale to microscale (10nm – 100 μm) whereas the organic matter relies only in nanoscale (10 – 750nm). Due to the existence of pores with several multitudes of sizes, transport processes in these types of reservoirs are complex processes at micro (10^{-6} m) to nano-scale (10^{-9} m) [26]. Unconventional gas reservoirs have pressures in the range of 1 – 100 MPa [27]. Under those pressures and pore sizes the mean free path (λ) is comparable to the characteristic length of the pore and the gas is often in rarefied regime [5, 28]. Darcy's Law, which was concluded from experiments and derived from continuum methods (Navier-Stokes equations), is no longer valid without any slip modification [29-32].

In the present thesis, we will consider gas flows mainly in the transition and free molecular regime which can be characterized as dilute gases. We describe the dominant methods for simulating rarefied gases, discrete methods, and develop new hydrodynamics models. The new hydrodynamics models been implemented in an open source code using C++ in the OpenFOAM framework. The new developed codes are an actual extension on the compressible Navier-Stokes solver in OpenFOAM, called *rhoCentralFoam*. The main solver which follows the Volume Diffusion theory is called *HWrhoCentralFoam* taking the

initials of our current university and *CCrhoCentralFoam* for the Korteweg model. The rest of the thesis provides with the fundamentals of rarefied gas dynamics and several test cases that the Volume Diffusion (or bi-velocity) theory has been tested on.

1.2. Rarefied Gas Dynamics

Rarefied gas dynamics can be defined as the study of gas flows in which the average distance between two subsequent collisions of a molecule (mean free path, λ) is comparable to the typical length (L) of the structure of the flow that is being considered. The Knudsen number (Kn) is introduced in order to characterize the degree of rarefaction and it is defined as the ratio of the molecular mean free path (λ) to the characteristic length of the flow:

$$Kn = \frac{\lambda}{L} \tag{1.1}$$

Rarefied gas flows can be modelled by different methods depending on the flow regime. The first classification of the different flow regimes has been made by Tsien depending to the degree of rarefaction [33]:

- For Kn < 0.001: *Continuum regime*
- For 0.001 ≤ Kn ≤ 0.1: *Slip regime*
- For 0.1 < Kn ≤ 10: *Transition Regime*
- For Kn > 10: *Free molecular regime*

Continuum Regime: In the continuum flow regime, the number of collisions is high enough and the well-known Navier-Stokes set of equations can be used. The conventional no-slip boundary condition is considered to be valid since the flow in such occasion is in local thermodynamic equilibrium. Discrete methods are prohibited in such regime due to the intermolecular collisions which can lead to huge computational time that is required.

Slip Regime: As the Knudsen number increases and becomes significant the gas surface interactions become less frequent and a layer in the order of one mean free path (λ), the

well-known Knudsen layer starts to form near the surfaces. The Knudsen layer cannot be studied with the standard Navier-Stokes and new methods such as the Boltzmann equation should be adopted. This non-equilibrium phenomenon (rarefaction effect) are accompanied by velocity slip and temperature jump at the walls. The gas velocity (U_g) and temperature (T_g) have different values than the surface values (U_s and T_s). The NSF can be extended in this regime by using the Maxwell's velocity slip [3] and Von Smoluchowski's temperature jump boundary conditions [34]. In this regime, we find micro gyroscope accelerometer, flow sensors, micro nozzles and tight gas reservoirs as the pore diameter decreases.

Transition Regime: This regime can be characterized as the most difficult regime for modeling and describing the flow and it attracts most of the research in our days. In the transition regime, the NSF equations are no longer valid and alternative methods should be adopted. The constitutive laws that define the stress tensor and heat flux are those that particularly break down and corrections (or extended hydrodynamics) are required. These extended hydrodynamics models equations are usually derived from the Boltzmann equation based on the Chapman-Enskog expansion of the velocity distribution function, f. The Boltzmann equation can also be used in this regime since is valid at microscopic level. However, it is difficult to obtain an exact solution of the Boltzmann equation due to the non-linear nature of the collision integral. The direct simulation Monte Carlo (DSMC) method offers an alternative way of solving the Boltzmann equation indirectly [35]. DSMC is the dominant method for solving problems in the transition regime. In the transition regime, we usually find applications such as hard disk drive and unconventional gas reservoirs where the mean free path (λ) becomes comparable to the characteristic length of the flow domain (L).

Free Molecular Regime: In this regime, intermolecular collisions are rare and the mean free path is very large compared to the characteristic length of the flow system. The collision-less form of the Boltzmann equation is used as continuum fluid models fully break down. In this regime, the collision integral can be neglected and the Boltzmann equation can be solved. In this regime, we regularly find applications in the aerospace industry and planetary science. The DSMC can also be used.

1.3. Kinetic Theory of Gases and Boltzmann Equation

Kinetic theory of gases uses statistical based methods to describe dilute gas. Using probability theory and statistical mechanics it presents the gas properties using microscopic

interactions and collisions between molecules. The molecular collisions are considered always as binary collision in the kinetic theory of gases since the gas is dilute and it very unlikely that in a single collision event, three or more molecules will be involved. Using the probability theory, it calculates macroscopic phenomena and values from the dynamic of molecules at a microscopic level [35].

Starting by using classical Newtonian mechanics, the equations that describe the motion for all in a system can be expressed as:

$$m\frac{d^2r_i}{dt^2} = \sum_{\substack{j=1 \\ j\neq i}}^{N} \mathrm{F}_{ij,} \tag{1.2}$$

where m is the mass of a single molecule, r_i is the position of that certain molecule. $\mathbf{F}_{ij}$ represents the forced imparted in molecule i by molecule j. Like in the molecular dynamics (MD) technique which is a deterministic technique, the above equation is solved. Despite the new advances in high performance computers (HPC) and the use of parallelization techniques, MD are restricted in small scales and the time steps are often restricted to femtoseconds. The main objective is to use probability theory together with averaging methods in order to obtain the macroscopic properties from microscopic data. In order to reduce the statistical noise there should be sufficient number of particles where the properties are being calculated from. It should be noted that dilute gas systems is usually assumed that all of the molecule energy is fully kinetic (ideal gas). Even though the kinetic theory can describe polyatomic gases and mixtures, the internal degrees of freedom dramatically increase and this makes the model extremely complex and infeasible to be solved.

The dilute gas approximation in conjunction with the molecular chaos along with the kinetic theory lead scientists to the formulation of the Boltzmann equation which starts from the Liouville theorem.

First, Maxwell in 1859 introduced his model of distribution of molecular velocities and he showed that a certain number of molecules have particular velocity within a specific range [36]. The Maxwell theory is generalized and called nowadays Maxwell-Boltzmann distribution. Several properties can be obtained from the Maxwell-Boltzmann distribution. Figure 1.1 illustrates the Maxwell-Boltzmann molecular speed distribution of oxygen at two different temperatures, 173K and 300K.

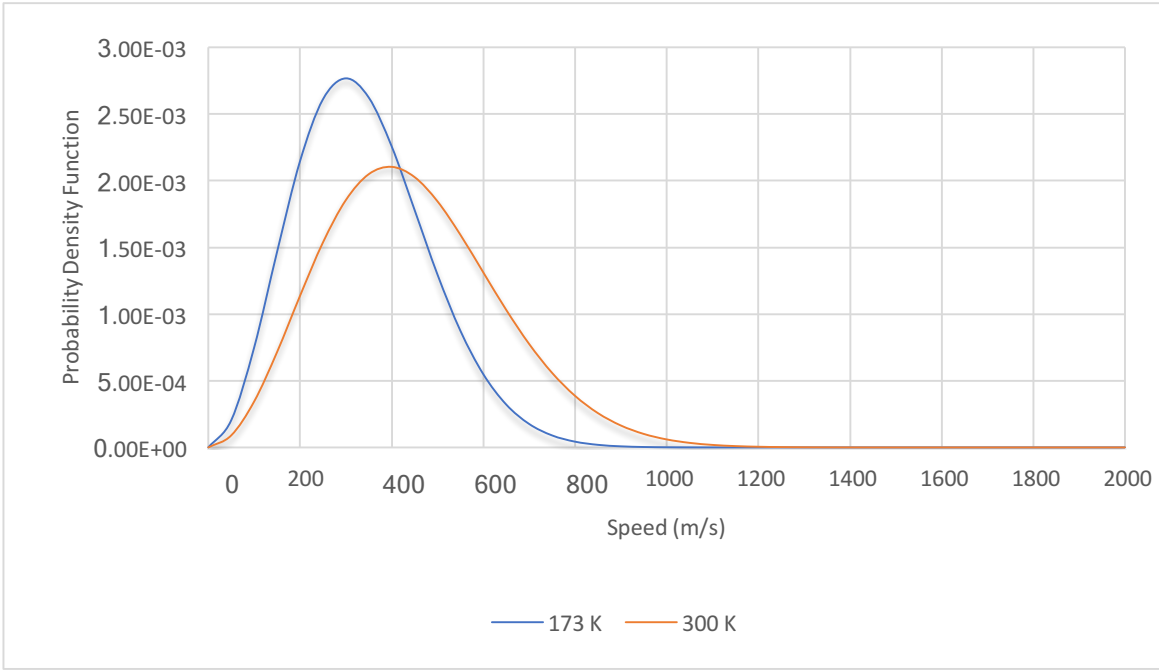

Figure 1-1: Maxwell-Boltzmann molecular speed distribution for oxygen gas

Starting from the Liouville equation, which is fundamental in statistical mechanics the Boltzmann equation is derived. In principle, the Liouville theorem is six-dimensional space equation where three coordinates describe the velocity-space and three coordinates describe the location in physical-space. The Boltzmann equation for a single species and monoatomic gas can be written as follows:

$$\frac{\partial(nf)}{\partial t} + c\frac{\partial(nf)}{\partial r} + F\frac{\partial(nf)}{\partial c} = \int_{-\infty}^{\infty}\int_{0}^{4\pi} n^2\,(f^* f_1^* - f f_1) c_r \sigma \mathrm{d}\Omega \mathrm{d}c_1 \qquad (1.3)$$

Where f is the velocity distribution function, n is the number density, F is the external body force, r and c are the position and velocity vectors respectively. The subscript * indicates the post-collision values and f, f_1 are distribution function of two different types of molecules (c,c_1), σ is the collision cross section and Ω is the solid angle. The Boltzmann equation can be employed to describe flows in all flow regimes. If the assumption of binary collisions and molecular chaos are met the equation can be used. Although the Boltzmann equation is valid for all Kn numbers it is enormously expensive to solve numerically even with the new capabilities with modern computers because of the non-linearity of the collision integral. In order to facilitate analytical solutions, simplified models for the collision integral are often proposed. Among these models is the Bhatnagar, Gross, Krook (BGK) model. Within the Boltzmann equation two prerequisites should kept in mind: Firstly, the fact that it is available only for dilute gas and only for binary collisions. During

collisions between molecules of class c and class c_1, the distribution function f of molecules of class c has been assumed to be uncorrelated with the distribution function f_1 of class c_1 [5]. The above equation is for single component or monatomic gas. However, in nature most of the gases are polyatomic gases where there is exchanges of translational and internal energies and more transport coefficients need to be introduced. Boltzmann equation is used for low Mach number flows and simple geometries. The first or the second (even the third) approximation of Chapman-Enskog expansion can be employed in order to solve the Boltzmann equation [37]. The first order approximation corresponds to the standard NSF set of equations. The second order approximation is the complex non-linear Burnett equations. The third order approximation is called super-Burnett equations. The Burnett and super-Burnett aim to be valid in the transition regime and extend the continuum fluid like models. However, there are concerns that higher order Burnett equations are not thermo-mechanically consistent and violate thermodynamic principles.

1.4. Unconventional Gas Resources

According to the U.S. Energy Information Administration (EIA) data the production of shale and tight gas consists more than 40% of the U.S natural gas production. As it can be seen in Figure 1.2 the production of shale and tight gas is expected to reach 55% by 2040. It is estimated that in the U.S the reserves from shale gas are estimated to be 500 – 1000 trillion cubic feet (tcf) [38]. Previous works have shown that production from source or cap rocks can be economically substantial.

The substantial amount of natural gas that can be found in tight and shale gas formations has enhanced research about transport phenomena occurring in such porous medium. Most of the gas production from such formation occurs in the source rock where low permeable formations are usually found [39].

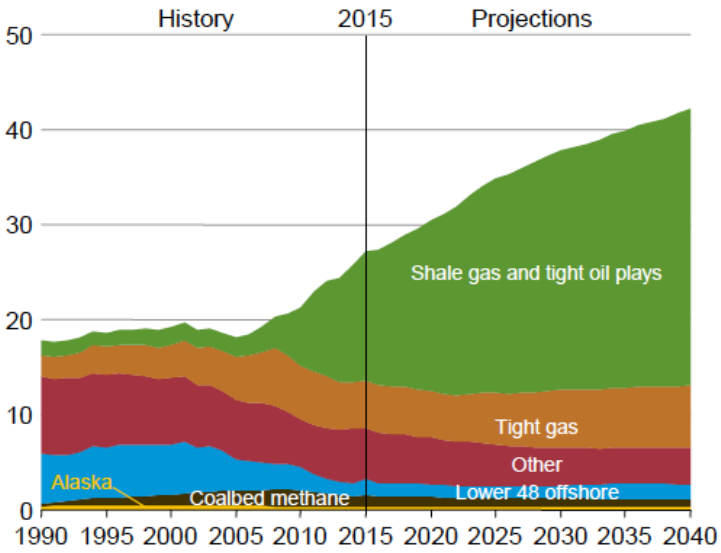

Figure 1-2: US dry natural gas production (projected)

Flow and recovery mechanisms in shale and tight gas reservoirs can be substantial different from those that occur in conventional gas reservoirs. Shale and tight gas reservoirs are usually ultra-tight rocks with relatively low pore connectivity and extremely low permeability. Pore sizes in shale matrix usually ranges from some nanometres to several hundreds of nanometres and under such conditions the pore sizes are comparable to gas mean free path. Unconventional gas reservoirs for example, can exhibit multi-mechanism flow which can be a combination of Darcy flow, Knudsen diffusion and the so called Klinkenberg effects [40].

In order to improve the production from shale and tight gas reservoirs it is crucial to understand the gas flow mechanisms. Under conditions that exhibit in shale and tight gas reservoirs the flow is often in the slip flow and transition regime where standard Navier-Stokes equations fail. This will be further discussed in the next Chapter.

1.5. Project Objectives

The objective of the current project is to develop continuum based methods that are able to describe gas flows in all rarefied flow regimes. In this work, the developed hydrodynamic models are compared with experimental data and other discrete methods that are widely used in order to describe rarefied gas flows. A detailed analysis, is performed on the proposed models in order to assess their ability to capture non-equilibrium phenomena in the whole range of Knudsen number.

In the present study, the incompleteness of the standard continuum based Navier-Stokes equations to describe rarefied gas is presented through several problems. These serve as the basis of the need for new continuum based methods.

The direct simulation Monte Carlo (DSMC) method is the dominant way to describe rarefied gas flows in our days. However, the computational cost of this method is extensively high and it restricts its application up to the transition regime. In our research, DSMC will serve as a benchmark way for the new hydrodynamic models.

The objectives of the thesis are to develop and benchmark on the free open source Open Field Operation and Manipulation (OpenFOAM) package the proposed extended hydrodynamics models. The new codes are tested against existing experimental data, analytical solution and results from other discrete methods, like the DSMC. In this work, the codes are tested for micro- and nano-structures where non-equilibrium effects dominate the flow. We fully present all the numerical results obtained from the proposed models in various configurations in nano and micro devices.

1.6. Key Developments

The proposed models are developed in a C++ Computational Fluid Dynamics (CFD) solvers in the OpenFOAM framework. In the OpenFOAM framework the solver for solving compressible flow based on Navier-Stokes-Fourier is called *rhoCentralFoam*. The solver was developed by Greenshields *et al.* back in 2009 [41]. This solver will serve as the basis for the extension in the continuum theory. The two proposed solvers will allow us to compare them with the *rhoCentralFoam* and DSMC method in order to find out their ability to describe non-equilibrium flow. The first solver is based on the Korteweg model. Beside the Korteweg model, a new model that is based on Volume Diffusion (or Bi-velocity) theory is presented in its theoretical manner and developed as extension to *rhoCentralFoam*. Each solver involves new velocity slip and temperature jump boundary conditions respectively. These new developments enable the application of such problems in micro geometries where MEMS and NEMS problems are usually found. The DSMC method is used to benchmark the new solvers. In addition, the DSMC is used for several different cases that are outlined below.

In more detail, the main contributions of this work are:

a) Use for the first time DSMC along with micro-CT images and simulate rarefied gas flows in unconventional gas reservoirs. The use of such method (micro-CT) can generate a new area of research not only for tight gas reservoirs but for planetary science in order to study gas flows through comet nucleus.

b) Development of a CFD solver in the OpenFOAM framework as an extension to the *rhoCentralFoam*. The solver is based on the volume diffusion (or bi-velocity) hydrodynamics and named *HWrhoCentralFoam* from the initials of Heriot-Watt University.
c) Development of a CFD solver based on the Korteweg fluid like model as an extension of standard Navier-Stokes equations. The solver is named *CCrhoCentralFoam*
d) Benchmark of *HWrhoCentralFoam* against DSMC and standard Navier-Stokes in lid-driven micro- cavity in a rarefied regime.
e) Benchmark of *HWrhoCentralFoam* against Navier-Stokes-Fourier in a mixed-convection problem.
f) Comparison of *HWrhoCentralFoam and CCrhoCentralFoam* against experimental data and analytical solutions mass flow rate in a micro-channel in the whole range of Knudsen number.
g) Development of new boundary conditions based on the Maxwell and Smoluchwski boundary conditions, in order to incorporate the new terms that have been added in the *HWrhoCentralFoam* and *CCrhoCentralFoam*.

1.7. Thesis Outline

In Chapter 2 we describe in detail the direct simulation Monte Carlo (DSMC) method which is the dominant method for simulating rarefied gas flows. The results that are obtained with our new volume diffusion (or bi-velocity) model are compared with the DSMC and with experimental data where these are available. In this chapter, the equations and methodology that DSMC uses to obtain macroscopic gas properties is also described in detail.

The application of rarefied gas dynamics in porous media is of great interest and we describe the current challenges that the oil & gas industry is facing nowadays. The application of DSMC in porous media is investigated in Chapter 3. The application of DSMC was achieved by obtaining the porous structure with micro-CT imaging tool. The methodology of micro-CT is briefly described as it offers a great tool for applying discrete and hydrodynamics methods in porous media.

In the next chapter, we perform an in-depth description of the volume diffusion and generally in hydrodynamics continuum models that have been developed during the past years. The development of the solvers in the OpenFOAM is extensively described.

Chapter 5 is used as a benchmark of our new compressible solvers and application of the volume diffusion theory and Korteweg model micro scale problems. A micro cavity case is tested and evaluated between NSF, DSMC and volume diffusion. In addition, a mixed-convection case is also evaluated against the standard NSF. Finally, the volume-diffusion is tested against experimental data of mass flow rate in a micro-channel. The application of analytical solutions that arise from the volume-diffusion theory for predicting permeability of tight gas porous media are explained and offer an alternative area of applying this method.

The key findings from the current research are discussed in Chapter 6. The results enabled the discussion about the future work that can be done based on the observations.

1.8. Published Papers

In the present thesis, the papers below have been published or submitted for publication in peer reviewed journals and conferences:

1. Chariton Christou. and S.Kokou Dadzie, "Numerical Simulations of Rarefied Gas-Flows in microchannels". *Physical Review Fluids, Submitted*

2. Chariton Christou, and S. Kokou Dadzie. "An Investigation of Heat Transfer in a Cavity Flow in the Noncontinuum Regime." *Journal of Heat Transfer*139.9 (2017): 092002.

3. S. Kokou Dadzie and Chariton Christou, Bi-velocity gas dynamics of a micro lid-driven cavity heat transfer subject to forced convection. *International Communications in Heat and Mass Transfer*, 2016. **78**: p. 175-181.

4. Chariton Christou, and S. Kokou Dadzie. "Direct-simulation Monte Carlo investigation of a Berea porous structure." *SPE Journal* 21.03 (2016): 938-946.

5. Chariton Christou and S. Kokou Dadzie, 2016, July. Effects of volume diffusion in heat transfer in a cavity flow in non-continuum regime. *Proceedings of the 30th International Symposium of Rarefied Gas Dynamics: AIP Conference*

6. S. Kokou Dadzie and Chariton Christou, 2016, July. An investigation of Mixed-Convection in a Rarefied Gas. *Proceedings of the 30th International Symposium of Rarefied Gas Dynamics: AIP Conference*

7. Dadzie, S.K., Tubby, W.G. and Christou, C., NEGF2015/5 Investigation of various permeability laws in tight porous media.

8. Chariton Christou and S.Kokou Dadzie, 2015, February. Direct Simulation Monte Carlo Method in Porous Media with Varying Knudsen Number. In *SPE Reservoir Simulation Symposium*. Society of Petroleum Engineers.

Chapter 2

2.The direct simulation Monte Carlo method

In this chapter, we briefly describe the direct simulation Monte Carlo (DSMC) algorithm and its possible applications in different type of problems. The aim of the chapter is to illustrate the importance of the DSMC method. Capabilities and areas of applications of the DSMC method are discussed.

2.1. DSMC Method

DSMC was invented by Graeme A. Bird in 1963 [42]. The method is based on the kinetic theory of gas (subject to the molecular chaos). It does not aim to solve the Boltzmann equation directly but to mimic it. DSMC and Boltzmann equation are based on the same physical principles. In other words, the Boltzmann equation plays a fundamental role in the origin of DSMC. The molecular collisions are considered in a probabilistic way rather than deterministic. A simulated particle represents a number of real gas molecules. This belongs to the concept of molecular dynamics, which their concept is to simulate in particle level, but to restrict the number of molecules to a tractable figure. The number of simulated particle should be large enough so as to represent the global distribution of the real gas molecules. On the other hand, at the same time the number of simulated particles should be kept small enough in comparison to the real number of molecules. This is used in order to reduce the computational time of the simulations and in order to be able to run on the most advanced computers. It is stochastic particle-based method and the basic concept of it is to track every simulated particle in time and space and at the same time modifying its velocity components and position coordinates which are stored in memory through their

collisions and interaction with boundaries. Beside the fact that each simulated particle can represents a real number of molecules, another advantage of DSMC over molecular dynamics (MD) is that it can treat particle collision stochastically rather than deterministically.

The DSMC method is based in the sense that the particle motion and intermolecular collisions are decoupled over discrete time steps of magnitude Δt. During a step Δt, each simulated particle travels a certain distance based on its velocity and then collision with another particle is executed. The time step should be small enough in respect to the mean free time, which can be defined as the average time between two subsequent collisions of a single molecule. The computational mesh is required, as in standard computational fluid dynamics (CFD) methods to perform near-neighbour collisions and to get the macroscopic properties. The flow field is divided into cells with linear size of Δx. The size of Δx should be small in comparison with the mean free path and it should be kept in general smaller than $\lambda/3$ [43]. The way that the collision pairs are chosen and how many of them are taking action is a key issue in ensuring the consistency of the method. The cells of it can be easily adapted to any geometrical shape and it can be applied in a variety of complex geometries (i.e porous medium).

DMSC becomes popular during the 1970s due to an experimental verification obtained for a space shuttle in the transition regime [44]. In more detail, Bird used the DSMC to study the shockwave structure not only in single species but in gas mixtures as well [45]. The introduction of the Larsen-Borgnakke [46] model which restricts energy transfer in an inelastic collision between translational and rotational model which added later offered another option when dealing with polyatomic gases collisions. In order to simulate realistic collision rates, and keep the computational level in a minimum level the no-time-counter (NTC) technique along with a sub-cell method are used and they become the standard approaches in DSMC [35, 47]. In this scheme, a particle pair is selected randomly within each cell, or within sub-cell regardless particles positions. Then, an acceptance-rejection procedure is followed. In the acceptance case a collision is performed between particles. In the case of rejection, a new particle pair is selected and this procedure (acceptance-rejection) is repeated until the required number of candidate pairs in a selected cell at the set time step has been selected. This indeed improves the accuracy of the DSMC by incorporating the collisions of particles with one other. In 1966 an experiment was performed of the shock wave problem for obtaining the molecular velocity distribution. The results were not published since they proved to be inconsistent with that time (1966) theoretical results. However, after 23 years (1989) these results get compared with DSMC

simulations and proved to be consistent [48]. That verification gave the DSMC the recognition. Along the most important challenges that DSMC faced was the scepticism regarding the relationship of it with the Boltzmann equation and if it does really solve it. In 1992 Wanger proved mathematically the convergence between DSMC and Boltzmann equation when he compared these two methods for a monoatomic gas in limiting case.
DSMC can be characterized as a highly intensive method due to the need to track large number of particles and at the same time compute and store large number of collisions. Another important aspect is that in order to reduce the statistical scatter (or noise) a large number of time steps are required. Parallelization techniques can be used to reduce the computational time. Modern computing platforms, like High Performance Computers (HPC) can work with this method and reduce the computational time dramatically. Recently, a GPU (Graphics Processing Unit) code [49] has been developed and proved that the computational time can be reduced reasonably in comparison with a CPU code.

2.2. DSMC Algorithm

A DSMC simulation begins by dividing the flow field into several cell meshes by meeting the $\lambda/3$ criterion. The time step, Δt, is set next smaller than the mean collision time. The next step is to impose the simulated particles and the number of real molecules that each DSMC particle represents. The molecular properties of the gas are then set by defining the molecular mass, m, the macroscopic density, temperature, T, and velocity that will be used to calculate the initial thermal velocity (from the Maxwell-Boltzmann distribution) at the set temperature for the DSMC particles. The next step is the selection of the intermolecular collision model between the Variable Hard Sphere (VHS), the Hard Sphere (HS) and the Variable Soft Sphere (VSS). The last part is to set the gas-surface interaction model, which can be selected, from a variety of available models. Figure 2.1 represents the basic flowchart (algorithm) that is being followed in a typical DSMC solver. This can be summarized in four steps: 1) move particle over the Δt time step; 2) apply the boundary conditions by introducing new particles at inlet boundaries, removing them from outlet boundaries and processing them for reflections with solid boundaries; 3) sort particles into the computational mesh and calculate the intermolecular collisions; 4) sample the average particle information.

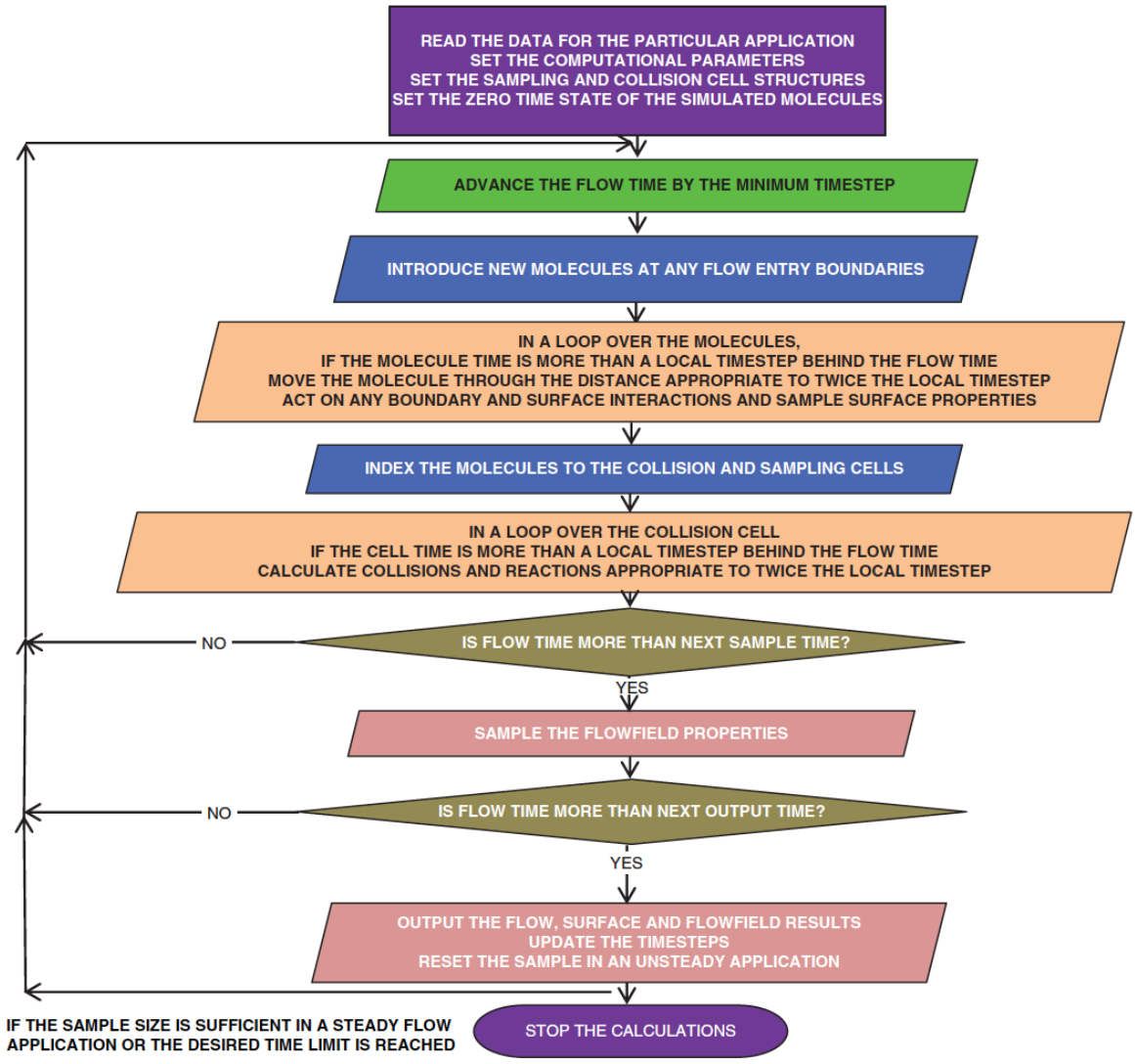

Figure 2-1 DSMC algorithm flowchart

Particle Movement

The first of part of the simulation (algorithm) is to move a particle, i through the distance that is being determined by its velocity c_i and the time step Δt. The new position is being calculated by the equation:

$$r_{i,new} = r_{i,old} + c_i \Delta t \tag{2.1}$$

The particles are inserted at the inflow boundaries and interactions with the boundaries are dealt within this step. There are three different types of boundary conditions model that are commonly used in DSMC. The first one deals with the flow particle across the inlet to obtain the desired freestream conditions.

At the inlet, the particles are inserted based on the equilibrium Maxwellian number flux (molecular) across a boundary $\dot{N}_{in}$:

$$\dot{N}_{in} = \frac{n_{in}}{\beta(2\pi^{\frac{1}{2}})}\left[\exp(-s^2 cos^2\theta) + \pi^{\frac{1}{2}} cos\theta(1 + \mathrm{erf}(s\, cos\theta))\right] \tag{2.2}$$

With

$$\beta = \left(\frac{m}{2k_B T_{in}}\right)^{1/2} \tag{2.3}$$

and

$$s = c_{0_{in}}\beta \tag{2.4}$$

where the subscript *in* denotes the properties at the inlet, n is the number density, θ is the angle between the velocity vector $c_{0_{in}}$ and the inlet. Where k_B is the Boltzmann constant and T_{in} is the inlet temperature. The outlet procedure consists in deleting the particles that leave the system.

In 1879 Maxwell proposed the first gas-surface interaction model for the kinetic theory of gases [50]. In this type of model a gas-surface interaction can be treated as specular or diffuse. When we have specular reflection, the surface is perfectly smooth and elastic. The particle velocity (normal to the surface) is reversed and those that are parallel to the surface remain unchanged. The diffuse reflection represents a microscopically rough surface. The velocity component is reset and the post-interaction velocity is not related with the pre-interaction velocity. The post-interaction velocity is calculated based on the thermal equilibrium with the surface temperature and the direction of velocity is sampled from Maxwellian distribution with equal probability to all directions. In the case of a diffuse model, the user should have specified the accommodation that is required (Fig.2.2a)

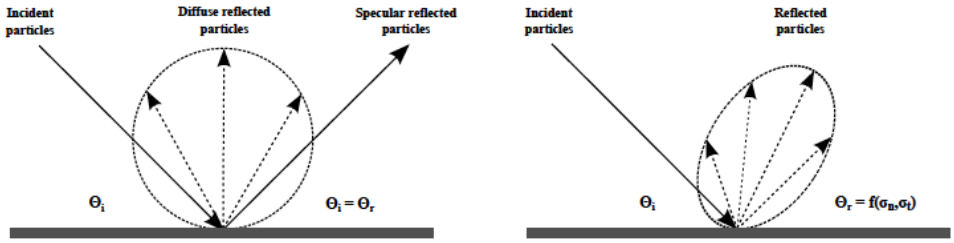

(a) (b)

Figure 2-2 (a) Maxwell's diffuse and specular gas-surface interaction models and (b) Cercignani-Lampis-Lord gas-surface interaction model

Cercignani and Lampis (CL) in 1971 [51] proposed a new kinetic model for gas-surface interactions. The CL model is based on the definitions of α_n and α_t which are accommodation coefficients for the kinetic energy and are associated with the normal and tangential components of velocity. As it can be observed from the Fig.2.2b, the reflect angle is function of the incoming particle angle. This model is quite simple and it has been used extensively. In 1991 Lord applied the Cercignani Lampis model to the DSMC simulations [52]. He also extended the model in order to have the ability to have diffuse reflections with incomplete energy accommodation and to account rotational and vibrational energy exchange at the surface. The model took its final form and applied to DSMC by taking the name Cercignani-Lampis-Lord (CLL) model.

Particle Collisions

Particles that are removed from the domain through the boundaries need to be re-inserted before the intermolecular collisions start. Collisions are treated probabilistically. The intermolecular collisions pairs are selected within the same cell. The sub-cell method can also be used in order to perform the intermolecular collisions in the same cell. Bird's NTC scheme is the standard approach to perform the correct number of collisions. Particle *i* is chosen in random order (from all available particles) in the current cell and another particle *j* is chosen from the same cell to ensure neighbour collisions. Each pair is tested and the collision is accepted when:

$$\frac{(\sigma c_r)_{ij}}{(\sigma c_r)_{max}} > R_f \tag{2.5}$$

where R_f is the random fraction which can take values between 0 and 1 and σ is the maximum product of collision cross-section and c_r is the relative speed between the pair . The probability of a collision to occur in the cell is given by:

$$P_{coll} = \frac{\sigma c_r}{(\sigma c_r)_{max}} \tag{2.6}$$

The NTC scheme is then used in order to achieve the correct collision rate. The number of possible collision pairs to be selected in a cell with N simulated molecules over the time step Δt is as follows:

$$\frac{1}{2N(N-1)F_N}(\sigma c_r)_{max}\Delta t/V_{cell} \tag{2.7}$$

where F_N is the number of real gas molecules that the DSMC particle represents and V_{cell} is the volume of the cell.

If we consider intermolecular collision (a collision between two molecules) with mass m_i and m_j with velocities c_i and c_j respectively. The conservation of mass and momentum requires that:

$$m_i + m_j = m_i^* + m_j^* \tag{2.8}$$

and

$$m_i c_i + m_j c_j = m_i^* c_i^* + m_j^* c_j^* \tag{2.9}$$

Where m^* and c^* denotes the post-collision mass and velocity component respectively.

For elastic collisions, the centre of mass velocity can be defined as:

$$c_m = \frac{m_i c_i + m_j c_j}{m_i + m_j} = \frac{m_i {c_i}^* + m_j {c_j}^*}{m_i + m_j} \tag{2.10}$$

and we know that:

$$c_r = c_i - c_j \text{ and } {c_r}^* = {c_i}^* - {c_j}^* \tag{2.11}$$

The pre-collisions velocities can be obtained by combining equations (2.9) and (2.10):

$$c_i = c_m + \frac{m_j}{m_i+m_j}c_r \quad \text{and} \quad c_j = c_m - \frac{m_i}{m_i+m_j}c_r \tag{2.12}$$

and the post-collision velocities are:

$$c_i^* = c_m + \frac{m_j^*}{m_i^* + m_j^*} c_r^* \text{ and } c_j^* = c_m - \frac{m_i^*}{m_i^* + m_j^*} c_r^* \tag{2.13}$$

When considering the translational energies associated with the collision we define the pre-collision translational energy as:

$$E_{tr} = \frac{1}{2m_i c_i^2} = \frac{1}{2\left(m_i + m_j\right)c_m^2} + 1/2 m_r c_r^2 \tag{2.14}$$

The centre of mass velocity is unchanged so the post-collision translational energy is:

$$E_{tr}^* = \frac{1}{2{m_i}^* {c_i^2}^*} = \frac{1}{2\left({m_i}^* + {m_j}^*\right){c_m^2}^*} + 1/2 {m_r}^* {c_r^2}^* \tag{2.15}$$

It should be noted that in case of chemical reactions the post-collision reduced mass may differ from the pre-collision value.

Sample flow properties

DSMC is a particle-based method and usually engineers are interested in macroscopic flow properties rather than the microscopic. The macroscopic flow properties are recovered in DSMC by statistical averaging of the microscopic data after all collisions have been processed. For simplicity, we restrict the discussion in this section to monoatomic gas where no chemical reactions are taking place. To calculate the macroscopic properties, the cell system is used. The method takes into account that each simulated particle represents a real number of molecules. We start from the number density

$$n = \frac{F_N \overline{N}}{V_{cell}} \tag{2.16}$$

Where, F_N is the number of real molecules in the system and $\overline{N}$ is the average number of DSMC particles in the cell.

The mass density of ρ is defined as:

$$\rho = nm \tag{2.17}$$

where m is molecular mass. The macroscopic velocity that is noted as c_0, or $\boldsymbol{u}$ can be denoted as the mean value of the particle velocities,

$$\boldsymbol{u} = c_0 = \frac{\sum_{i=1}^{N} c}{N} \tag{2.18}$$

The thermal or peculiar velocity $\boldsymbol{c}'$ is defined as:

$$c' = c - c_0 \tag{2.19}$$

The pressure tensor **p** is:

$$\mathbf{p} = \rho\overline{c_i' c_j'} \tag{2.20}$$

The velocity components in x, y and z directions represented by u, v and w respectively

$$c_1' = u', c_2' = v', c_3' = w' \tag{2.21}$$

The macroscopic pressure scalar P is defined as the average value of the three normal components

$$P = 1/2\rho(\overline{u'^2} + \overline{v'^2} + \overline{w'^2}) \tag{2.22}$$

The viscous stress tensor τ is computed from the negative of the pressure tensor

$$\tau = -(\rho\overline{c_i' c_j'} - p) \tag{2.23}$$

The translational temperature which for a monatomic gas equals the overall temperature is defined by:

$$T_{tra} = \frac{1}{3k_b} m(\overline{u'^2} + \overline{v'^2} + \overline{w'^2}) \tag{2.24}$$

Assuming that there is no rotational and vibrational energy we can proceed to the computation of the heat flux vector **q**

$$\boldsymbol{q} = \frac{1}{2}\rho\overline{c'^2 u'} \tag{2.25}$$

2.3. *dsmcFoam*

In the present study, the *dsmcFoam* and *dsmcFoamStrath* are used within the framework of OpenFOAM, which, use C++ toolbox. The OpenFOAM is a free (available online) computational fluid dynamics (CFD) package under a general GNU license. Based on Bird's method, *dsmcFoam* has previously been used to solve several engineering problems [53]. Complex geometries are treated using structured and unstructured meshes with the *snappyHexMesh* tool. The *dsmcfoam* solver is featuring with particle initialisation in complex systems, particle tracking in structured and unstructured mesh as well as transient or steady state simulations. Force measurement tools are also included in *dsmcFoam* that can be used in aerospace engineering problems.

Originally OpenFOAM came with the solver named *dsmcFoam* which includes several key features that have been described previously. However, in several simulations the extended solver *dsmcFoamStrath* is also used. This other solver includes chemical reactions option, vibrational mode and the Cercignani-Lampis-Lord (CLL) model. Both codes are fully parallelized, which means that each case can be decomposed and run on the number of available core to the user. Post processing is usually made through Paraview or Tecplot in which *dsmcFoam* compatible. In order to use *dsmcFoam* solver the six stages that are usually followed are:

1) Computational mesh generation
2) Set up initial conditions (boundaries, freestream properties, time step)
3) Initialise dsmc particles (*dsmcInitialise*)
4) Start DSMC simulation (*dsmcFoam*)
5) Once steady state solution is achieved, enable time averaging process.

A typical decomposition of a simple rectangular in an eight cores machine is being presented in Figure 2.3

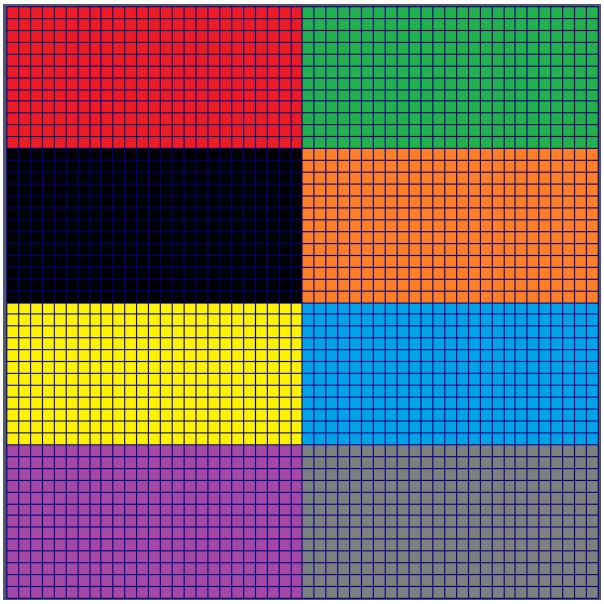

Figure 2-3: Typical Parallel Decomposition (Simple)

2.4. Limitations of DSMC

Despite the fact that DSMC is a powerful tool for simulating rarefied gas flows in high-speed applications and especially for simulating high Knudsen number flows even in complex geometries it has several weaknesses.

DSMC is a computationally expensive method to simulate flows even in the transition regime. In fact, the error and uncertainty is proportional to the square of the number of samples (or simulated particles) [54]. If we want to calculate the bulk flow velocity, this is estimated using the mean velocity of all simulated particles in a cell. This can lead to very slow convergence if we take into account that in order to reduce the error by a factor of 2 we need to increase the simulated particles by four times. This then leads to a huge computational time. For $Kn < 0.1$ DSMC seems to be inappropriate based on computational resources that is needed in comparison with continuum based numerical methods. For such Knudsen number it would be computationally more efficient to use continuum models such as Navier-Stokes-Fourier with temperature jump and velocity slip boundary conditions.

The cell size should be smaller than $\lambda/3$. This is a limitation that can lead to significant errors. Larger cell sizes may result in diffusion errors. Breuer *et al.* studied a Rayleigh flow and showed that cell sizes bigger than the mean free path can lead to higher apparent viscosity [55].

Hadjiconstantinou showed that the error in transport coefficients is proportional to the square of the time step. In principle, a wrong choice of time step Δt can lead the molecules

to travel through several cells before colliding. He characterizes that as *discretization crime* [21].

Each cell should contain at least 20 simulated particles. If we run a case of a 3D box in the dimensions of 1μm x 1μm x 1μm for Kn = 0.1 it will have at least 27000 cells. Taking into account the minimum number of simulated particles we will need for such simulation at least over half millions of simulated particles. If we combine the restrictions for the time step, we can understand that this cannot be achieved on a standalone computer and an HPC will needed.

Another disadvantage of DSMC is the large statistical error especially in low speed gas flows. In principle, in order to reduce the statistical noise in flows in the magnitude of 1m/s a very long time averaging is required. These statistical fluctuations decrease with the square root of the sample. Even though there are modified versions of DSMC in order to treat such flows, it is thought that it is one of the biggest disadvantages of it [56].

Another problem is the uncertainties in physical input parameters. This is especially in the intermolecular collision models. For example, the hard sphere (HS), variable hard sphere (VHS) and variable soft sphere (VSS) models are ideal for different type of problems [5]. The standard hard sphere models are ideal for monoatomic gases or for gases with small rotational and vibrational non-equilibrium effects. If someone would like to simulate gas mixtures, then the VSS model should be used since it introduces an additional power-law parameter and can give the necessary flexibility for these cases.

In the next chapter, we will discuss how these limitations and uncertainties can be overcome by the incorporation and use of other extended hydrodynamic models that are based on the continuum theory.

Chapter 3

3.Hydrodynamic Models

In the present chapter, we firstly review the fundamental problem of proposing extended hydrodynamic methods in order to describe fluid flow based on the *atomistic view to the laws of motion of continua*. After that, we present our newly developed extended hydrodynamic models and their computational fluid dynamics (CFD) codes.

3.1. Overview

Description of fluid motion was a problem exhibited since ancient civilizations. The Greek mathematician and physicist Archimedes (of Syracuse) was the first to propose a scientific study of motion of fluid in his study *On Floating Bodies* nearly 250BC.

Among the firsts that proposed their theory about fluid motion was Isaac Newton when he stated that the shear stress between layers of fluid is proportional to the velocity gradient in the direction perpendicular to the layers. In a historical overview, we find the Daniel Bernoulli equation in 1738 when he proved that pressure is proportional to the acceleration. In other words, the Bernoulli equation is approximate relation between pressure, velocity, and elevation. Among the most noted works is the one by Leonhard Euler (Bernoulli's associate) when he applied the Newton's second law of motion to incompressible fluid dynamics and presented the *Euler equations*. The heat conduction equation was later presented by Joseph Fourier. One of the most noticeable works was from the Claude Navier in 1822 when he introduced the element viscosity in the Euler equation for more realistic and vastly more difficult problem of viscous flows. The general theory of stress was expressed a year later by Cauchy and according to his law a stress tensor exists which maps the normal to a surface to the traction vector acting on that surface. The so-called Navier-Stokes equations were published when George Stokes published the complete set of equations in 1845. Until 1850 the description of flow was based on the continuum theory. In 1872, Ludwig Boltzmann published the *Kinetic Theory of Gases*. In this work, the

famous *Boltzmann equation* was introduced. It is the most celebrated nonlinear kinetic equation even today (after 150 years). In principle *Boltzmann equation* describes the dynamics of slightly rarefied gas by taking into account the free flight of the particles and their collisions.

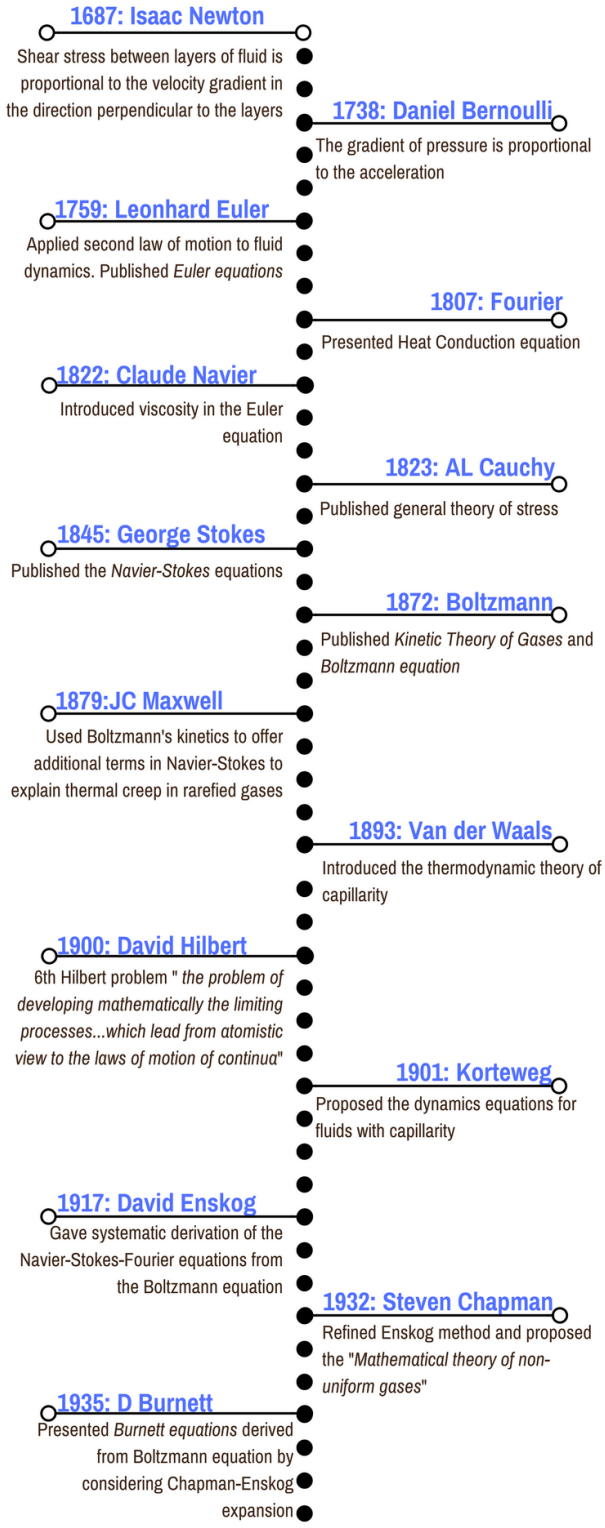

Figure 3-1 Fluid Mechanics Milestones

Even today, with the high advances in computational resources Boltzmann equation can be used for limited problems. Rarefied gases attracted more interest after Boltzmann proposed

his equation. In that manner, Maxwell proposed additional terms in the standard Navier-Stokes equations in order to explain thermal creep in rarefied gases. The Maxwell additional terms were proposed in 1879 and in other words are boundary conditions. In 1893, Johannes Diderik van der Waals introduced the thermodynamic theory of capillarity under the hypothesis of a continuous variation of density. At that period, (late 1800s) more attempts were started in order to capture non-equilibrium effects with continuum methods. In 1900 David Hilbert proposed twenty-three problems in mathematics. During the time of writing only nine have fully resolved. The 6th Hilbert problem is *Mathematical treatment of axioms of physics*. Even today, the problem remains actually controversial due to the title of it. From the scientific perspective, the 6th Hilbert problem can be described as going *from atomistic view to the laws of motion of continua.* Several attempts have been made until today now claiming that have solved the problem. Based on the van der Waals approach, his PhD student, Korteweg, proposed the dynamics equations for fluids with capillarity. Korteweg model, can be simply described as extended Navier-Stokes equations. Several years later, 1917, David Enskog presented a systematic derivation of the Navier-Stokes equations from the Boltzmann equation. In 1932, Chapman and Cowling refined Enskog method; the well-known Chapman-Enskog expansion. Three years later, Burnett, presented a series of equations derived from Boltzmann equations using the Chapman-Enskog expansion.

The above, describes the historical timelines in fluid mechanics in order to solve fluid flow under any condition. However, one can notice from the milestones (Fig.3.1) that lot problems arise in rarefied gases. Based on this manner we describe below continuum based methods and the kinetic theory in rarefied gas flows [57].

3.2. Hydrodynamic Models in Rarefied Gas Dynamics

As described above and in previous chapter, the description of rarefied gas flows remains difficult to solve by continuum methods. The limits of many continuum models are usually tested in rarefied gases and this is due to the fact that they should capture non-equilibrium phenomena that occur in the atomistic level. Crookes in 1876 (Figure 3.2), performed an experiment with radiometer showed that the radiation intensity is indicated by the rotation speed of the mounted vanes on a spindle enclosed in an evacuated glass bulb [58]. The rotation of the vanes is driven by the rarefied gas flow in the bulb due to the temperature difference across the vanes. In other words, the radiometer when it was exposed to light then the vanes turn.

Figure 3-2 Crooke's Radiometer

The work from Crookes enabled the research in rarefied gases. In the rarefied gases, the inhomogeneity of temperature field that can lead to gas motion is called "*thermally induced flows*". Based on the idea of surfaces of discontinuity Gibbs published the theory of capillarity. Gibbs, developed the equilibrium thermodynamics of interfaces theory. Just after the Crookes radiometer, he recognized that a liquid-vapour interface actually represented a rapid but smooth transition of physical quantities between bulk fluid values [18]. The flow that is induced in the direction of a temperature gradient in a rarefied gas long channel with a temperature gradient along it is called thermal transpiration phenomenon.

The mysterious observations (at that time) from Crookes radiometer were explained by Maxwell's revolutionary paper in 1879 in terms of thermal creep. The fact that the thermal creep is representing a strictly linear phenomenon according to Maxwell's paper gave the full explanation for Crookes radiometer and Reynold's thermal transpiration phenomenon in gases [3]. In 1893, van der Waals proposed gradient theories based on thermodynamic principles for the interface for non-isothermal multiphase fluids. He introduced an equation of state and based on that he showed that the liquid-vapour interface becomes infinite as the critical temperature is approached [19]. In more detail, Van der Waals introduced the term $c(\nabla\rho)^2$ in the energy density, where c is a capillarity coefficient and ρ is the density. The theory of continuous transition layers which developed by van der Waals gave very close results with the Gibbs theory.

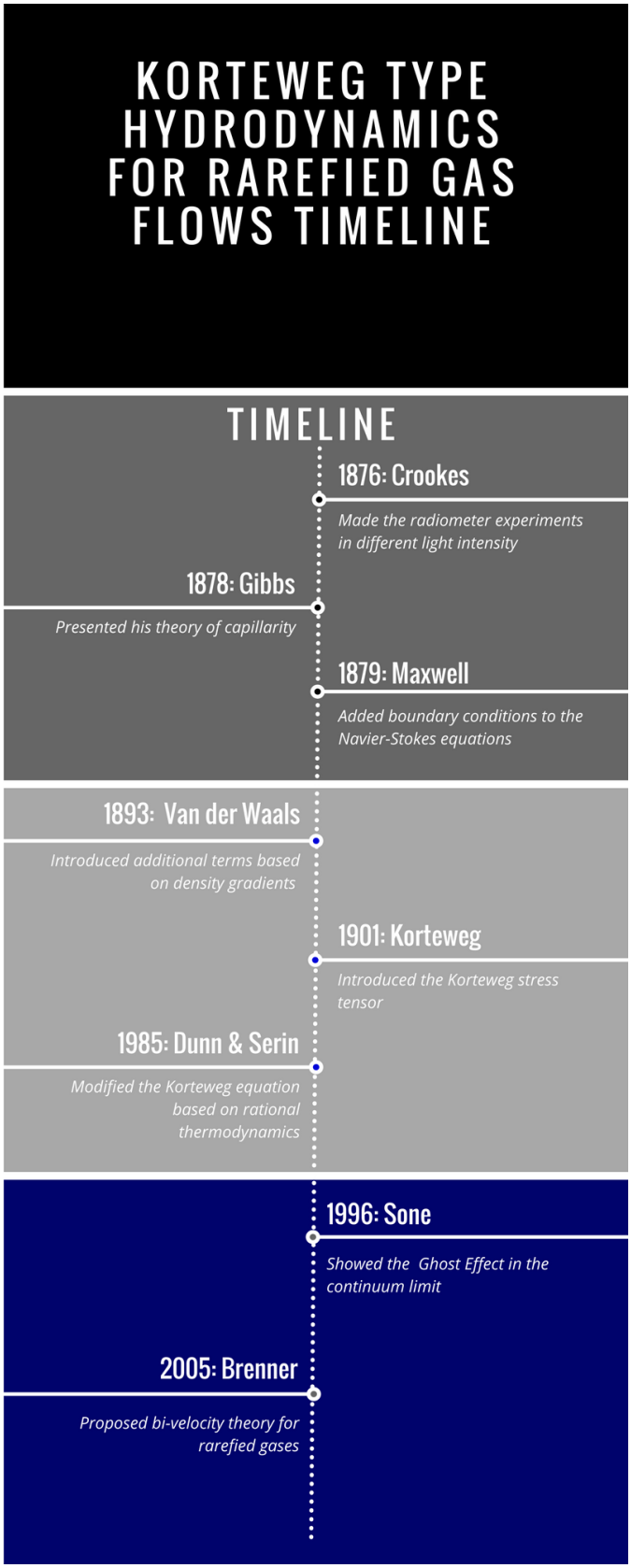

Figure 3-3 Rarefied Gas Milestones

Few years later, a Dutch physicist Korteweg, a PhD student of Van der Waals, published a paper presenting a constitutive equation for the Cauchy stress that included density

gradients [20]. Korteweg theory was proposed for multiphase flows (liquid-vapor) to analyse their structure phase transitions under static and dynamics conditions [59]. The proposed model was incorporating new terms in the stress tensor depending on the gradient of the density ρ. The additional terms in Korteweg stress tensor may be viewed as an additional contribution to the Navier-Stokes. This idea was proposed after Korteweg made some considerations on the possible interactions between molecules in two neighboured infinitesimals representing volume elements. These nonlocal interactions of the molecules within the interface appear in the stress tensor in terms of density derivatives. The material coefficients that appear in the Korteweg stress tensor should vanish in order to be compatible with conventional thermodynamics and the second law [59]. In 1929, Epstein quantified the phenomenon of thermophoretic particle motion in gases on the basis of thermal creep [60]. This work, showed the importance of thermophoresis in a wide variety of applications. The Korteweg work was reviewed by Dunn and Serrin in 1985 [59]. As mentioned earlier, Dunn and Serrin showed that the classical Korteweg stress tensor is incompatible with the classical thermodynamic principles. As a result of this they concentrate on developing a thermodynamic structure which retains the purely thermal Clausius-Duhem inequality. In other words, the modification that Dunn and Serrin introduced in the energy equation, an additional term called *interstitial working*, u, as the rate of supply of mechanical energy across every material surface of the body [61]. The work from Dunn and Serrin represents different modifications from the rational thermodynamics point.

In a series of papers, Sone presented the so-called *ghost effect* and he showed that the heat-conduction equation is not appropriate to describe the temperature field in a gas at rest in continuum limit [62, 63]. Sone, concluded later that we will not know the behaviour of the gas in the continuum limit unless we know what happens when the gas is rarefied [64]. This work pioneered research about continuum mechanics and the inappropriateness under certain conditions even at the continuum limit (or the limit where the mean free path of the gas molecules or the Knudsen number of the system tends to zero). In all of these works, Sone studied fluids (or gas) at rest and where the pressure is uniform and the temperature field is determined by the heat-conduction equation. The *ghost effect* describes when something that does not exist in the limit of $Kn \approx 0$, but it exists for a finite Kn, gives a finite effect on the behaviour of the gas in this limit. Sone concluded recently in his book that the Navier-Stokes set are inconsistent and there is a necessity of convection term in the energy equation and another higher order term in the momentum equation [57]. In 2004, Howard Brenner, Professor at MIT published a paper where he started a discussion if the

volume velocity of a fluid is equal to its mass velocity [65]. By that time, it was believed that the mass and volume velocity of a fluid are equal. Brenner, was inspired by the thermophoresis phenomenon and added a diffusion term in the momentum equation and especially in shear stress tensor. A year later, Brenner concluded his work and modified the Navier-Stokes equations with appreciable density gradients that previously appeared in the Van der Waals theory [66]. The bi-velocity theory of Brenner (that's how is called) was come to add some other observations similar to what Sone did a few years later but from different perspective. First of all, Brenner observed that the density variations are caused by variation in temperature (similar to *ghost effect*). His theory was tested in several works and it was proved to be better than standard Navier-Stokes [67, 68]. The bi-velocity hydrodynamics were completed upon recognizing the need to suggest requirement that the constitutive equations within the new theory satisfy a condition of mechanical equilibrium. A summary of the Korteweg type hydrodynamics is summarized in Fig. 3.3. The bi-velocity theory is applicable in compressible flows and usually not in incompressible since the density is constant in such flows. Brenner's theory should be viewed as strictly continuum in nature [69]. Dadzie presented a fully thermo-mechanically consistent set of equations without Chapman-Enskog expansion. This work remains until today the most consistent work of the bi-velocity hydrodynamics that is fully stable [70]. That work has been tested later in several other problems within its simplified forms[71, 72].

3.3. Development of new Hydrodynamic Models

The diffuse interface theories are dated back to the initial work from van der Waals. That work pioneered the work for non-classical continuum and thermomechanical principles. This was followed later by Korteweg as well as by Dunn and Serin. Dunn and Serin introduced the notion of an interstitial work-flux contribution in the energy equation beyond the classical Fourier heat flux [59]. In a very recent work from Gorban and Karlin, it was concluded that Korteweg model is the first post Navier-Stokes equation which remains inside continuum mechanics and at the same time captures some non-equilibrium kinetic phenomena [73].

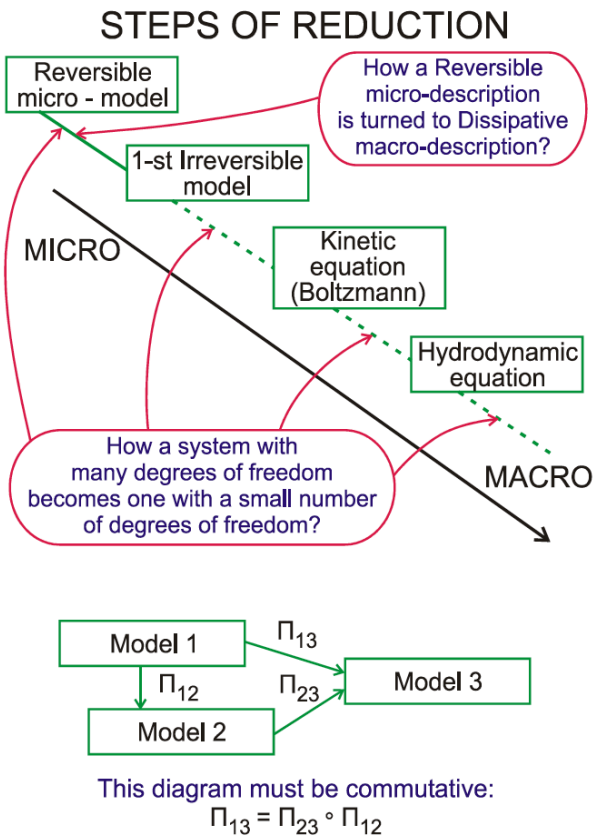

Figure 3-4 The Stairs of Reduction[74]

Figure 3.4 shows the stairs of reduction which actually lead from the reversible microdynamics to irreversible macrokinetics [74]. Based on the above description and observation we continue with the two new hydrodynamics models.

3.4. Compressible Korteweg fluid like model

From Van der Waals theory of capillarity authors noted that near a liquid-vapour phase transition a thermodynamic formulation of the fluid flow equations includes contributions from a density gradient-energy term. This formulation introduces in the momentum equation a capillarity stress tensor [75]. This stress tensor also referred to as the Korteweg stress tensor may written [76] :

$$\boldsymbol{\Pi_k} = \left(\beta \frac{1}{2} |\nabla\rho|^2 + \gamma\rho\Delta\rho\right)\mathbf{I} + \alpha(\nabla\rho \otimes \nabla\rho) \tag{3.1}$$

where ρ is the fluid density, I is the identity tensor and the term $\alpha\,(\nabla\rho \otimes \nabla\rho)$ also sometimes referes to as the Korteweg tensor. One can note in the above equation the importance of gradient of density in the Korteweg tensor which can confirms Van der Waals theory. The phenomenological coefficients α, β, γ are material function dependent

upon ρ and called capillary coefficients. Their exact value and expression are still elusive [77]. From a dimensional analysis, they may be represented as:

$$a = \beta = \gamma = \alpha^* \frac{\mu^2}{\rho^3} \tag{3.2}$$

Where α^* is a scalar. The standard Navier-Stokes may then be modified by adding the Korteweg stress Eq.3.1, to its viscous stress tensor The derivatives of the density that appear in the above stress tensor arise from the nonlocal interaction of the molecules within the interface.

A compressible Korteweg fluid flow equations is therefore written as:

Conservation of mass

$$\frac{\partial \rho}{\partial t} + \nabla \cdot [\rho \boldsymbol{U}] = 0 \tag{3.3a}$$

Conservation of momentum

$$\frac{\partial \rho}{\partial t} + \nabla \cdot [\rho \boldsymbol{U}] = 0 \tag{3.3b}$$

Conservation of total energy

$$\frac{\partial}{\partial t}\left[\frac{1}{2}\rho U^2 + \rho e_{in}\right] + \nabla \cdot \left[\frac{1}{2}\rho \boldsymbol{U^2 U} + \rho e_{in}\boldsymbol{U}\right] + \nabla \cdot [(p\boldsymbol{I} + \boldsymbol{\Pi}) \cdot \boldsymbol{U}] + \nabla \cdot \boldsymbol{J} = 0 \tag{3.3c}$$

where the shear stress term $\boldsymbol{\Pi}$ is given by**,**

$$\boldsymbol{\Pi} = -2\mu \overset{\circ}{\overline{\nabla \mathbf{U}}} - \boldsymbol{\Pi_k}) \tag{3.4}$$

composed of the standard Navier-Stokes stress component

$$\boldsymbol{\Pi_{ns}} = -2\mu \overset{\circ}{\overline{\nabla \mathbf{U}}}$$

With

$$\overset{\circ}{\overline{\nabla \boldsymbol{U}}} = \frac{1}{2}\left(\nabla \boldsymbol{U} + \widetilde{\nabla \boldsymbol{U}}\right) - \frac{1}{3}\mathbf{I}\nabla \cdot \boldsymbol{U} \tag{3.5}$$

with $\widetilde{\nabla \boldsymbol{U}}$ denoting the transpose tensor of $\nabla \boldsymbol{U}$ and **I** the identity matrix.

and the capillary stress tensor is $\boldsymbol{\Pi_k}$, Eq. 3.1.

The heat flux, $\boldsymbol{J}$, is given here as:

$$\boldsymbol{J} = -k\nabla T \tag{3.6}$$

3.5. Bi-velocity model

Kinetic derivation of the volume diffusion continuum equations is based on the inclusion of an additional transport term originating from particle molecular level spatial diffusion [70]. The changes on the stress tensor are based on density gradients as Van der Waals and Korteweg proposed.

Two different macroscopic fluid velocities can then be derived based on different averaging methods. Bi-velocity method recognizes the appearance of two (conceptually) different velocities. In one hand, the mass velocity $\boldsymbol{U_m}$ is proportional to the mass flux and is found in the continuity equation. On the other hand, volume velocity, $\boldsymbol{U_v}$, accounts for variation in volume occupied by the mass. A volume flux density relates the two:

$$\boldsymbol{U_v} = \boldsymbol{U_m} - \boldsymbol{J_c} \tag{3.7}$$

Where:

$$\boldsymbol{J_c} = -\frac{k_m}{\rho}\nabla\rho \tag{3.8}$$

with k_m an additional transport coefficient: the molecular (or volume) diffusivity coefficient.

Figure 3.1 depicts the two different concepts of macroscopic fluid velocity. Flux $\boldsymbol{J_c}$ may be viewed as a molecular level diffusive flux associated with the gas molecule concentration and $-\boldsymbol{J_c}$ is the gas volume diffusive flux. The $\boldsymbol{U_m}$ and $\boldsymbol{U_v}$ are both macroscopic concepts by definition. It should be distinguished that in the volume diffusion theory the fluid particle does not represent a simple point of mass but a volume element. The bi-velocity $-\boldsymbol{J_c}$ is oriented in the direction from high density to low density in the case of compression and the reverse in the case of expansion. With no density variation, $\boldsymbol{J_c}$ vanishes.

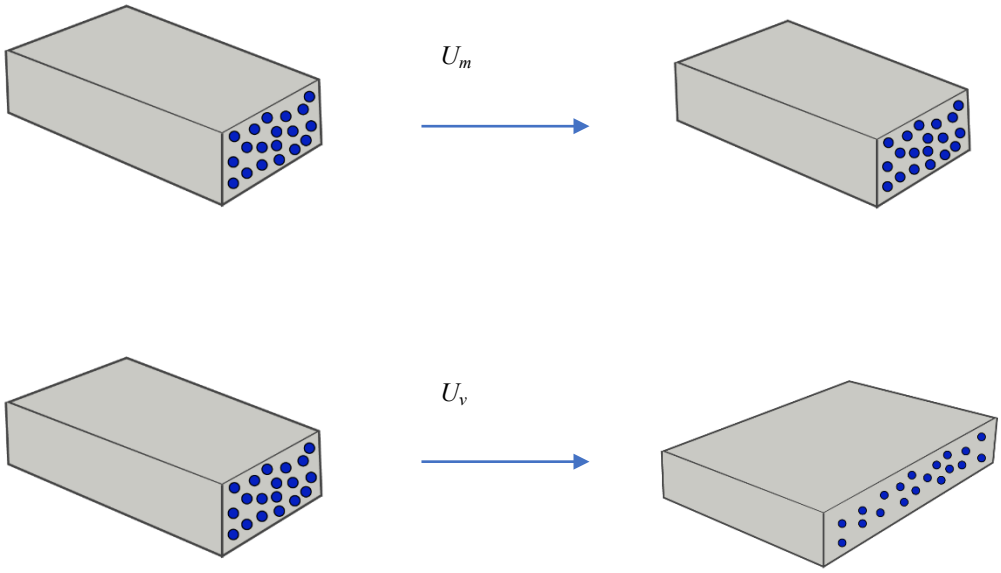

Figure 3-5: Representation of the mass velocity, U_m and volume velocity U_v. Both velocities are macroscopic concepts. a) The macroscopic motion of a fluid element in a fluid without density variations, b) macroscopic motion in a fluid with density variations. The volume diffusion particles are much larger than molecules. The amount of mass (number of molecules) remain the same

A resulting bi-velocity hydrodynamics set of equations are written [72] :

Conservation of mass

$$\frac{\partial \rho}{\partial t} + \nabla \cdot [\rho \boldsymbol{U}] = 0 \tag{3.9a}$$

Conservation of momentum

$$\frac{\partial \rho \boldsymbol{U}}{\partial t} + \nabla \cdot [\rho \boldsymbol{U}\boldsymbol{U}] + \nabla \cdot [p\boldsymbol{I} + \boldsymbol{\Pi}] = 0 \tag{3.9b}$$

Conservation of total energy

$$\frac{\partial}{\partial t}\left[\frac{1}{2}\rho \boldsymbol{U^2} + \rho e_{in}\right] + \nabla \cdot \left[\frac{1}{2}\rho \boldsymbol{U^2 U} + \rho e_{in}\boldsymbol{U}\right] + \nabla \cdot [(p\boldsymbol{I} + \boldsymbol{\Pi}) \cdot \boldsymbol{U}] + \nabla \cdot \boldsymbol{J_u} = 0 \tag{3.9c}$$

where the shear stress term $\boldsymbol{\Pi}$ is given by,

$$\boldsymbol{\Pi} = \boldsymbol{\Pi_v} - \rho \boldsymbol{J_c J_c} \tag{3.10}$$

$$\boldsymbol{\Pi_v} = -2\mu \overset{\circ}{\overline{\nabla [\boldsymbol{U_m} - \boldsymbol{J_c}]}} \tag{3.11}$$

and the energetic heat flux, $\boldsymbol{J_u}$, is given by,

$$\boldsymbol{J_u} = \boldsymbol{q_{ve}} + p\boldsymbol{J_c} \tag{3.12}$$

The specific internal energy of the fluid is $e_{in} = (3/2)\,RT$.

In the set of equations (3.9) $\boldsymbol{q_{ve}}$ is the entropic heat flux given by the Fourier's law [70] :

$$\boldsymbol{q_{ve}} = \boldsymbol{q_v} + \rho e_{in}\boldsymbol{J_c} = -k\nabla T \tag{3.13}$$

The volume diffusivity coefficient may be related to dynamic viscosity, μ, as:

$$k_m \equiv \alpha\frac{\mu}{\rho} \tag{3.14}$$

where our investigation led to α as a rarefaction dependent parameter:

$$\alpha = \frac{1}{\mathrm{PrKn}} \tag{3.15}$$

The mean free path, λ was calculate as:

$$\lambda = \frac{2(5-2\omega)(7-2\omega)}{15}\left(\frac{m}{2\pi k_B T}\right)^{\frac{1}{2}}\left(\frac{\mu}{\rho}\right)$$

with ω the temperature coefficient and m the atomic mass [78].
By substituting Eq 3.15 into Eq 3.14 and then into Eq 3.8 we have the final expression of the effective volume flux:

$$\boldsymbol{J_c} = -\frac{\mu}{\mathrm{PrKn}\rho^2}\nabla\rho \tag{3.16}$$

One can solve the bi-velocity equations, either by incorporating the new terms in the stress tensor or by solving directly for volume velocity

3.6. Computational Fluid Dynamics (CFD) Hydrodynamics solvers in OpenFOAM

Numerical implementations of the two set of hydrodynamics equations are done on the OpenFOAM platform. These are adaptations of the solver rhoCentralFOAM which comprises of a finite volume (FV) discretization using semi-discrete, non-staggered central schemes for colocated variables prescribed on a mesh of polyhedral cells that have an arbitrary number of faces and solved on a three-dimensional unstructured mesh of polygonal cells. RhoCentralFOAM was initially developed to simulate compressible flows with better shock capturing [41]. In this work the discretization of a finite volume (FV) is achieved using semi-discrete, non-staggered central schemes as proposed by Kurganov and Tadmor [79]. In general, the computational domain is divided in continuous control cells. Faces are either parts of outside boundaries and interests only one cell or are part of internal mesh and interest two cells. For rarefied gases, the fluid properties are not transported only by the fluid flow but from propagation of waves as well. For this reason, the construction of flux interpolations is from a neighbouring cell to a given face only. The present solver is based on central-upwind schemes of Kurganov and Tadmor; first order in time, second order in space. By default, all OpenFOAM solvers are three dimensional. Each solver is density-based solver and it uses a more physical form of the equations described in section 3. The solver initially starts with solving the inviscid version of the set of conservative equations in an iterative order. Density-weighted fields are calculated first. The momentum density is calculated from $\dot{\boldsymbol{U}} = \rho \boldsymbol{U_m}$ and the total energy density $\dot{E} = \rho E$. Where the total energy is $E = e_{in} + \frac{|\boldsymbol{U_m}|^2}{2}$. The set of equations are consequently solved then for ρ, $\dot{\boldsymbol{U}}$ and $\dot{E}$. Based on these the temperature, T, is evaluated by the subtraction of kinetic energy from the total energy as:

$$\mathrm{T} = \frac{1}{\mathrm{c_v}}\left(\frac{\dot{\mathrm{E}}}{\rho} - \frac{|\mathbf{U_m}|^2}{2}\right) \tag{3.17}$$

Where C_v is the specific heat capacity at constant volume.

The momentum and heat diffusion are introduced in the compressible Navier-Stokes, rhoCentralFoam solver by the inclusion of necessary diffusive terms in the governing constitutive equations. $\boldsymbol{U_m}$ and T are evaluated explicitly since the momentum and energy equations are solved explicitly as noted in the inviscid version above. The following procedure will be completely explicitly and all new solutions at the current time level (Δt)

would be calculated from convection, diffusion and boundary conditions from the previous level (*Δt-1*).

The solver starts with the solution of the momentum equation by solving for $\dot{\boldsymbol{U}}$:

$$\frac{\partial \dot{\boldsymbol{U}}}{\partial t} + \nabla \cdot \left[\boldsymbol{U_m}\dot{\boldsymbol{U}}\right] + \nabla p = 0 \tag{3.18}$$

Mass velocity is then updated by solving $\boldsymbol{U_m} = \dot{\boldsymbol{U}}/\rho$. This step is done before solving a diffusion correction for $\boldsymbol{U_m}$

$$\frac{\partial \rho \boldsymbol{U_m}}{\partial t} - \nabla \cdot (\mu \nabla \boldsymbol{U_m}) + \nabla \cdot (\mu \nabla \boldsymbol{J_c}) - \nabla \cdot \left(\boldsymbol{\Pi}_{exp}\right) = 0 \tag{3.19}$$

Where the terms in the stress tensor containing inter-component, coupling are treated explicitly for both methods. For the bi-velocity method this explicit component of the stress tensor is:

$$\boldsymbol{\Pi}_{exp} = \mu\,[(\nabla \mathbf{U_m})^{\mathrm{T}} - (\nabla \mathbf{J_c})^{\mathrm{T}}] - \left(\frac{2}{3}\right)\mathrm{tr}(\nabla \mathbf{U_m})\mathbf{I} + (\frac{2}{3})\mathrm{tr}(\nabla \mathbf{J_c})\mathbf{I}$$

In equation 3.19 we note the appearance of the term $\nabla \cdot (\mu \nabla \boldsymbol{J_c})$, which is neglected for the Korteweg solver. The Laplacian terms from the deviatoric tensor $\nabla \cdot (\mu \nabla \boldsymbol{U_m})$ and $\nabla \cdot (\mu \nabla \boldsymbol{J_c})$ are implemented implicitly and they form coefficients within the solutions matrixes, rather than values in the source vectors. For the boundaries in $\boldsymbol{U_m}$ and $\boldsymbol{J_c}$ are also implemented implicitly and condition is applied by direct substitution of the gradients at boundary faces. Similar procedure is followed to implement Korteweg compressible fluid model where the additional explicit component of the stress tensor is now:

$$\boldsymbol{\Pi}_{exp} = \mu\left[(\nabla \mathbf{U_m})^{\mathrm{T}} - \left(\frac{2}{3}\right)\mathrm{tr}(\nabla \mathbf{U_m})\mathbf{I}\right] + \left(\frac{\mu^2}{2\rho^3}|\nabla\rho|^2 + \frac{\mu^2}{\rho^2}\Delta\rho\right)\mathbf{I} + \alpha^*\frac{\mu^2}{\rho^3}\nabla\rho \otimes \nabla\rho$$

To obtain the solution for the energy equation, similar procedure is followed by first solving for $\dot{E}$ as:

$$\frac{\partial \dot{E}}{\partial t} + \nabla \cdot \left[\boldsymbol{U_m}\left(\dot{E} + p\right)\right] + \nabla \cdot (\boldsymbol{\Pi} \cdot \boldsymbol{U_m}) = 0 \tag{3.20}$$

The $\boldsymbol{U_m}$ has been updated by the new terms that appear in Korteweg and bi-velocity model as in Eq. 3.19. The temperature, T is updated from ρ, $\mathbf{U_m}$ and $\dot{E}$ from the equation 4.1 before solving a diffusion correction equation for T:

$$\left(\frac{\partial(\rho c_v T)}{\partial t}\right) - \nabla\cdot(k\nabla T) - k_m\nabla\cdot\left(\frac{p}{\rho}\nabla\rho\right) = 0 \tag{3.21}$$

Here, in our solver we only correct the additional term $\nabla\cdot\left(\frac{p}{\rho}\nabla\rho\right)$ in the bi-velocity model and it is treated explicitly. However, the additional heat flux component also exists in principle in Korteweg theory. As the application in the present investigation concerns isothermal gas flow in microchannel, actual solution to the energy equation is of less importance.

Boundary Conditions

Maxwell type first-order slip boundary conditions are adopted to accompany the different hydrodynamics equations. In more detail, we used the slip boundary conditions as presented below [3]:

$$\boldsymbol{U_m} - \boldsymbol{U_w} = -\left(\frac{2-\sigma_u}{\sigma_u}\right)\frac{\lambda}{\mu}\boldsymbol{\tau_v} - \frac{3}{4}\frac{\mathrm{Pr}\,(\gamma-1)}{\gamma p}\mathbf{j} \tag{3.22}$$

$\mathbf{n}$ is the unit normal vector defined as positive in the direction of the flow domain. Where $\mathbf{U_w}$ is the wall velocity, σ_u is the tangential momentum accommodation coefficient and where $\boldsymbol{\tau_v}$ is the new tangential shear stress, $\boldsymbol{\tau_v} = \mathbf{S}\cdot(\mathbf{n}\cdot\boldsymbol{\Pi_v})$. The tensor $\mathbf{S} = \mathbf{I} - \mathbf{nn}$ and $\mathbf{j} = \mathbf{J}\cdot\mathbf{S}$

Further to the Maxwell slip, Smoluchowski developed temperature jump conditions which is driven by the heat flux to the surface in the normal direction [34].

$$T - T_w = -\frac{2-\sigma_T}{\sigma_T}\frac{2\gamma}{(\gamma+1)\mathrm{Pr}}\lambda\nabla_{\mathbf{n}}T \tag{3.23}$$

$\nabla_{\mathbf{n}} \equiv \mathbf{n}\cdot\nabla$ is the component of the gradient normal to the boundary surface and $\mathbf{n}$ is the unit normal vector defined as positive in the direction of the flow domain. T_w is the wall temperature; γ is the specific heat ratio and σ_T the thermal accommodation coefficient and

can take values from 0-1. Where 0 corresponds to perfect energy exchange between the gas and the boundaries and 0 to no energy exchange.

Chapter 4

4. Flow Through Porous Media

In the current chapter the flow through porous media will be discussed. A single-phase flow is considered. Firstly, it is aimed to describe the representation of the porous media in computational domain and then the different methods that are used to simulate the gas flow. We concentrate on flows in high Knudsen numbers (Kn ≈ 1) with applications in oil & gas industry and planetary sciences.

4.1. Overview

Accurate description of fluid properties through complex porous media is of great importance for various engineering applications, varying from natural gas reservoirs to comets outgassing. It also plays a key role in other geosciences applications, including CO_2 storage. Accurate description of gas flow through porous media will help enhance global hydrocarbon production and ensure energy supply. As for the application in planetary sciences, it will help understanding the outgassing flow near the surface boundary layer when comets are close to perihelion. From such results, future space missions in comets will take advantage.

Conventional gas reservoirs consist of pore size in the range of 1 to 100 micrometers where shale gas reservoirs can have pores in the range of 1 to 200 nanometers. Pore networks in unconventional gas reservoirs consist of pore networks from mineral matrix and organic matter. Mineral matrix pores vary from nanoscale to microscale (10nm – 100 μm) whereas the organic matter lies only in nanoscale (10 – 750nm). Due to the existence of pores with several multitudes of sizes, transport in those types of reservoirs is a complex process at micro (10^{-6} m) to nano-scale (10^{-9} m) [26]. Production from unconventional gas reservoirs such as tight and shale gas are now key role players in the global energy market. In these types of reservoirs, the gas is stored in mineral pores or adsorbed into organic matter.

Natural gas reservoirs consist of methane (90%), nitrogen (5%) and carbon dioxide (5%) [31]. Understanding transport mechanism in micro (10^{-6} m) to nano-scale (10^{-9} m) in natural gas reservoirs is crucial for accuracy in reservoir simulations. Gas-surface interactions at molecular scale for CH_4, which the natural gas reservoirs consist mostly of, are also of great importance. As Fig 4.1 illustrates, unconventional gas reservoirs have pressures in the range of 1 – 100 MPa [27]. Under those pressures and pore sizes the mean free path (λ) is comparable to the characteristic length of the pore and the gas is often in rarefied regime [5, 28] . Investigation of gas properties in unconventional gas reservoirs depending on the Knudsen number has been conducted by only few researchers [80, 81].

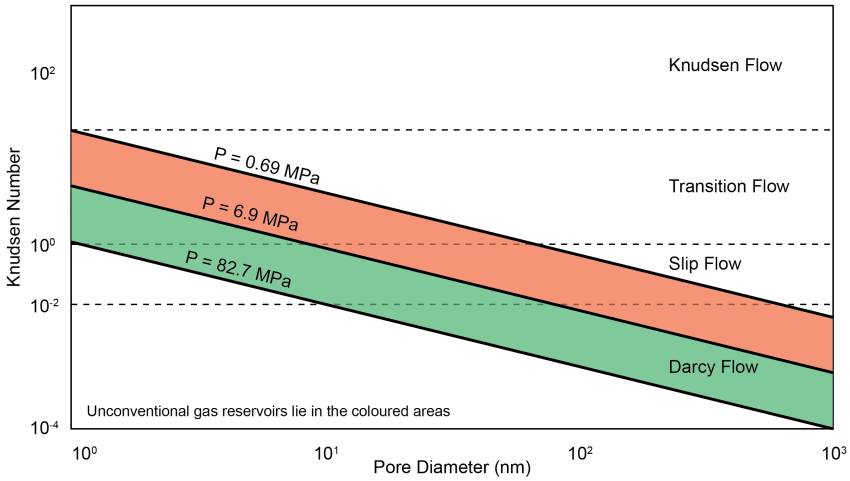

Figure 4-1 Knudsen number versus pore diameter (nm) at different pressures for methane at 100 ^oC

In nanopores the gas velocity and gas temperature near the walls are not zero [81]. Klinkenberg noted the gas slip on the walls in micro and nanopores [40]. He noticed that for pores where the diameter is comparable to the mean free path the gas molecules move forward into the transport direction. Klinkenberg also noted that the gas slippage is responsible for increasing permeability. He introduced an equation for calculating the permeability by introducing some correction factors. Due to the fact that on the Klinkenberg equation the permeability is inversely proportional to the pressure, the Klinkenberg effect can be found for a wider range of pore size with lower pressure. Several slip models (i.e Maxwell, Beskok & Karniadakis) have been proposed to correct the NSF for a wide range of Knudsen number. However, these models are generally inadequate for Kn > 1 and flow rate at nanoscale are greater than that predicted by Darcy's equation [30, 31]. Darcy's Law, which was concluded from experiments and derived from continuum

methods (Navier-Stokes equations), is no longer valid without any slip modification [29-32].

Comets are consisting of high porosity material and their production rate from sublimation is in the range of 3 x $10^{19\text{-}21}$ molecules/m^2/s. The Rosetta mission from European Space Agency (ESA) is for the first time that a spacecraft is orbiting a comet for such an extended period, from the onset to the activity through-out the perihelion passage. Outgassing flow from the onset to perihelion is purely rarefied, ranging from the transition regime to the free molecular regime. Understanding of the flow near the surface of a comet will help future missions and especially the landing operations.

Gas flows in such conditions is rarefied which lies in the transition or free molecular regimes. As mentioned, standard continuum methods are not appropriate for simulating these flows. Further to the complexity of gas flow, the structure of the porous medium in direct simulations is another important factor.

4.2. Pore Scale Modelling and Imaging

In order to estimate rock and flow properties at larger scales, modelling the fluid flows at the pore scale of a porous medium can provide an excellent tool to study and understand the physics of transport phenomena in porous media. In the past, experimental methods were used to characterize the pore space. The most common method to estimate the porosity was the mercury injection (mercury porosimetry) [82]. However, mercury injection cannot provide pore size distribution and can only give a calculated effective porosity. This method is not appropriate for micropores. The pore scale of porous media is in the range of 10^{-9} to 10^{-4} m. The modern methods in computers capabilities allowed the simulation in complex geometries (like porous medium) using parallelization techniques. An accurate description of flow in porous media at pore scale will allow scientists up-scale the observations to the reservoir and comet scale. The characterization of the pore geometry and complex porous media occur when direct imaging methods become available for small scales.

Scanning Electron Microscopy (SEM) technology is a method for obtaining 2D images in a very high resolution (up to nanometer scale). This type of image was used in the oil and gas industry several years ago. However, with this method the connectivity of the pore space remains unknown. Under particular circumstances it can give good information for tight rocks, like unconventional gas. Furthermore, FIB (Focus Ion Bean)-SEM is used to

generate very high resolution three-dimensional images of small rocks. It should be noted that this method is destructive.

During the past decade, new techniques have been revealed and offer an alternative method to represent rock. To generate high resolution 3D images of a porous media in small scale the X-Ray technique is used [83]. This method is used with laboratory instrumentation and it is named as micro-computed tomography (micro-CT) and the instrumentation can be seen in Fig.4.2. Initially, micro-CT was used in biomedical applications.

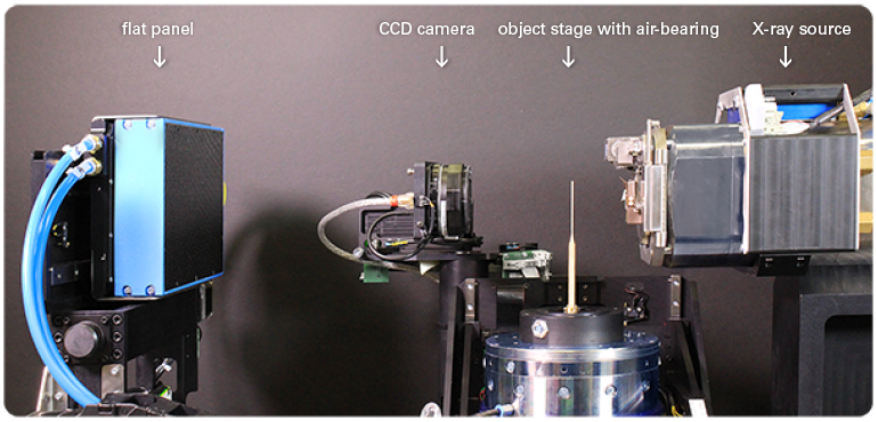

Figure 4-2 Micro-CT Imaging Scanner

For the applications in the porous medium, the core sample rotates (360 degrees) and the X-Ray is recording from different directions and angles the movement in order to produce a 3D representation image of the rock (Fig 4.3a). Different algorithms are used to represent the void and solid spaces [84]. In order to remove the noise of the obtained image, several filters are applied. In our days, the resolution of such scanning can be well over 1000 voxels in each direction. The output from a micro-CT scanner is a grey scale binary image as it can be observed from Fig 4.3b with an extension of .raw. The binarized image uses 0 and 1 to represent void and (or) solid. The first step of the image processing is to visualize the binary image with different type of software. The image can be cropped into a 3D cubic and finally segmented into void and space. The segmentation step is important since it will generate the mesh on the image. The final result will be a binary 3D image in a stereo-lithography file format.

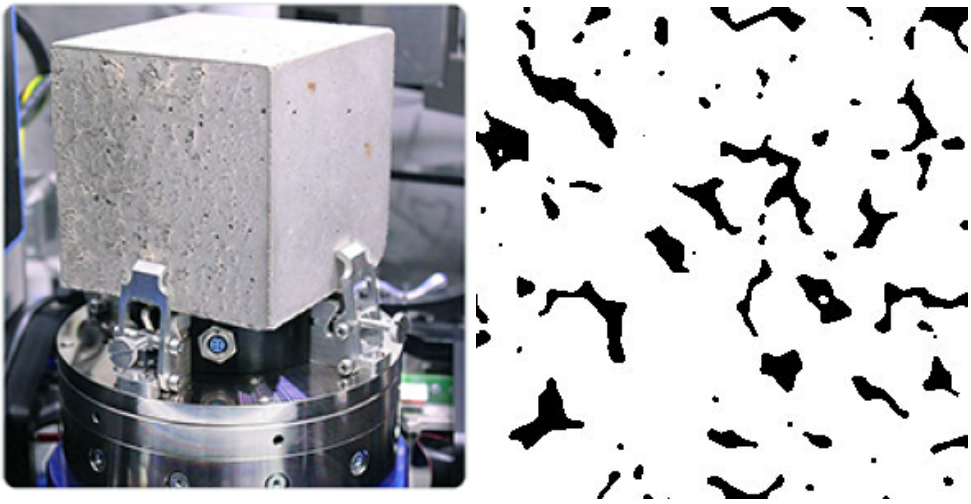

a) b)

Figure 4-3 a) Micro-CT Imaging Rotating b) Output Binary Image

It is widely accepted that the micro-CT high-resolution 3D images provide an excellent opportunity to simulate gas flow directly on the rock image and investigate the mechanisms the govern the flow at the pore scale. This will give the necessary information to accurately calculate macroscopic properties of the rock such as porosity and permeability. This type of image in computer-based simulation can offer helpful insights into the gas flow physics in pore scale and predict flow properties in porous media.

In order to simulate flow (single or multiple phase) through binary pore-scales images there are usually two ways to model the flow. The first technique is called direct modelling (Fig. 4.4a). In this method, the pore space is discretized using Cartesian mesh as most of the open source CFD packages use. This is actually a direct approach of the geometry and can represent the pore space geometry reasonably well. On the other hand, due to the large number of cells high computational requirements are required. This is mainly due to the large memory that is needed to handle all the necessary information for each cell depending on the method that is used. This technique has previously been applied directly on pore-space images using the Lattice Boltzmann (LB) method [85]. The particle-based methods are easily applicable in such type of direct simulations. However, they are facing the problem of tracking and saving particles properties and collisions. The recent advances in HPC science allowed us to use parallel computing to efficiently run such simulations with inconsiderable problems. To date, several studies have been carried out to simulate single or two phase flows using direct modelling on pore space images [86]. It is expected that direct modelling on pore image that are extracted from micro-CT scanners will face considerable interest from researchers in the following years.

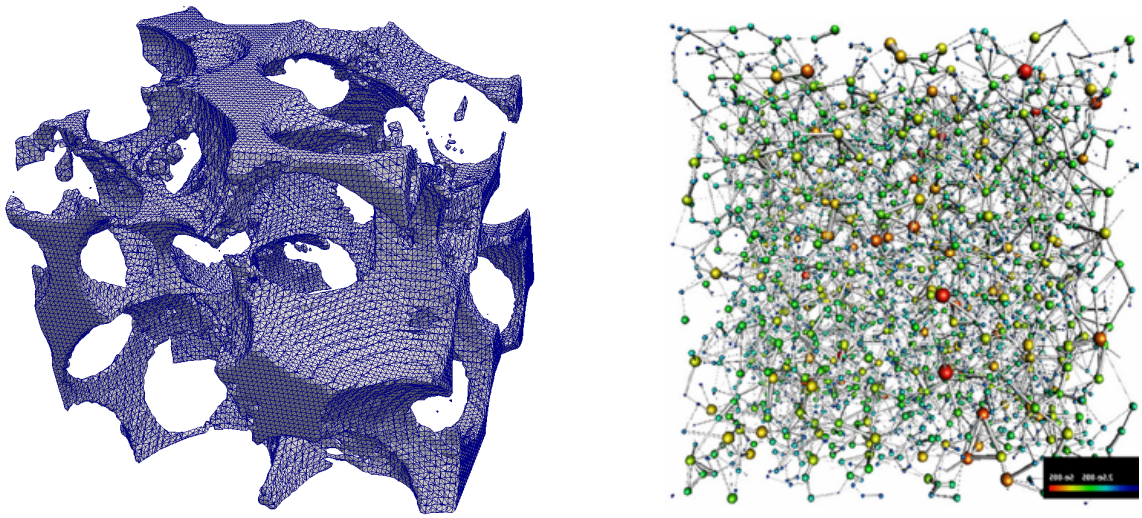

a) b)

Figure 4-4 a) Direct Modeling b) Network Modeling

The most computationally efficient flow model is the network modelling. Network modelling (Fig. 4.4b) has attracted particular interest in two-phase flows and especially for applications related with the oil & gas industry. For the network extraction modelling, initially the image geometrical description (or representation) has to be replaced by a simpler method than direct modelling taking into account pores and throats. In last decade, the developments in pore scale images drive the research for network extraction methods through complex porous media. Dong *et al* compared different network extraction models on 3D images and they presented a new model that they have developed in order to better represent complex porous medium [84]. Even if with network modelling the computational resources that are required are extensively lower than with direct modelling the uncertainty of network model that is used governs the skepticism for this method.

4.3. Using DSMC in micro-CT images

4.3.1 Pre-processing

As it was described previously, several tight and unconventional gas reservoirs have single phase flows within the transition and free molecular regime with Knudsen number greater than 0.1. Flows that belong to these regimes cannot be simulated with standard Navier-Stokes equations and new methods should be adopted. In previous chapter, it was described that the DSMC is the dominant method for simulating rarefied gas flows. Since tight gas

reservoirs incorporate rarefied gas flows, DSMC offers a great tool for predicting gas properties. For the first time (according to our best knowledge) the DSMC is applied on micro-CT images of rock samples using direct modelling. This will offer a better understanding of the flow physics at a pore scale in tight gas reservoirs. The knowledge that will obtained from the DSMC simulations in micro-CT images will give an in-depth knowledge for tight gas reservoirs.

The main challenge of simulations with direct modelling of the micro-CT images is the representation of the geometry in the OpenFOAM framework. The micro-CT scanning technology offers an excellent tool to capture and represent porous rocks with a resolution of some microns. The images that we are using have been obtained from different micro-CT laboratories and scanners. One of the biggest challenges in dealing with direct modelling is the computational effort of the simulations. A typical micro-CT porous medium image can have more than 2 million grid blocks. A typical DSMC simulation time-step takes usually five minutes for this number of blocks in a single intel XEON 3.2GHZ processor. Typical DSMC simulations require one hundred thousand time steps to converge. Even with recent advances in parallel computing with eight cores then this simulation would require more than forty days to finish. In principle, these simulations are unfeasible not only from cores resources but for memory as well. In order to minimize the computational time decomposition techniques are regularly used to decompose the mesh. This will give the option to run the simulations on inter-connected nodes (more than 2000) with reasonable higher memory.

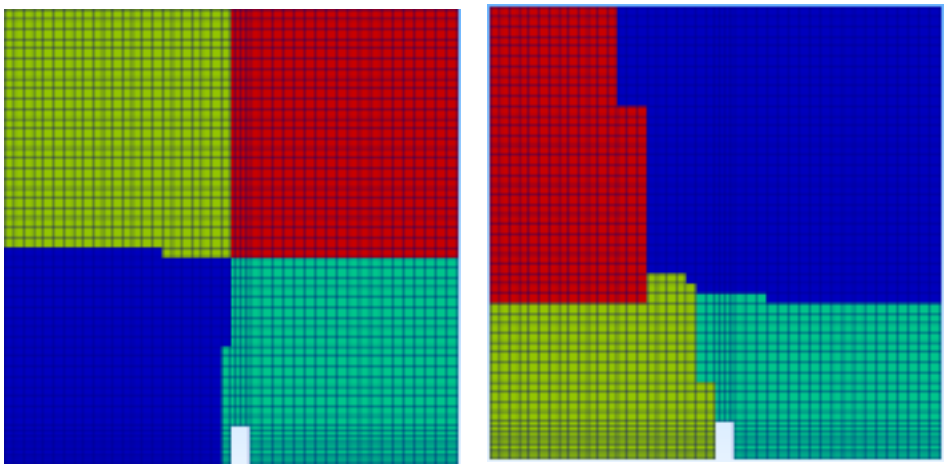

a) b)

Figure 4-5 Domain Decomposition a) Simple b) Scotch

In OpenFOAM there are several techniques to decompose the computational domain into sections according to the available number of cores. The method that is usually used is the *Simple* package (Fig.4.5a). It splits the domain into sections by direction. A new graph partitioning package that is called *Scotch* has been proved to be more efficient than *Simple.* The decomposition method splits the computational domain so that each processor has the same number of particles. It provides increased computational efficiency and improves the load balancing (Fig.4.5b). The *Scotch* in 64 processors offers reduction of computational time by over 35% in comparison with *Simple* technique. In cases like porous media obtained from micro-CT the decomposition method and parallel computing offers a useful tool to decrease the computational time. This will allow us to perform simulations on relatively big micro-CT images of porous rocks and make assumptions about macroscopic properties. We are using a Berea sandstone with resolution of 10μm. Each of the simulations are run on 64 processors in parallel. The *Scotch* package is used to decompose the computational domain and HPC is used.

4.3.2 Running Simulations

A Berea sandstone, 56nm wide, with over 1 million computational cells is benchmarked with DSMC. The 3D geometry was obtained using a microcomputed tomography (micro-CT) with size of 1024^3 voxels. The boundary surfaces as well as the rock and inlet gas temperatures are set to 300K. For all cases, we used fully diffuse reflection. In DSMC for the diffuse reflection the porous medium and velocity should be defined. Simulations contain, in all cases, 2 million DSMC simulator particles and solved in parallel with twelve

processors. All cases are pressure driven flow configuration with a set inlet pressure on the left-hand side and a set outlet pressure on the right-hand side as illustrated in Fig. 4.6. For all simulations, the gas is assumed to be methane where the properties are as given in Table 4.1. The gas-surface interaction model that was used in our simulations was the Maxwell model [3]. The variable hard sphere (VHS) collision model is used. The parameter, T is the temperature, m is the atomic mass, ξ is the fraction of $c\Delta t/\lambda$, ω is the temperature coefficient and d_{ref} *is* the species reference molecular diameter. The values of the T_{ref}, ω, ξ, *and* m are given in the table [35]. Initial velocity for all Knudsen numbers is the same. The Knudsen number variation is achieved by varying the density.

Table 4-1: Flow Simulations Details

Specie	λ	Tref (K)	ω	d_{ref}(x10^{-10}) (m)	m(x10^{-27}) (kg)	ξ	Time Step (s)
CH_4	VHS	300	0.84	4.83	26.63	6.4	1.3 x 10^{-8}

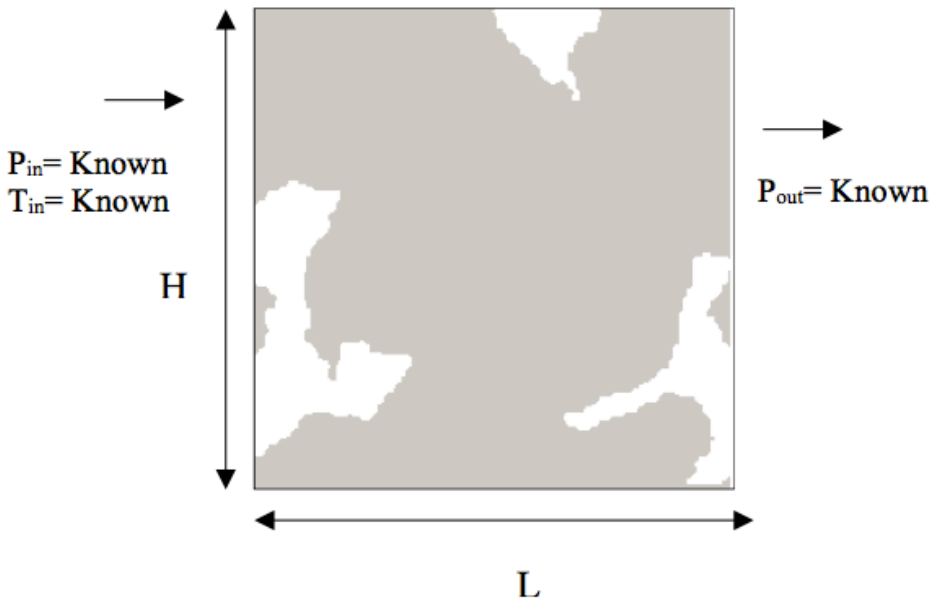

Figure 4-6 Simulations Configuration

Three different Knudsen cases have been tested as detailed in Table 4.2. For all the cases the cell size was smaller than the mean free path in order to meets the λ/3 criterion. The cases were run within OpenFoam [87]. The DSMC code that it has been used in the present work its part of this open source code software. OpenFOAM uses finite volume (FV) numerics to solve systems of partial differential equations ascribed on any three-dimensional unstructured mesh of polygonal cells. The 3D porous structure was imported in OpenFOAM to produce a three-dimensional unstructured mesh with polygonal cells to

solve the flow equations. The DSMC method is implemented in OpenFOAM in a parallel solver called *dsmcFoam*.

Table 4-2 Simulations Parameters

Case	Kn	Pin(Pa)	Pout(Pa)	Pin/Pout
I	0.037	300000	200000	1.5
II	0.37	30000	20000	1.5
III	3.7	3000	2000	1.5

The representation of the 3D geometry was obtained using ImageJ software. The rock type is the Berea sandstone (Fig. 4.7) in all cases. Figure 3 shows the pore volume in the model. Red arrow is X-axis, yellow is Y-axis and green is the Z-axis.

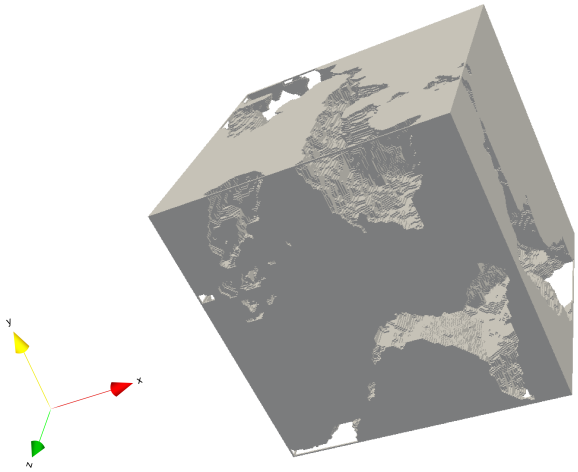

Figure 4-7 3D Simulated Berea Porous Sample

The normalized velocity profiles for the three cases are shown in Fig.4:8. For the Kn = 0.037 the velocity was normalized with the maximum velocity. The same procedure was followed for Kn = 0.37 and Kn = 3.7. The left side represents the inlet pressure and the right the outlet in all profiles. From the results, we observe a channel in the middle of the porous media where the maximum speed is achieved. Because of the porous media geometry, the empty space in the right corner affects the motion of the fluid and the maximum velocity. Furthermore, the empty space in the left upper corner prevents the fluid to travel in that channel. For a highly rarefied gas (Kn = 3.7) the maximum velocity is significantly smaller than for the smaller Knudsen number (Kn = 0.037). Near the outlet we observe a higher velocity again because of the outlet pressure and a parabolic shape. For a Kn = 0.37, in the early transition regime, the same phenomena can be seen but with not so high velocities at the three main points (inlet, middle, outlet) because of the lower

pressures intermolecular collisions are taking place less frequently. At Kn = 3.7 a more uniformly distributed velocity profile can be seen.

In order to demonstrate that the 20 particles per cell that were used in all simulations was the appropriate number, we investigate a case of Kn = 3.7 for 50 particles per cell. From Fig. 4.8d it can be stated that there is no noticeable difference with Fig. 4.8c where 20 particles per cell were used. Any small variation may be attributed to statistical noises. As a result of this the statistical noise that appears in the results depends mainly in the nature of the method and not on the simulated particles per cell. By increasing the simulated particles per cell, it wasn't observed any noticeable change on the properties of the gas (i.e velocity profile).

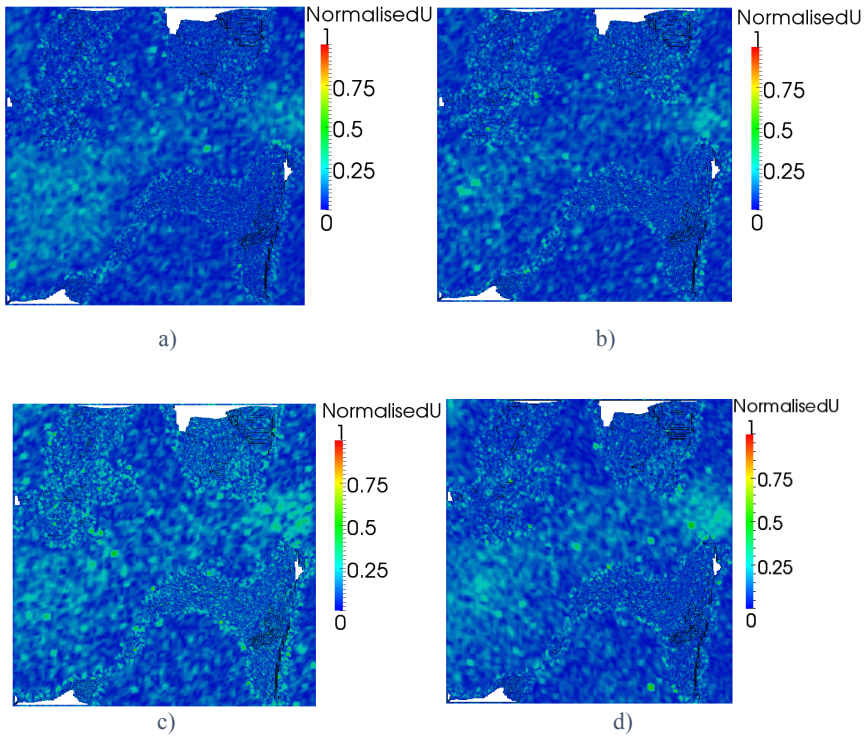

Figure 4-8 Velocity profile; a) Kn = 0.037, b) Kn = 0.37, c) Kn = 3.7, d) Kn = 3.7 (50 particles per cell)

The normalized velocity profiles in Fig. 4.9 are taken in a certain 2D (in the center) slice of the porous media. These show some statistical noises in the results, which increase as the Knudsen number increases. For a lower Knudsen number, with more simulated molecules in the simulation the statistical error is less than in higher Knudsen numbers where the number of simulated particles is more important. Because DSMC is a statistical based method, the number of simulated particles affects the results as mentioned previously. In order to solve these statistical noise problems, the number of simulated particles may be increased to a higher number than 20 particles per cell that were used in our cases. We also run a simulation for Kn = 3.7 with 50 particles per cell (Fig. 4.9d) and

compare with results with 20 particles per cell (Fig. 4.9c). The results indicate unnoticeable changes between the two. This is in agreement with previous author observations with regards to the appropriate number of simulated particles in a cell [53, 88]. Those studies were, however, for simple geometries like the lid-driven cavity configuration. Results from Fig. 4.9 indicate that the appropriate number of simulated particles per cell is between 20 and 50 even for complex geometries like this porous structure. The velocity is higher at the outlet for the lower Knudsen number case and follows a parabolic like shape. Fig. 4.9 shows the higher velocity occurs near the outlet. For Kn = 3.7, the red color near the outlet shows the existence of the highest velocity at the outlet. This higher velocity is shown in the cases of Kn = 0.37 and Kn = 3.7 by the green and yellow color respectively. The higher velocity is explained by the low pressure at the outlet [89]. The lowest velocities are observed near empty spaces for all three cases. The higher velocity occurs in a continuous area (no empty spaces) at the outlet of the porous structure for the three Knudsen numbers. It is observed, however, that for the higher Knudsen number, the velocity is more uniformly distributed with less difference between inlet and outlet. This may be attributed to less intermolecular collisions as the Knudsen number increases.

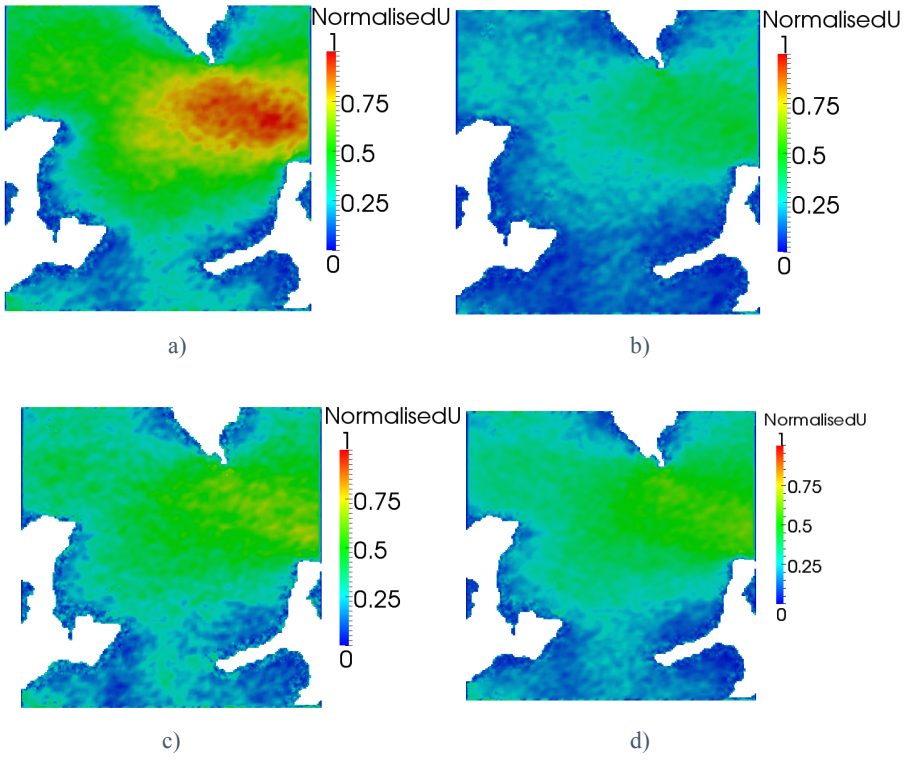

Figure 4-9 Velocity profile; a) Kn = 0.037, b) Kn = 0.37, c) Kn = 3.7, d) Kn = 3.7 (50 particles per cell)

Fig. 4.10 represents the velocity profile at the inlet of the porous medium. For Kn = 3.7 the profile is more uniform as the wall effects become important in the transport mechanism.

For Kn = 0.37 the velocity profile nearly follows the profile for Kn = 3.7. For Kn = 0.037 a parabolic like shape can be observed and the classical NSF behavior is approached. For all Knudsen numbers, the velocity near the walls is non-zero; demonstrating Klinkenberg slippage effects [40]. Previous authors have also noted that velocity profiles under these conditions are non-parabolic profiles [89].

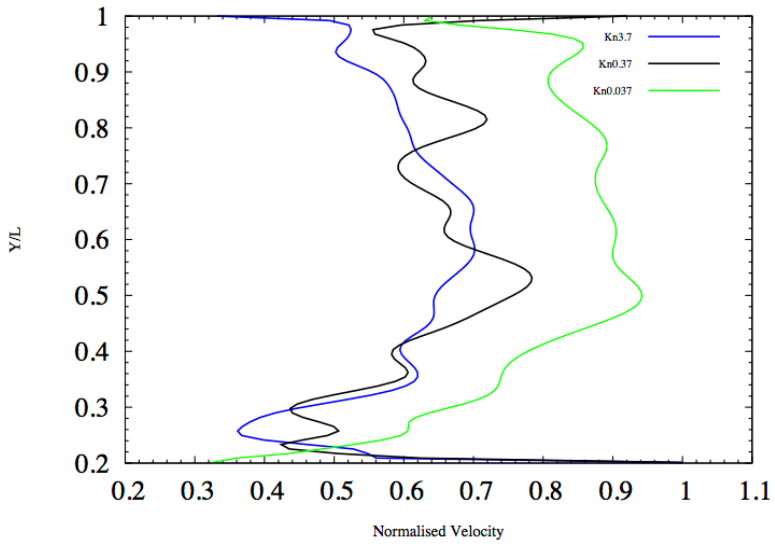

Figure 4-10 Normalised velocity profile in the pore cross-section at the inlet of the medium

Fig. 4.11 shows the velocity distribution at the center of the medium in the y direction. At the upper wall, it can be seen that the higher velocity is for a Kn = 0.37 and the lower for Kn = 0.037. However, nearly in the middle of the channel, Kn = 0.037 has the highest velocity while Kn = 0.37 has the lowest. This may be attributed in less intermolecular collisions that occur in higher Knudsen numbers. On the lower wall, as the Knudsen number increases the velocity increases. The velocity near the walls is non-zero showing the existence of slip. It is interesting to note that for all Knudsen numbers, at the center of the structure, the velocity profile is parabolic.

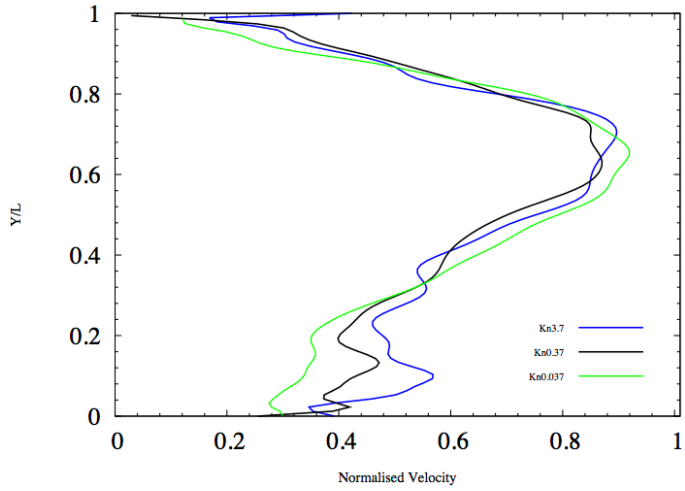

Figure 4-11 Normalised velocity profile in the pore cross-section at 1/2 of the medium

Fig. 4.12 shows the velocity profile on a cross section at the outlet of the porous structure. It can be observed that as the Knudsen number decreases, a more parabolic like shape is obtained. From these results the inadequacy of NSF is for Kn > 0.1, since the classical parabolic-like shape is approached for Knudsen numbers lower than that value [89]. The loss of the parabolic like shape may be attributed to more gas-wall interactions.

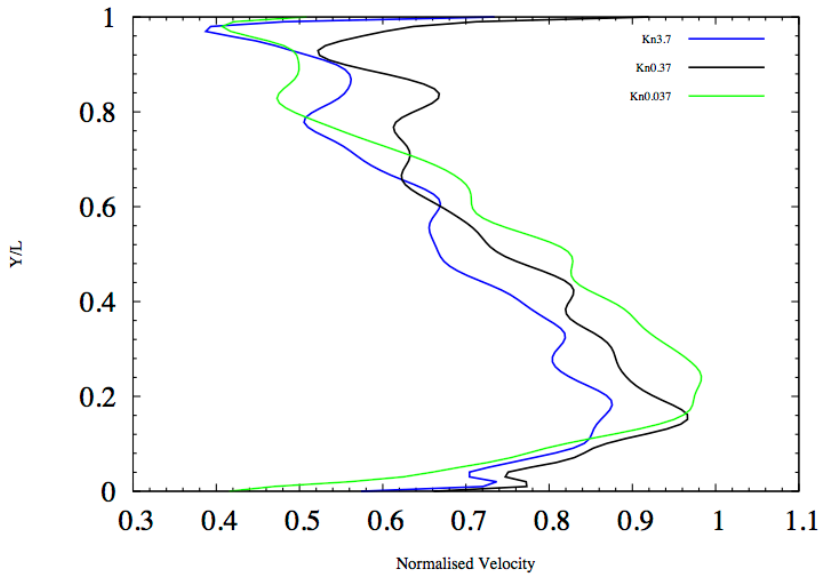

Figure 4-12 Normalised velocity profile in the pore cross-section at the outlet of the medium

Summarizing the above, from the velocity profile it can be concluded that Knudsen number plays an important role in the whole porous strata. As the Knudsen number decreases, a more parabolic like shape can be observed for the three sections (inlet, middle, and outlet). This is more pronounced at the outlet of the flow domain. The parabolic like shape decrease as the Knudsen number increases. Firouzi *et al.* showed previously that as pores become smaller the velocity profile does not follow the classical NS parabolic like shape [89].

Figure 4.13 represent the computed normalized pressure profiles for the three cases. For Kn = 0.037 the pressure was normalized with the maximum pressure of 4077501Pa. The same procedure was followed for Kn = 0.37 and Kn = 3.7 where the maxima were 451779Pa and 43212Pa respectively. The pressure profiles for the three different Knudsen numbers do not show a significant change in our simulations, as the ratio inlet/outlet is constant. Higher pressures can be observed near empty space surfaces where compression phenomena occur.

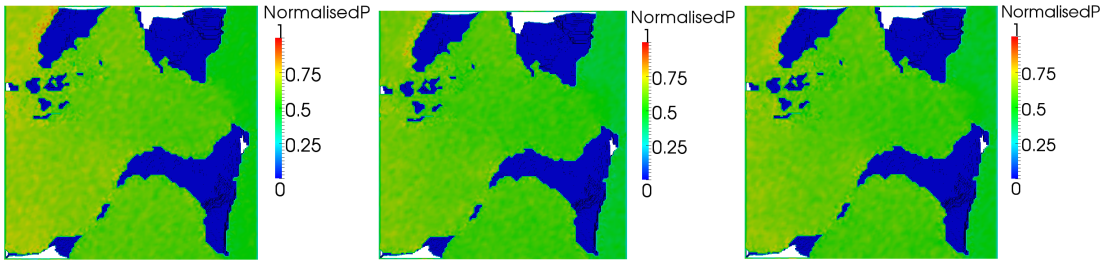

a) *b)* *c)*

Figure 4-13 Pressure Profile; a) Kn = 0.037, b) Kn = 0.37, c) Kn = 3.7

Fig. 4.14 shows the pressure distribution across the middle and in X direction. For the three different cases a pressure drop can be observed at the outlet, which is the result of the inlet/outlet pressures ratios that have been set for all cases to the same, i.e at a ratio of 0.6. The similarity observed between the different pressure profiles for the three different Knudsen numbers may be explained by the same constant inlet/outlet ratio used in the three cases.

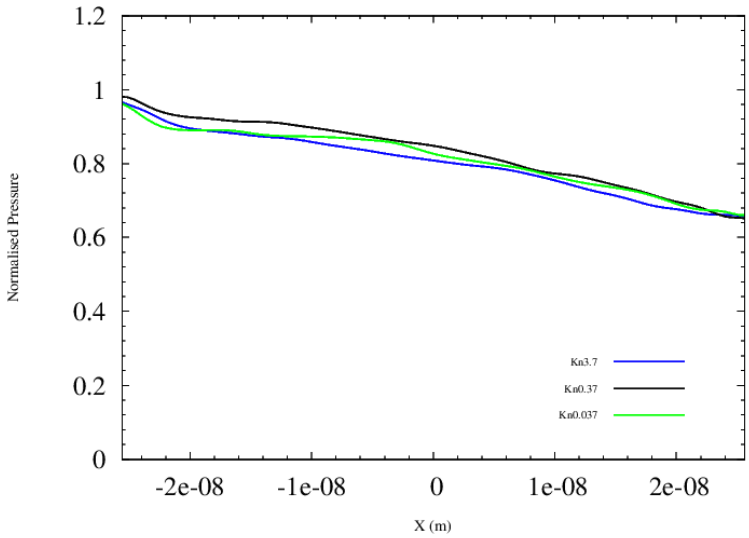

Figure 4-14 Normalised Pressure Profile

Fig. 4.15 shows the normalized temperature profiles for the three cases. For the Kn = 0.037 the temperature was normalized with the maximum temperature of 456K. The same procedure was followed for Kn = 0.37 and Kn = 3.7 where the maxima were 432K and 415K respectively. For all the case an almost uniformly distributed temperature is observed. We also observed that, as the Knudsen number increases the maximum temperature decreases. We note that intermolecular collisions become more frequent as the Knudsen number decreases, which may explain the maximum temperature rise. There is a decrease of 23 degrees from Kn = 0.037 to 0.37 and 15 degrees from Kn = 0.37 to 3.7.

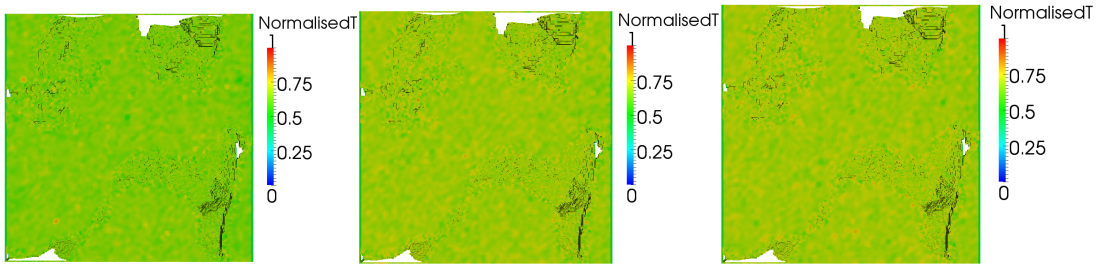

a) *b)* *c)*

Figure 4-15 Temperature Profile; a) Kn = 0.037, b) Kn = 0.37, c) Kn = 3.7

Figure 4.16 shows the temperature distribution across the middle of the porous structure. The results are in full agreement with the 3D profiles for the three different cases. The temperature stays constant along the system.

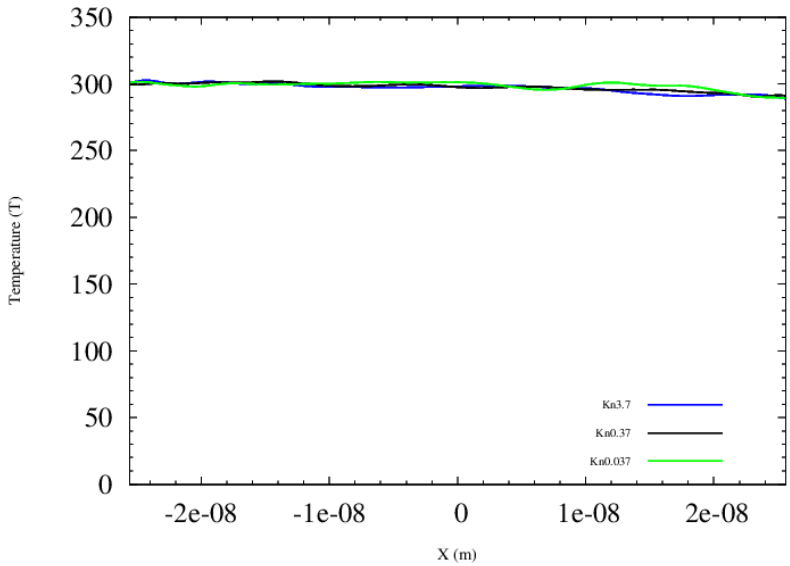

Figure 4-16 Temperature Profile

4.4. Permeability laws in tight porous media

In 1856, French engineer Henry Darcy first provided a relation which permits the measurement of fluid flow through porous media [90]. The ability of a fluid to pass through the interconnected pore spaces of a rock denotes the degree of permeability possessed by the rock formation and it should be noted that Darcy permeability is purely a function of pore geometry. Darcy also recognized that for the measurement of fluid flow through porous media, the force which causes the fluid to flow (pressure gradient) and the viscosity μ of the flowing fluid must also be taken into consideration. Darcy's law is given as:

$$Q = \frac{kA_{xsa}\overline{P}}{\mu L} \tag{4.1}$$

Klinkenberg was the first person in the oil industry to identify the phenomena of slip [40]. He discovered that the rate of fluid flow through porous media at very low pressures (such as in low pressure gas shales) was actually more than predicted by Darcy's law. He hypothesized that this was because under these conditions the velocity of molecules along the pore walls is not zero and this occurs when the diameter of the pore approaches the mean free path of the gas. Klinkenberg proposed the following equation for apparent (effective) gas permeability k_a which takes into account the additional consideration of gas slippage:

$$k_a = k_\infty \left(1 + \frac{b_k}{\overline{P}}\right) \tag{4.2}$$

where $\overline{P}$ is the average pressure, and k_∞ is the reference/intrinsic permeability, which is purely a function of pore geometry, and is given by:

$$k_\infty = \frac{\phi {r_p}^2}{8\tau} \tag{4.3}$$

where r_p is the pore radius, ϕ the porosity and τ the tortuosity factors [91]. The slippage factor b_k relates to the mean free path of the gas and is given by:

$$b_k = \frac{4c\lambda\overline{P}}{r_p} \tag{4.4}$$

where $c \approx 1$.

Klinkenberg approach generally works well in slip flow regimes. Few studies have been undertaken investigating fluid flows in the transition region. In 1999, Beskok and Karniadakis published their work which looked at rarefied gas flows in a wide range of Knudsen number ($0 \leq Kn < \infty$) (Beskok & Karniadakis, 1999). This enabled Civan and Florence to approximate apparent permeability as a function of Knudsen number. Civan's equation is as follows [91]:

$$b_k = \frac{4c\lambda\overline{P}}{r_p} \tag{4.5}$$

$$k_a = k_\infty \left(1 + \alpha_o \left(\frac{Kn^B}{A + Kn^B}\right) Kn\right)\left(1 + \frac{4Kn}{1 + Kn}\right) \tag{4.6}$$

Extracting the data provided by Civan for flows in the transition region: A = 0.178, B = 0.4348 and α_0 = 1.358.

The model derived by Florence for transition flow can be expressed as [92]:

$$k_a = k_\infty(1 + 4Kn) \tag{4.7}$$

It is clear that, from Eq. 4.6 and Eq. 4.7 apparent gas permeability in porous media depends on Knudsen number.

The present study takes an analytical approach towards generating a new Knudsen number which complies with Cooper *et al.* experimental data and thus providing enhanced solutions to Knudsen number dependent apparent gas permeability correlations.

4.4.1 Mean Free Path Analysis

Expressions for the mean free path of a gas differ between researchers, although similarities do exist. The mean free path expressions investigated in this work all contain the following common factor:

$$\overline{\lambda} = \frac{\mu\sqrt{2RT}}{P} \tag{4.8}$$

Maxwell provides two correlations for the mean free path of a gas. The first is [50]:

$$\lambda = 2\left(\frac{2P}{\pi\rho}\right)^{\frac{1}{2}} \cdot \frac{\mu}{P} \tag{4.9}$$

The density in Eq. 4.9 can be eliminated in favour of the pressure via use of the ideal gas law:

$$P = \rho RT \rightarrow \rho = \frac{P}{RT} \tag{4.10}$$

Therefore, Maxwell's first expression becomes:

$$\lambda = 2\left(\frac{2PRT}{\pi P}\right)^{\frac{1}{2}} . \frac{\mu}{P} = \frac{2}{\sqrt{\pi}} \times \bar{\lambda} \tag{4.11}$$

The second correlation Maxwell provides is as follows:

$$\lambda = \frac{3}{2}\mu\left(\frac{\pi}{2P\rho}\right)^{\frac{1}{2}} \tag{4.12}$$

Again, eliminating the density in favor of the pressure via the ideal gas law furnishes the expression:

$$\lambda = \frac{3}{2}\mu\left(\frac{\pi RT}{2P^2}\right)^{\frac{1}{2}} \tag{4.13}$$

Multiplying Eq. 4.13 by $\sqrt{2}/\sqrt{2}$ to obtain $\bar{\lambda}$ yields:

$$\lambda = \frac{3\sqrt{\pi}}{4} \times \bar{\lambda} \tag{4.14}$$

Roy and Bird both provide a correlation for the mean free path of a gas using the Chapman-Enskog expansion for the coefficient of viscosity in a hard sphere intermolecular collision model gas [37]. Roy's expression is as follows [81]:

$$\lambda = \frac{\mu}{\rho}\sqrt{\frac{\pi}{2RT}} \tag{4.15}$$

Application of the ideal gas law to eliminate the density yields:

$$\lambda = \frac{\mu RT}{P}\sqrt{\frac{\pi}{2RT}} = \sqrt{\frac{\pi}{2}}\mu\frac{\sqrt{RT}}{P} \tag{4.16}$$

Multiplying Eq. 4.16 by $\sqrt{2}/\sqrt{2}$ to obtain $\overline{\lambda}$ gives:

$$\lambda = \frac{\sqrt{\pi}}{2} \times \overline{\lambda} \tag{4.17}$$

Bird's expression is as follows [93]:

$$\lambda = \frac{16\mu}{5} (2\pi RT)^{-\frac{1}{2}} / \rho \tag{4.18}$$

Applying ideal gas law yields:

$$\lambda = \frac{16\mu}{5\sqrt{2\pi RT}} \frac{RT}{P} = \frac{16\mu}{5\sqrt{2\pi}} \frac{\sqrt{RT}}{P} \tag{4.19}$$

Multiplying Eq. 4.19 by $\sqrt{2}/\sqrt{2}$ to obtain $\overline{\lambda}$ gives:

$$\lambda = \frac{16}{5(2\sqrt{\pi})} \frac{\mu\sqrt{2RT}}{P} = \frac{8}{5\sqrt{\pi}} \times \overline{\lambda} \tag{4.20}$$

Ewart also uses a mean free path expression similar to that of the hard sphere model [94]:

$$\lambda = \sqrt{\frac{\pi}{2}} \frac{\mu}{P} \sqrt{2RT} \tag{4.21}$$

where the mean free path coefficient of Ewart is:

$$k_{\lambda E} = \sqrt{\frac{\pi}{2}} \tag{4.22}$$

leading to mean free path:

$$\lambda = k_{\lambda E} \times \overline{\lambda} \tag{4.23}$$

The various mean free path expressions are summarized in Table. 4.3 and presented schematically in Fig. 4.17 using Cooper *et al.* experimental data set which is described in following sections.

As demonstrated in Fig. 4.17, the Knudsen number follows a similar trend for each author – the Knudsen number steadily decreases as pressure increases. However, the Knudsen number range varies significantly for Cooper *et al.* experimental data set. The ratio of highest Maxwell (2) to lowest (Roy) is 3:2. The same ratio can be obtained using the values for the highest and lowest mean free path coefficient k_λ presented in Table 4.3.

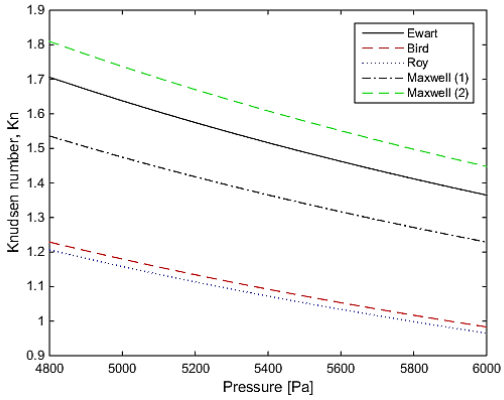

Figure 4-17 Variation of Knudsen number across Cooper et al. *experimental range using the different mean free path expressions.*

Author	k_λ	k_λ *[value]*
Ewart	$\sqrt{\frac{\pi}{2}}$	1.25
Bird	$\frac{8}{5\sqrt{\pi}}$	0.90
Roy	$\frac{\sqrt{\pi}}{2}$	0.89
Maxwell (1)	$\frac{2}{\sqrt{\pi}}$	1.13
Maxwell (2)	$\frac{3\sqrt{\pi}}{4}$	1.33

Table 4-3 Summary of the different coefficients k_λ *to the common factor,* $\overline{\lambda}$.

4.4.2 A Homogeneous Knudsen Number Approach

An expression for the mass flow rate through a rectangular micro/nano-channel based upon volume diffusion theory accounting for slip and Knudsen diffusion is given in [68]:

$$\dot{M} = \frac{wh^3 P_o^2}{24 L \mu_g RT}(P^2 - 1)\left[1 + AKn_o \frac{1}{P+1} + BKn_o \frac{lnP}{P^2 - 1}\right] \tag{4.24}$$

where the various coefficients appearing therein are described in Table 3. The mass flux expression from Eq. 4.24 is obtained by dividing through by area ($h \times w$) and leads to:

$$J = \frac{h^2 P_o^2}{24 \mu LRT}(P^2 - 1)\left[1 + AKn_o \frac{1}{P+1} + BKn_o \frac{lnP}{P^2 - 1}\right] \tag{4.25}$$

A	B	P	Kn_o	K_{slip}
$12K_{slip}$	$\frac{24}{Prk_\lambda^2}$	p_i/p_o	$k_\lambda \bar{\lambda}_o/d_p$	$\frac{\sqrt{\pi}}{2}\times\frac{\sqrt{2}}{k_\lambda}$

Table 4-4 Summary of the different coefficients (k_λ) to the common factor, $\bar{\lambda}$.

In Eq. 4.25, the hydraulic radius r_h may be used. The hydraulic radius is defined as the flow area divided by the wetted perimeter of the conduit. If the cross-sectional area of the tube is assumed to be a square, r_h is obtained by the expression:

$$r_h = \frac{h^2}{4h} = \frac{h}{4} \tag{4.26}$$

Rearranging equation (4.26) yields:

$$h^2 = 16r_h^2 \tag{4.27}$$

Therefore, the mass flux of a fluid through a cylindrical pipe can be calculated using the Dadzie and Brenner model in the following form:

$$J = \frac{2{r_h}^2 P_o^2}{3L\mu RT}(P^2-1)\left[1 + AKn_o\frac{1}{P+1} + BKn_o\frac{lnP}{P^2-1}\right] \tag{4.28}$$

Cooper *et al.* provided an experimental data set studying the relationship between mass flux and pressure drop for argon gas in a straight cylindrical nanotube [95]. They determined slip coefficient for tubular carbon structures that have been produced by chemical vapor deposition on a porous alumina substrate. Commercially available porous anodic alumina filters (Whatman Anodisc) were used. After heating the tube to temperatures of 700, 750 and 800 °C in flowing argon, ethylene was introduced into the system at a flow rate of 150sccm (standard cubic centimeter per minute, cm^3/s). Characteristics of Cooper *et al.* nanotube experiments are disclosed in Table 4.5:

T	r_h	L
300 [K]	117.5 x 10^{-9} [m]	60 x 10^{-6} [m]
μ	P_o	Pr
2.22 x 10^{-5} [Pa s]	4800 [Pa]	0.68

Table 4-5 Characteristics of Cooper et al. *experimental set-up.*

Application of the mass flux Eq. 4.28 relative to Cooper *et al.* experimental data allows a consistent Knudsen number to be established. The solution of Eq. 4.28 is calculated using the value of k_λ for each author previously obtained. So that the theoretical values for each author lie in agreement with Cooper *et al.* experimental data, k_λ is multiplied by an alteration factor α. Table 4.6 summarizes this analysis. We obtain as a result $\alpha \times k_\lambda \approx 6.0$ the new coefficient to $\overline{\lambda}$ for determining the mean free path that results in the same Knudsen number range among all authors. In other words, the actual Knudsen number range corresponding to same values among all authors and in agreement with Cooper *et al.* experiments and Eq. 4.28 is now 6.69-8.36.

Table 4-6 Summary of values achieved following correction using mass flux Eq. 4.28 and Cooper et al. *data.*

Author	$\lambda = k_\lambda \times \overline{\lambda}$ $[10^{-7}]m$	Kn Range	α	λ x α $[10^{-6}]m$	New Kn Range
Ewart	3.28 - 4.09	1.39 - 1.74	4.80	1.57 – 1.97	6.69 – 8.36
Bird	2.36 - 2.95	1.00 - 1.25	6.68	1.57 – 1.97	6.69 – 8.36
Roy	2.32 - 2.89	0.98 - 1.23	6.80	1.57 – 1.97	6.69 – 8.36
Maxwell (1)	2.94 - 3.38	1.25 - 1.57	5.34	1.57 – 1.97	6.69 – 8.36
Maxwell (2)	3.47 - 4.34	1.48 - 1.85	4.53	1.57 – 1.97	6.69 – 8.36

Figure 4.18 presents the resulting mass flux from Eq. 4.28 and the experimental data. The flux model provided by Javadpour [26] and the Hagen-Poiseuille flow (K/HP) analytical solution by Guo are also included in this comparison [96]. Agreement between Dadzie & Brenner corrected theoretical model and the experimental data is shown in Fig 4.18. This model was previously reported to predict mass flow rate in microchannel up to *Kn* of 5 based on Eq. 4.24. It is adopted here for the analysis as it accounts for slip and Knudsen diffusion. The agreement in Fig. 4.18 is better than Javadpour and the K/HP, and becomes less accurate for high pressure differences.

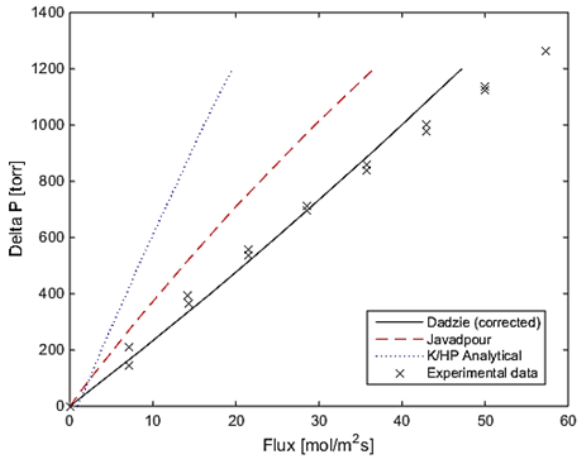

Figure 4-18 Comparison between K/HP analytical solution, Javadpour's model (with tangential accommodation coefficient equals to one), Dadzie and Brenner's corrected model, and experimental data for pressure difference versus flux [95].

In order to assess the validity of our correction with regards to the Knudsen number, the corrected apparent permeability models are compared with original models proposed by Civan and Florence [91, 92]. This is shown in Fig. 4.19a and Fig. 4.19b.

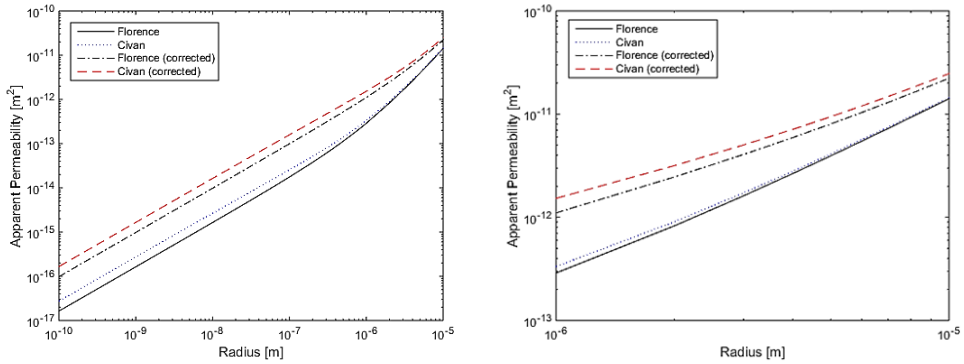

a) *b)*

Figure 4-19 a) Comparison of apparent permeability versus radius between corrected models and original models and b) in the transition regime

4.5. Summary

We have investigated the application of rarefied gas flows through porous media. Rarefied gas flows through porous media can be found in applications for the oil and gas industry and planetary sciences. Tight and unconventional gas reservoirs often lie in the transition regime. In addition, comets outgassing also fall in the transition and free molecular regime. The breakdown of continuum methods in such flows through porous media can be shown

by the collapse of Darcy Law in order to predict permeability especially in tight porous media.

The representation of porous media in computational methods which remains a challenge is achieved by using the micro-CT technology. We have used this technique in direct modelling with DSMC for simulations of gas flows. This was the first time that the micro-CT was applied in DSMC method. For a porous media with such a complex geometry, it showed that Knudsen number plays an important role for the velocity profile. The profile of the pressure and temperature show some similarities and for the three different cases. The temperature remains constant in the system with a slight decrease at the outlet for the three cases across the x direction. The pressure follows the same profile for all cases with a decrease that was set at the initial condition. Slight increase is observed at the middle of the profile demonstrating presence of empty space in the center. For all the Knudsen numbers, the parabolic-like shape is observed at the inlet and the middle of the channel for the geometry considered. As the Knudsen number increases the parabolic shape become non-obvious at the outlet. The Klinkenberg effect is also investigated for the different Knudsen numbers. Future work in this area using the direct simulation Monte Carlo method could include extending the study of gas transport to different samples of porous structures, like carbonates and other samples from tight gas formations. This would extend this investigation of the gas flow in porous media at micro and nano-scales.

Further to the simulation of DSMC in micro-CT images in rarefied gas flows we have presented an analytical solution of the various permeability laws. It is reported that the valuation of the mean free path of a gas and thus the Knudsen number affects the interpretation of experimental data for permeability laws. Various correlations for quantifying the mean free path of a gas were summarized and compared in this work. Using experimental data provided by Cooper *et al.*, and Dadzie & Brenner mass flow rate theoretical model, a new alteration factor has been introduced for the mean free path to characterize gas flow in nanotubes/shale-strata in the transition flow region. The effects of this modification were explored using Knudsen number dependent permeability correlations postulated by previous investigators. Results demonstrate a considerable discrepancy in the permeability numerical value. Similar investigations may be conducted using other mass flow rate equations such as those based on a direct solution to the Boltzmann kinetic equation.

The recent advances in oil & gas industry and especially the exploration and production from unconventional gas reservoirs have emerged the research in rarefied gas flows through porous media. There have been performed only a few studies regarding such flows and in

more detail using DSMC. The recent developments in High Performance Computers (HPC) allowed us to run in parallel direct modelling simulations using particle based methods (DSMC). The inappropriateness of continuum methods can be proved by the failure of Darcy law in predicting the permeability and the comparison with experimental or historical data from natural gas reservoirs. Further to the applications in oil & gas industry the latest missions in exploring comets (i.e comet 67P Churyumov/Gerasimenko) have made the understand of physics in such flows essential. The application of high porosity micro-CT images in DSMC will definitely help scientist to understand the outgassing in comets.

Chapter 5

5.Micro- and Nano-scale applications

Since the two presented models in Chapter 3 are newly developed set of equations it is important to test them as for the theory and the developed CFD code. We compare results from them against experimental data, analytical solutions and numerical results from DSMC which is the dominant method for simulating rarefied gas flows. In the absence of any experimental data, the DSMC will serve as the benchmarking method.

5.1. Introduction

All methods are developed using computer simulations. The computer usage in our days plays an increasingly important role for solving fluid mechanics problems. With the help of High Performance Computers (HPC) the computational efficiency faced a considerable grow. This allowed scientists to solve complex problems in a wide range of different applications.

Each newly developed CFD solver has to be tested for its accuracy and reliability. In order for the computational codes to considered reliable they have to have to pass through several test and processes of verification and validation. This will allow us comparing the results from newly developed models with other well-established methods.

As for the validation procedure, we aim to compare results with experimental data (when available), analytical solution and numerical results from our DSMC codes or other DSMC results available in the literature. In house DSMC code is based on dsmcFoam with adding some new equations in order to calculate heat flux vectors. Since *HWrhoCentralFoam and CCrhoCentralFoam are* a newly CFD codes (based on pre-existing code) they should be verified and validated. Navier-Stokes will be the reference for improvement in the results. Most of the benchmark cases represent the challenge that Bi-velocity and Korteweg numerical models face as they most capture non-equilibrium effects, flow physics, Knudsen layers, anti-Fourier flux, expansion cooling phenomena and Knudsen paradox.

5.2. Applications

The validation of the new CFD codes will come through an emerging engineering and energy field; the gas flow through microscale applications.

The use of micro- and nano- electromechanical systems (MEMS/NEMS) has faced rapid increase as it has generated extensive research in fluid flows in ultra-small devices. Gas flows at micro- and nano-scale involve complex processes due to rarefaction, important gas-surface interactions, and inter-molecular collisions [5]. With advances in nano- and micro-electromechnical systems (MEMS/NEMS) in fabrication technology, understanding new mass and heat transfer processes in rarefaction regimes is of another great interest. Accurate modelling of gas flows at micro/nano scale involve in principle accurate modelling of rarefaction, gas-surface interactions and inter-molecular collisions [5]

Classical continuum fluid equation models like the standard Navier-Stokes fail to describe flows under these conditions [97]. Gas flows in MEMS and NEMS are usually in the slip ($0.001 \leq Kn \leq 0.1$) and transition regimes ($0.1 \leq Kn \leq 10$) where atmospheric pressures can occur. In order to describe micro- and nano-scale flows, the Boltzmann-like kinetic equation for dilute gases is often adopted [98]. Due to the complexity of the collision term in the Boltzmann equation, approximation methods are often used. As the Knudsen number increases beyond the slip regime, NSF loses its validity. Molecular dynamics (MD) can capture nano-scale interactions and provide some accurate results. However, even with the capability of High Performance Computers (HPC), MD simulations can be extremely costly in terms of computational time. Moreover, time step in MD are restricted to femtoseconds and this could lead to thousands of years of CPU time [81]. Prediction of micro-channel flows using DSMC was carried out by Xue *et al.* and compared with Navier-Stokes [99]. They concluded that the analytical solution of Navier-Stokes equations fails to predict flow due to the breakdown of the continuum assumption. Several other studies were carried out using DSMC to investigate the lid-driven cavity flow in transition and slip regimes. Mizzi *et al.* provided DSMC flow features in the cavity in the slip flow regime [100]. General agreement is reported between NSF and DSMC at Kn=0.02 and 0.05 in the velocity fields and differences for the temperature fields. Though understanding counter-gradients heat transfer mechanism exhibited in the DSMC flow contours are still indistinct and are not predictable by NSF. Boundary treatment is determinant in DSMC flow feature predictions[101] . White *et al.* benchmarked DSMC for gas flow through micro-channels with bends and demonstrate importance of the mesh size in corner regions in order to capture the size and shape of recirculation zones [102]. DSMC was also used to investigate gas flows in vacuum packaged MEMS devices by Lui *et al.* where it was shown that heat-

transfer is weakened by rarefaction effects [103]. The significant impact on the direction of heat transfer with any increase in incomplete surface accommodation in a lid-driven cavity was stated later by John *et al* [104]. Mohammazadeh *et al.* simulated a micro cavity using DSMC and NSF. They showed the existence of unconventional heat transfer mechanism in the middle of slip flow regime. Furthermore, they concluded that the NSF equations are not accurate for a cavity flow for Kn < 0.1 [12]. Akhlaghi *et al.* studied recently wall heat transfer effects on the thermal behavior of Poiseuille flows with DSMC in micro/nanochannels and proved the existence of cold-to-hot heat transfer process in the cooling wall cases [105].

5.2.1. Lid-Driven Cavity for Bi-velocity (*HWrhoCentralFoam*)

The lid-driven cavity problem is a fundamental configuration involving a simple geometry. It is often used for validation, benchmarking and testing new methods. Some previous studies showed the complexity involved in a lid-driven cavity flow in rarefied gases under non-equilibrium effects [12]. In the absence of experimental data, results obtained using DSMC are used to compare with extended hydrodynamic equations. Here we used the lid-driven cavity problem to demonstrate how a volume diffusion continuum model can capture non-local-equilibrium phenomena in high Knudsen number heat transfer problems. This will be the first step for validation of the code and the theory.

The lid-driven cavity problem considered is shown in Figure 5.1 and investigated at different Knudsen numbers. The top driven lid (B-C) moves in x direction with a fixed velocity $\mathbf{U_w}$= 100 m/s while all other walls are stationary. All wall temperatures are set to a uniform value of T_w= 273K in all cases. Table 1 summarizes the set-up conditions for the proposed problem. The cavity is of length $L = 10^{-7}m$. A monoatomic argon gas is used. The different Knudsen number was achieved by varying the pressure. Even though experimental data are not available for the proposed problem, it is used as a benchmark for new models. Furthermore, the violation of Fourier law even for low Knudsen numbers is a critical test for investigating new methods. Three different cases are tested with NSF and DSMC [106].

Table 5-1 Case Properties

Gas	Temperature (K)	Initial Velocity (m/s)	L (m)	Wall Boundaries
Argon	273	100	10^{-7}	*Fully Diffuse*

For Bi-Velocity the mesh containing 160 cells in each direction was selected after the results for ρ and T converged on the mesh of 100 cells. The courant number, C_r was set to

0.5 for all cases as for the continuum methods. The DSMC grid containing 200 x 200 cells is selected for the reported results [107]. The cell size is kept in all cases less than the mean free path (λ) as suggested by G.A.Bird [35]. The variable hard sphere (VHS) model is used for the DSMC and the collision pairs are chosen based on the no time counter (NTC) method [47]. Fifty particles per cell were initially set for all the cases in order to minimize the statistical noise.

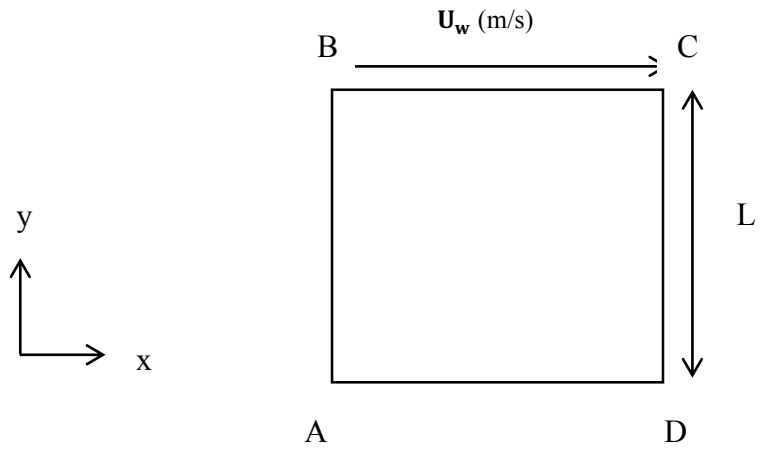

Figure 5:1 Configuration of the micro cavity flow problem

Classical NSF is well known to be unable to capture flow features in transition regime (Kn > 0.1) even when corrected with slip-jump boundary conditions. A lid-driven cavity problem was investigated and compared between DSMC and regularized 13 moments equations (R13) [12]. It was shown that R13 equations describe temperature and heat flux compared to DSMC up to Knudsen number 0.1. The unconventional cold-to-hot heat transfer was observed for Kn > 0.05. Here we run our new bi-velocity (or volume diffusion) solver for three different cases: Kn = 10, Kn = 1 and Kn = 0.1. These are higher Knudsen numbers compared with the previous studies [108].

The boundary conditions for temperature jump and velocity slip that were imposed are those presented in the previous chapter.

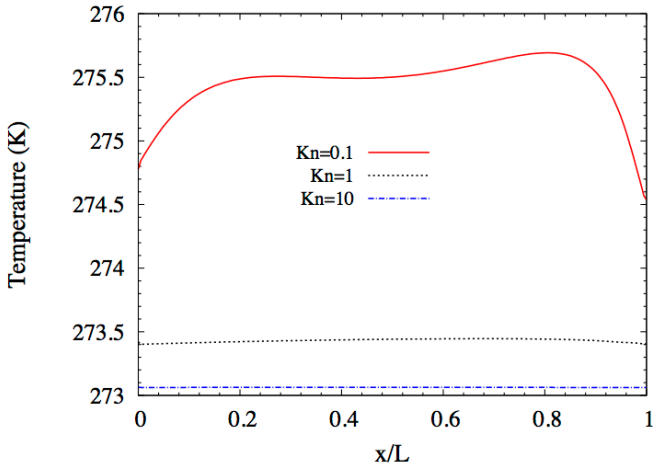

a)

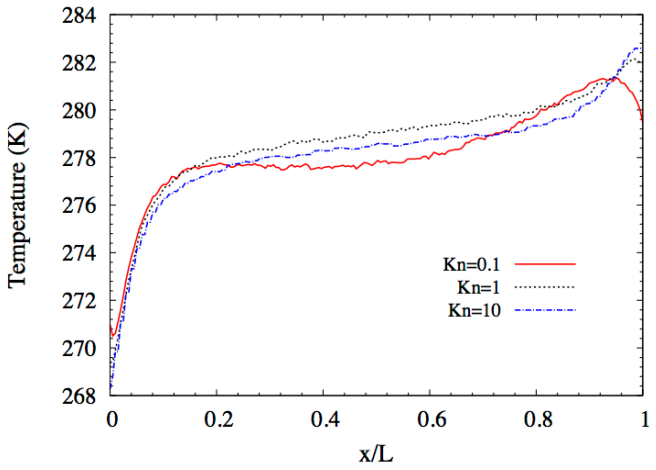

b)

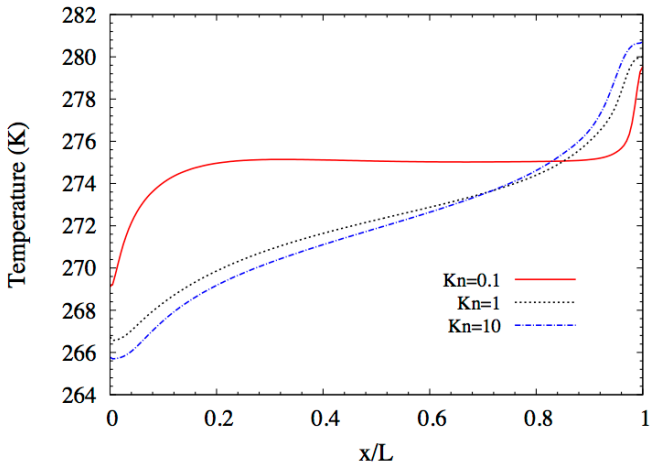

c)

Figure 5-2 Temperature variation comparisons of three different models a) NSF b) DSMC and c) Bi-Velocity

We start our investigation by first comparing the temperature profile among the Navier-Stokes, DSMC and Volume-Diffusion for all Knudsen numbers among a center-line of the

cavity. Standard NSF (Fig.5.2a) shows slight variation for Kn = 0.1, with a maximum temperature two degrees higher than the initial conditions. The left and right walls are predicted to be in relatively non-equilibrium conditions. As the Knudsen number increases and goes to the transition and free molecular regimes the standard NSF do not predict any change in the temperature distribution and confirms their inapplicability in such high Knudsen numbers (Kn > 1). DSMC (Fig.5.2b) and Volume Diffusion (Fig. 5.2c) show that in all Knudsen numbers, both walls are in non-equilibrium state. Both methods can predict very good temperature variations. However, Volume-Diffusion shows that the Knudsen layer is thicker for Kn = 1 and Kn = 10 than the one predicted by DSMC.

Numerical results are presented below in the slip and transition flow regimes. For each Knudsen number entropic heat flux and energetic heat flux are depicted and compared with DSMC heat flux.

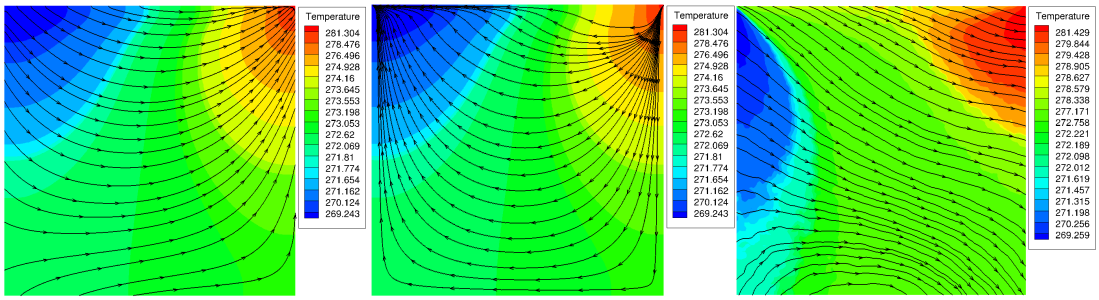

a) *b)* *c)*

Figure 5-3 Energetic heat flux a) and entropic heat flux b) lines overlaid on the temperature contour for Kn = 10 in comparison with DSMC heatflux c)

Figure 5.3 compares heat flux lines overlaid the temperature contours. First, we observe that the entropic heat flux from the volume diffusion model displays a flow from the higher temperature corner to the lower temperature corner (Figure 5.3b), which is in perfect agreement with the Second Law. The phenomenon of cold-to-hot heat transfer concerns the energetic heat flux (Figure 5.3a). While the DSMC heat transfer also shows a heat flux from cold-to-hot, our new model predicts a more consistent energetic heat flux clearly from the left corner to right corner. The unconventional cold-to-hot heat transfer in the energetic heat flux is attributable to the additional term in the heat flux. The predicted temperature distribution is in general agreement with the DSMC. Equal minimum and maximum temperature was predicted from the two methods. The minimum temperature is decreased by four degrees from the initially set conditions, which shows strong non-equilibrium effects in the left corner. The expansion-cooling phenomenon occurring on the left wall shows that the gas temperature becomes lower than the wall temperature ($T_g < T_w$). Another phenomenon governed by viscous dissipation is captured by the volume diffusion model in

the right corner (Figure 5.3a). For such high Knudsen number John *et al* performed similar case using DSMC and showed a heat transfer identical as the one presented in Figure 5.3c [104]. Their results are consistent with those performed from our DSMC code and the volume diffusion model.

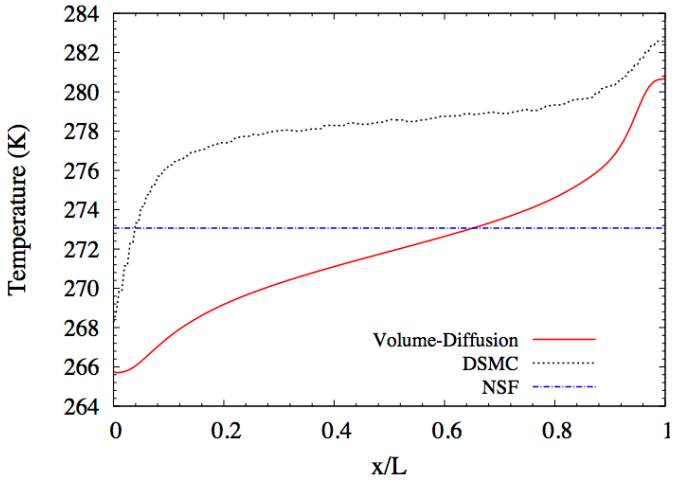

Figure 5-4 Variation of gas temperature near the top lid (y/L = 0.9) of the cavity for DSMC, NSF and Bi-Velocity at Kn = 10

Figure 5.4 shows the temperature distribution near the top moving lid for the volume diffusion model, DSMC and NSF. Temperature obtained by NSF is constant. This means that NSF does not reveal any disequilibrium for that configuration. This model is therefore inadequate for such a high Knudsen number as expected. Volume diffusion model and DSMC show non-uniform temperature distribution as they capture the non-equilibrium imposed by the moving lid. Volume diffusion model predicts lower temperature near the left wall compared to DSMC. DSMC shows a "plateau" in the middle of the cavity while volume diffusion model shows a gradually increasing temperature from left to right. The maximum difference between the two models occurs in the middle of the cavity and is 2.94%.

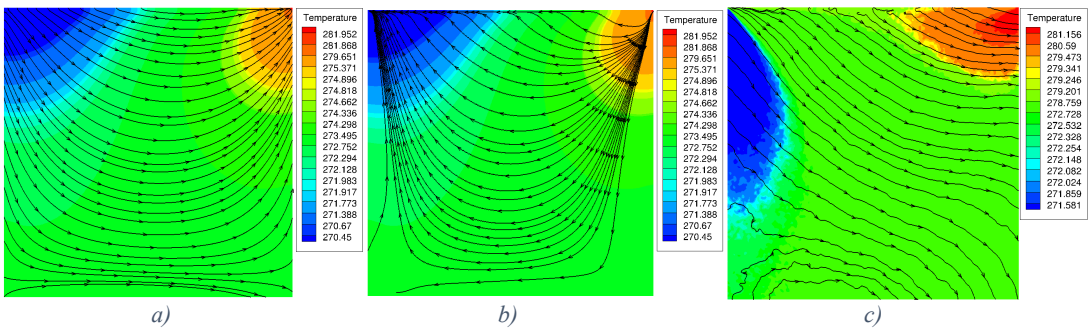

Figure 5-5 Energetic heat flux a) and entropic heat flux b) lines overlaid on the temperature contour for Kn = 1 in comparison with DSMC heatflux c)

In the mid-transition regime (Figure 5.5), for Kn = 1, entropic heat flux again follows the Second Law, i.e., a heat transfer from hot-to-cold. The energetic heat flux predicts cold-to-hot heat transfer in agreement with DSMC prediction. This agreement between DSMC heat flux and volume diffusion energetic heat flux can be understood. In the DSMC particle based method heat flux is defined via particle kinetic energy. This particle kinetic energy is associated with indeed the energy equation and the energetic heat flux within the volume based continuum approach. The volume diffusion model predicts better the cold-to-hot heat transfer phenomenon compared to DSMC. General agreement is observed for the temperature profiles for the two methods. The same maximum temperature is predicted.

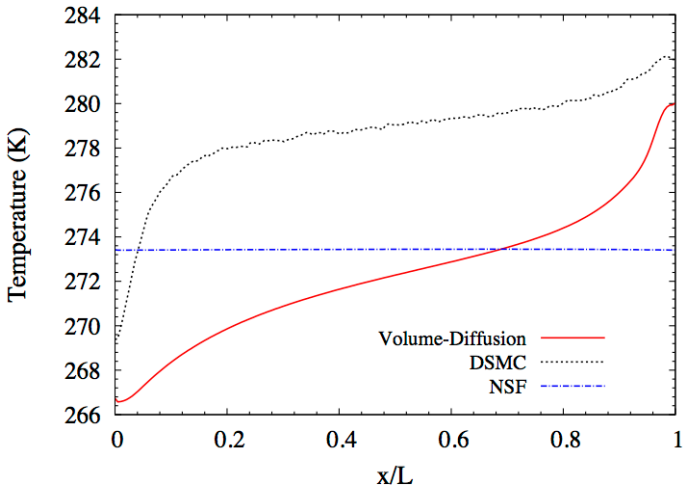

Figure 5-6 Variation of gas temperature near the top lid (y/L = 0.9) of the cavity for DSMC, NSF and Bi-Velocity at Kn = 1

For Kn = 1 (Figure 5.6), NSF is still inadequate in capturing the non-equilibrium imposed by the moving lid as it predicts a constant gas temperature. DSMC and volume diffusion again resolve the non-equilibrium structures with some differences in trend. The maximum relative difference between temperature values from the two methods is about 2.2%. In Figures 5.4 and 5.6 the temperature decreases at the left wall and increases at the right wall for DSMC and volume diffusion.

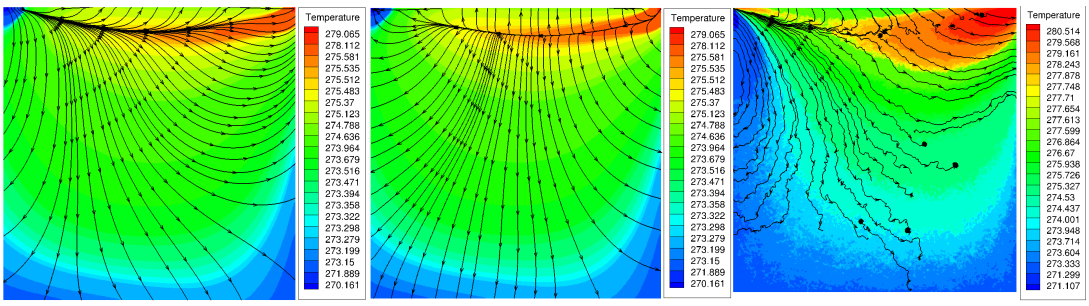

a) *b)* *c)*

Figure 5-7 Energetic heat flux a) and entropic heat flux b) lines overlaid on the temperature contour for Kn = 0.1 in comparison with DSMC heatflux c)

As the Knudsen number decreases, the energetic heat flux contour from the volume diffusion model become more similar to DSMC prediction (Figures 5.7a and 5.7c). Furthermore, entropic heat flux in Figure 5.7b is still consistent with the second law. Both methods predict a low temperature for the lower wall. Agreement is found for the minimum and maximum temperature. Mohammadzadeh *et al* performed a DSMC study for a lid-driven cavity with up to Kn = 0.1 m The heat transfer predicted from their DSMC model is matching volume diffusion results (Fig. 5.7a); see Ref [12].

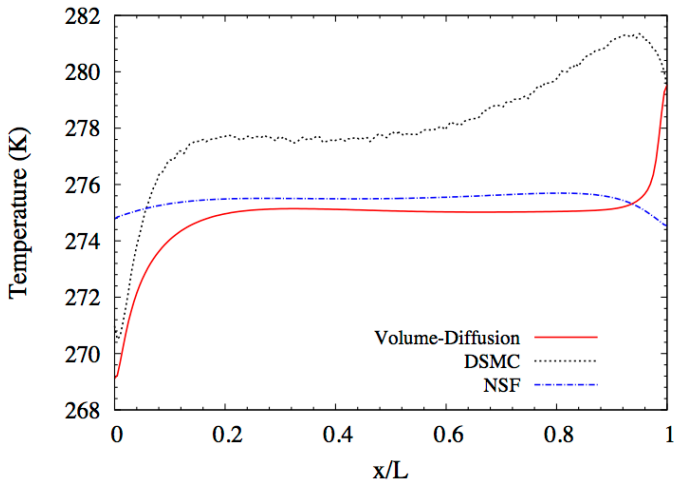

Figure 5-8 Variation of gas temperature near the top lid (y/L = 0.9) of the cavity for DSMC, NSF and Bi-Velocity at Kn = 1

Comparison of the three models at Kn = 0.1 is shown in Figure 8. NSF starts to exhibit some non-equilibrium effects at walls. Volume diffusion predicts thermal boundary layer at both walls characteristic of Knudsen layers connected with a nearly uniform temperature in the middle of the cavity, which is close to NSF value. Overall, NSF prediction is still different from the predictions by DSMC and volume diffusion. Agreement is found for the minimum and maximum temperature at the walls between DSMC and volume diffusion. Furthermore, the trends of the two methods are consistent and both methods show that left and right walls are in non-equilibrium state. The average relative difference between temperature values for the DSMC and the volume diffusion is about 2.4%. DSMC shows a temperature shoot near the right wall before converging to the wall temperature. Volume diffusion model has a rather more symmetrical profile.

Figure 5.9a shows the u-velocity along a vertical line crossing the center of cavity between the three velocities normalized with the lid velocity ($\mathbf{U_w}$ = 100 m/s): the mass velocity $\boldsymbol{U_m}$ and the volume velocity $\boldsymbol{U_v}$ within the volume diffusion model and the DSMC mass velocity $\boldsymbol{U_{DSMC}}$. The u-component of the mass velocity $\boldsymbol{U_m}$ is zero at Kn = 10. The v-velocity component of the three velocities is shown in Figure 8.b along a horizontal line crossing the center of the cavity. DSMC velocity profile lies between the volume velocity

and the mass velocity. The continuum mass velocity is however zero in both Figure 5.9a and b. The v-velocity from DSMC shows a v-velocity-slip near walls. The volume velocity is also non-zero at walls. Although the trend for these two velocities ($\boldsymbol{U_v}$ and $\boldsymbol{U_{DSMC}}$) is the same for that Knudsen number. The deviation in the v-velocity between the DSMC and the volume diffusion is observed in the Knudsen layer. At such high Knudsen number Knudsen layers cover most of the flow domain.

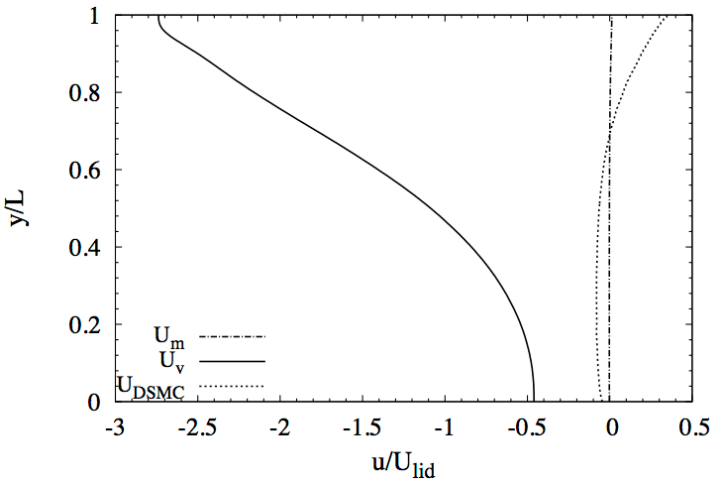

a)

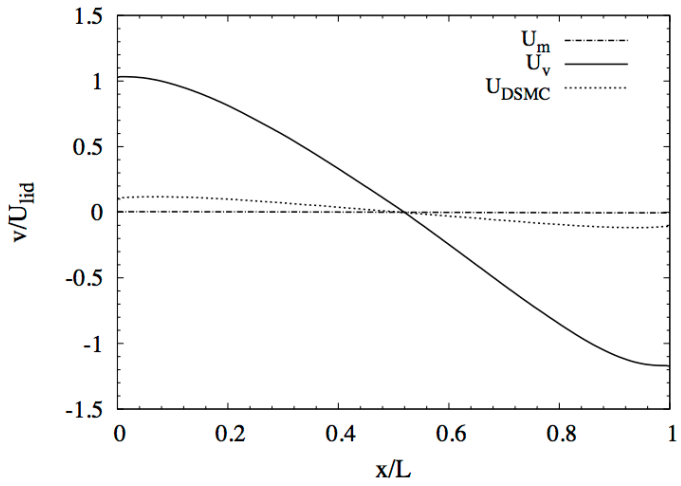

b)

Figure 5-9 Computed a) u-velocity profile plotted along a vertical line and b) v-velocity profile plotted along a horizontal line, crossing the center of the cavity at U_{DSMC}, U_m and U_v for Kn = 10

The normalized velocities components at Kn = 1 are shown in Figure 5.10. The u-velocity profiles are different between the three. The v-components are in Figure 5.10b. All velocities predict similar trend. However, $\boldsymbol{U_v}$ is the closest to $\boldsymbol{U_{DSMC}}$.

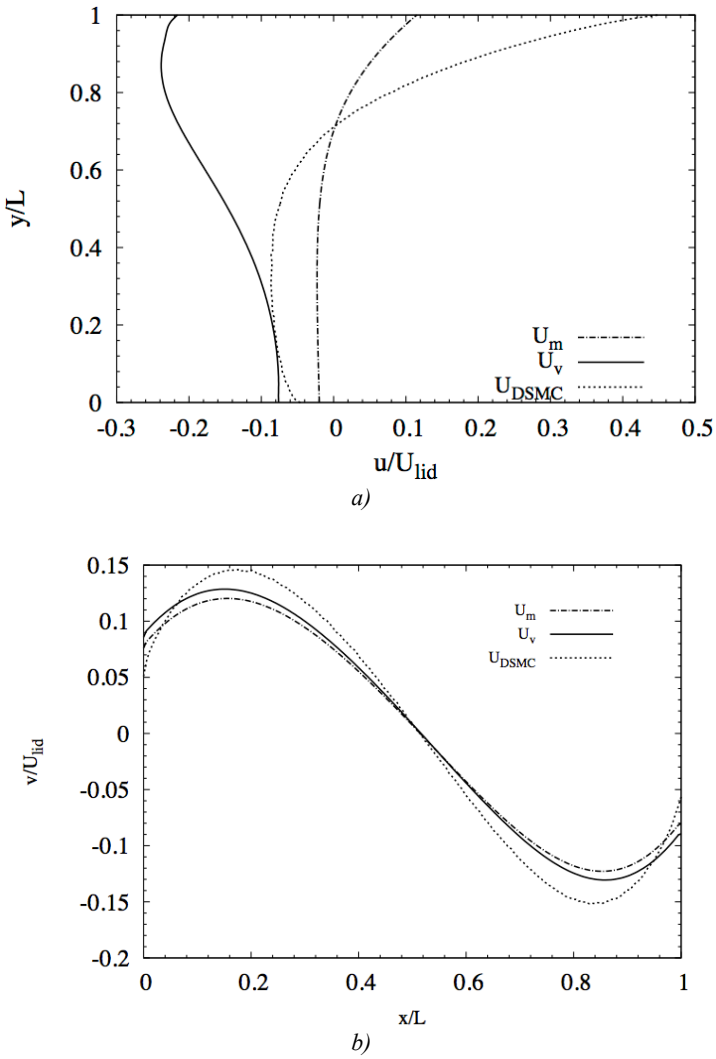

Figure 5-10 Computed a) u-velocity profile plotted along a vertical line and b) v-velocity profile plotted along a horizontal line, crossing the center of the cavity at U_{DSMC}, U_m and U_v for Kn = 1

Figure 5.11 presents the velocities profiles for Kn = 0.1 where we observed agreement between the different velocity on the u-component and v-component as the Knudsen number is decreased. It can be observed that all velocities have nearly the same value for u-velocity-slip. DSMC predicts though slightly lower slip than volume diffusion in Figure 5.11a. The v-velocity component in Figure 5.11b shows that there is agreement between the three methods. However, volume diffusion predicts a slightly lower slip closer to DSMC

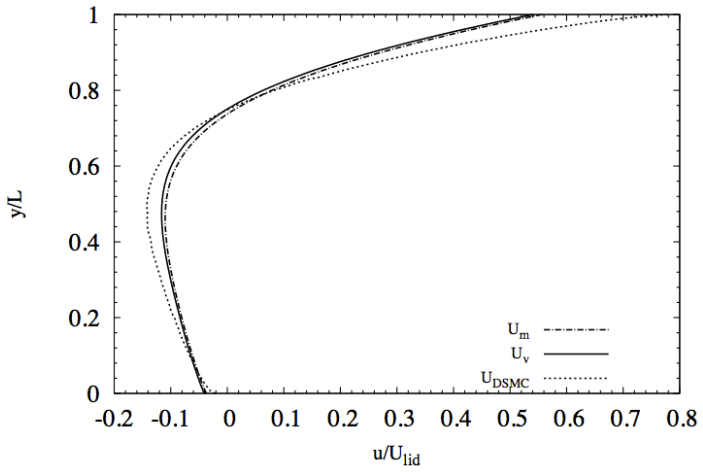

a)

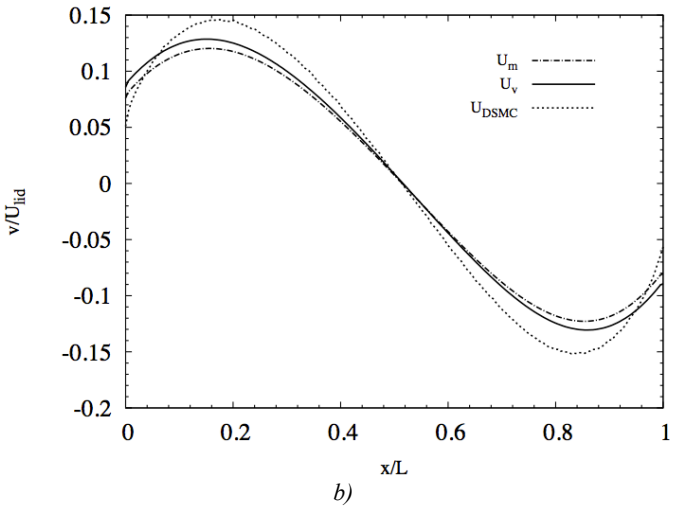

b)

Figure 5-11 Computed a) u-velocity profile plotted along a vertical line and b) v-velocity profile plotted along a horizontal line, crossing the center of the cavity at $U_{DSMC,}$ U_m and U_v for Kn = 0.1

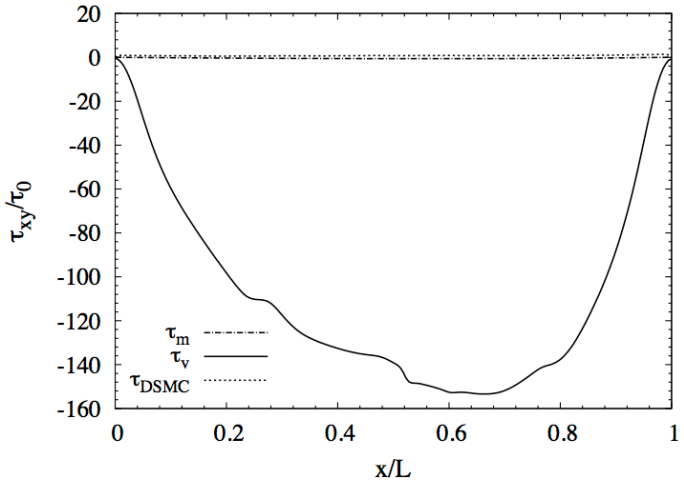

a)

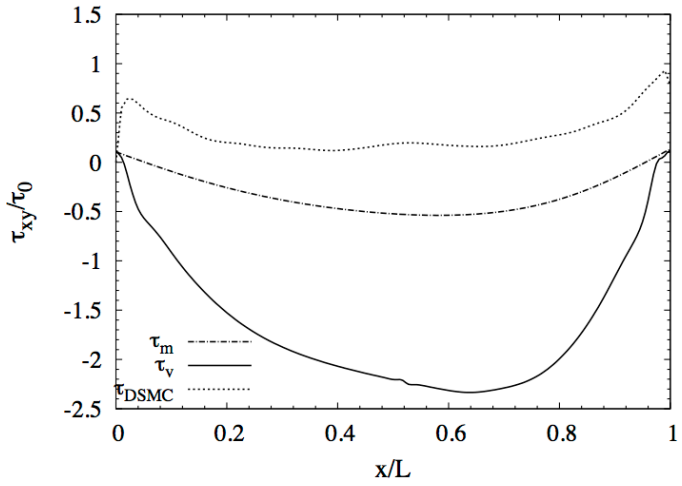

b)

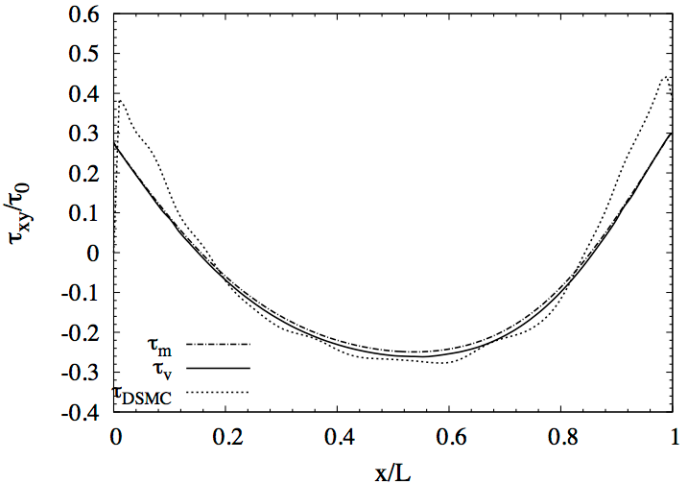

c)

Figure 5-12 Shear stress profile along the horizontal line of the cavity for a) Kn = 10 b) Kn = 1 and c) Kn = 0.1

Figure 5.12 shows the shear stress profiles along the horizontal line of the cavity. The shear stress has been normalized with respect to $\boldsymbol{\tau_0}$ where $\boldsymbol{\tau_0} = 0.5\rho \boldsymbol{U_w^2}$. The variation of the shear stress for the three different Knudsen numbers is investigated and compared between the shear stress from DSMC ($\boldsymbol{\tau_{DSMC}}$), NSF ($\boldsymbol{\tau_m}$) and volume diffusion ($\boldsymbol{\tau_v}$). For all the methods, the strength of the stress decreases as the Knudsen number decreases. $\boldsymbol{\tau_{DSMC}}$ and $\boldsymbol{\tau_m}$shear stress reduces significantly for large Kn and tend to zero for Kn > 10. For the large Knudsen numbers (Figure 5.11.a) $\boldsymbol{\tau_v}$ is evidently high in comparison to others.

Knudsen layer is usually defined as a kinetic boundary layer in rarefied gas flows near surfaces with thickness in the order of magnitude of the mean free path where the behavior of the gas cannot be captured in a standard continuum Navier-Stokes description. Gusarov

and Smurov Eq. 5.1 performed a numerical analysis of the Knudsen layer [109]. They concluded that the thickness of the Knudsen layer, $z_{0.1}$, can be estimated by the position where the heat flow decreases by a factor of ten from its wall value. Using this criterion Figure 5.13 depicts the normalized Knudsen layer thickness (with the mean free path) as a function of Knudsen number between the three different methods investigated:

$$q_z(z_{0.1}) = 0.1 q_z\,(0) \tag{5.1}$$

where, $q_z\,(0)$ is the heat flux at the wall ($x = 0$). It can be observed that for the low Knudsen number (Kn = 0.1) the predicted Knudsen layer thickness appears the same between models. In the transition regime (Kn = 1) the Knudsen layer becomes thicker for both DSMC and Volume Diffusion. These two methods prediction for the Knudsen layer expands toward the free molecular regime flow, Kn = 10. Overall, Volume Diffusion is in agreement with DSMC for the Knudsen layer thickness.

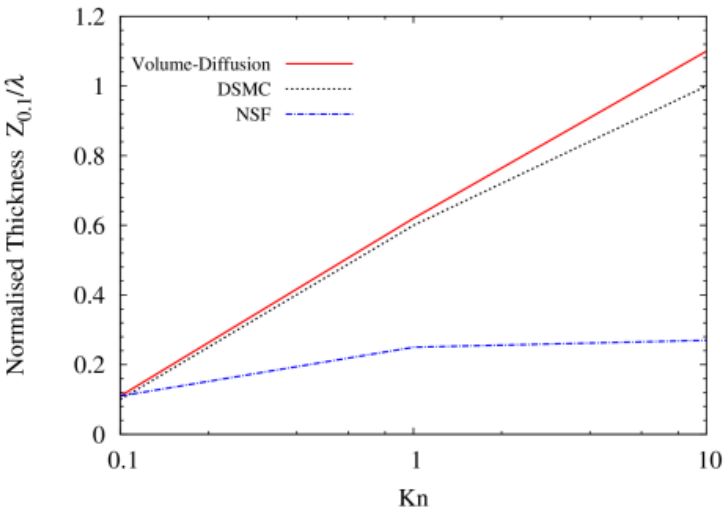

Figure 5-13 Knudsen Layer Thickness across different Knudsen numbers

We have presented a comparison between the newly developed volume-diffusion (or bi-velocity) model with Navier-Stokes and DSMC using our in-house CFD codes. However, in a complete validation we have to compare it with other results reported in the literature for the same problem. Here we used the work done by John et al using DSMC for a lid-driven cavity with slightly different Knudsen number and lid velocity as presented in table 5.2 [108] . They performed an investigation of heat transfer in a lid-driven under non-equilibrium conditions for a wide range of Knudsen number using DSMC. In order to check the validity of our model we compare the volume diffusion model with their simulations

for the highest Knudsen number (Kn = 8) in their work. Table 5.2 shows the case properties that were used in their simulations.

Table 5-2 John et al case properties

Gas	Temperature (K)	Initial Velocity (m/s)	Kn	Wall Boundaries
Argon	273	50	8	*Fully Diffuse*

In Fig.5.14 we compare normalized temperature profile along horizontal line crossing the center of the cavity. Both methods show that the left and right wall is under non-equilibrium conditions. It can be observed that the two methods are in good agreement. In addition, it can be observed that for the right wall the two methods are in excellent agreement. However, from the center of the cavity and to the left wall of the cavity the difference as for the temperature distribution increases slightly.

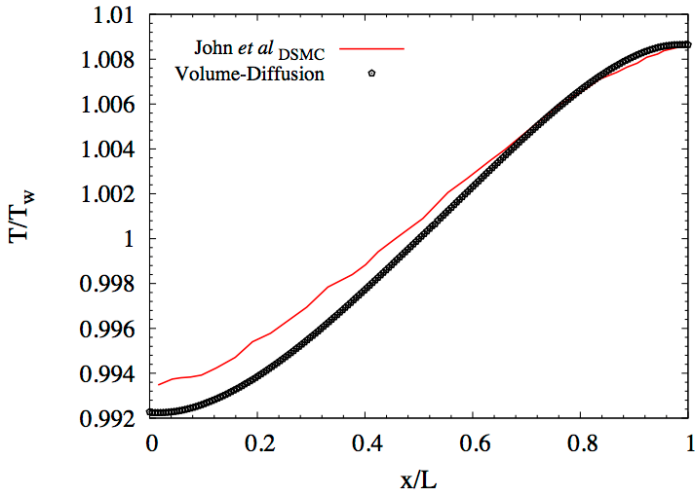

Figure 5-14 Comparison of the normalized temperature along the center of the cavity

5.2.2. Mixed-Convection Problem

Lid-driven cavity flow problem is often used to benchmark new continuum fluid models as several investigations are carried out using the configuration [110, 111].Several heat transfer mechanics, namely, natural convection, forced-convection and mixed-convection are all investigated using hydrodynamic models as understanding thermal behaviours of a lid-driven cavity fuels applications in electronic cooling, manufacturing processes and others. For example, Iwatsu and Hyun provided a numerical study of three dimensional flows in a cubical container with stable vertical temperature stratification [112]. Ghasemi and Aminossadati presented the numerical study of mixed-convection in a lid-driven filled

with water and nanoparticles [113] . Cheng and Liu investigated effects of the cavity inclination on mixed convection heat transfer [114].

In the present study, we compare volume-diffusion with standard Navier-Stokes. Sketch of the problem under investigation and boundary conditions are shown in Figure 5.15. It is a two-dimensional square cavity of length $W = 50\mu m$ and aspect ratio of one. The cavity is filled with compressible monoatomic argon, *Ar,* with negligible gravity force. The horizontal walls are adiabatic with the top moving at velocity $\boldsymbol{U_w}$ = 100 m/s generating a forced convection. The left vertical wall is kept at the lower temperature (T_c = 273K) and the right vertical wall at the higher temperature (T_H = 283K).

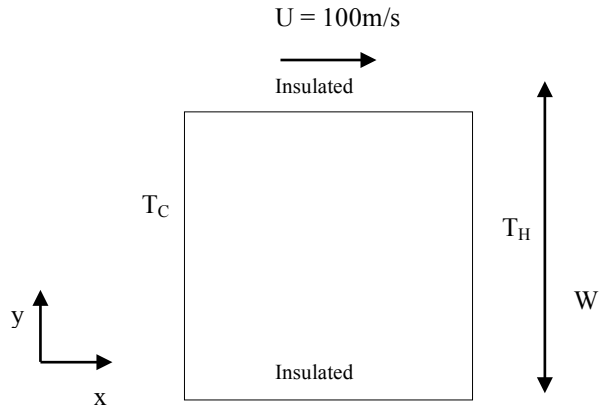

Figure 5:15 Mixed-Convection Problem configuration

The viscosity for the simulations was μ = 1,69 x 10^{-5} Pa s. Table 5.3 presents the flow characteristic numbers including the Reynold number (Re), Lewis number (Le) and Peclet number across the simulation range. Reynolds number is a dimensionless number and can be calculated by, Re = ρUD/μ, where D is the diameter and μ fluid viscosity. Lewis number is dimensionless number and is defined as the ratio of thermal to species diffusivity [115]. Peclet number is dimensionless number as well and it is the ratio of thermal energy convected to the fluid to the thermal energy conducted within the fluid. Mass transfer peclet number can be calculated as, Pe_L = WU/D^*, where D^* is the mass diffusion coefficient [116].

Table 5-3 Flow characteristic numbers across the simulation range

Kn	λ(m)	W(m)	Re	Lewis Number	Peclet Number	Mass Transfer Peclet number
0.001	5.0E-08	5.0E-05	296	7	195	1346
0.005	2.5E-07	5.0E-05	290	7	191	1319
0.01	5.0E-07	5.0E-05	258	7	170	1172
0.5	2.5E-05	5.0E-05	66	7	44	302
1	5.0E-05	5.0E-05	40	7	26	182
10	5.0E-04	5.0E-05	4	7	3	20

Figure 5.16 shows temperature and pressure distributions near the top wall. The top right wall region is the most in non-equilibrium state. At Kn = 0.001 NSF and volume diffusion methods predict the same temperature distribution with the lower temperature on the left wall and the higher on the right. From Kn = 0.005 differences in predictions by the two methods start to appear first in the top right-hand wall region. The difference between the two methods occurs around the peak temperature and becomes noticeable at Kn = 0.01 where though the overall temperature trend remains similar. As we increase the Knudsen number to 1, NSF temperature profile becomes constant; i.e., NSF no longer captures any temperature variation caused by the movement of the top lid. NSF with slip and jump conditions fail completely to capture the disequilibrium in the flow field imposed by the moving lid. Volume diffusion model, however, shows a non-uniform temperature distribution with boundary layers near both walls typical of Knudsen layers. We also observed temperature jumps at both walls. The pressure profiles are normalized with P_0 = 97500Pa and are shown in Figure 5.16b. The pressure distribution is the same at all Knudsen numbers between the two methods. This means that, with the mixed convection configuration investigated here, no significant correction to the momentum equation is observed. Temperature and heat transfer processes are the most affected by the volume diffusion correction in that configuration. Meanwhile, the equality observed in the temperature profile for Knudsen number less than 0.001 with a deviation above that value confirms that the volume diffusion correction to NSF model is a way of distinguishing between the different flow regimes.

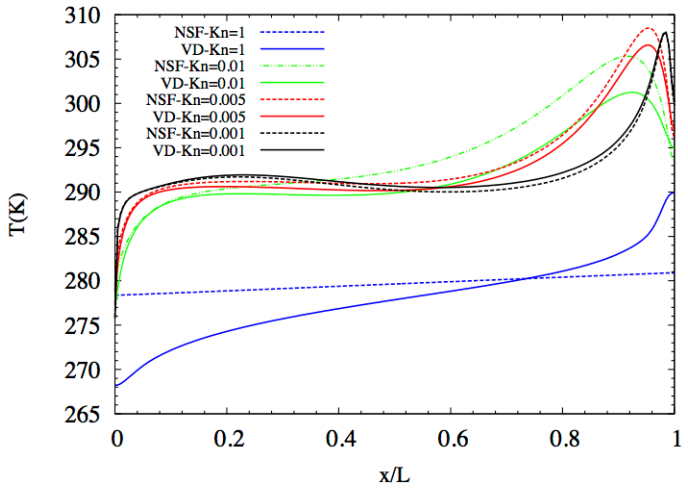

a)

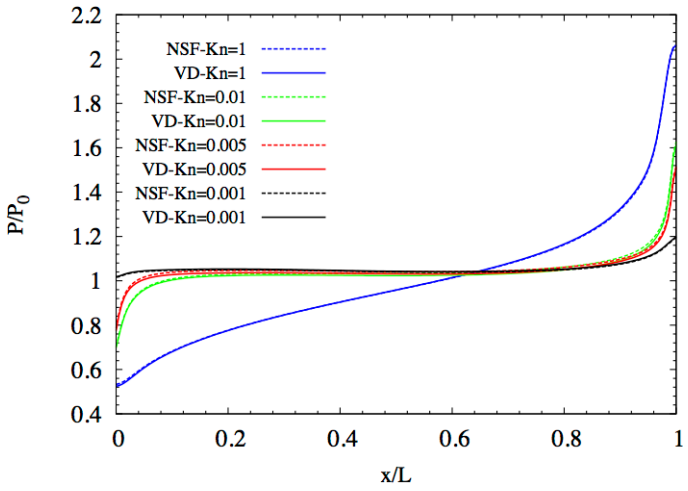

b)

Figure 5-16 Comparison of the temperature a) and pressure b) profiles along the top wall

Figure 5.17 shows the variation of maximum heat fluxes as a function of Knudsen number in the domain. Highest maximum heat flux is predicted by volume diffusion model. Energetic heat flux is always higher than the entropic heat flux and both are well above heat flux predicted by NSF.

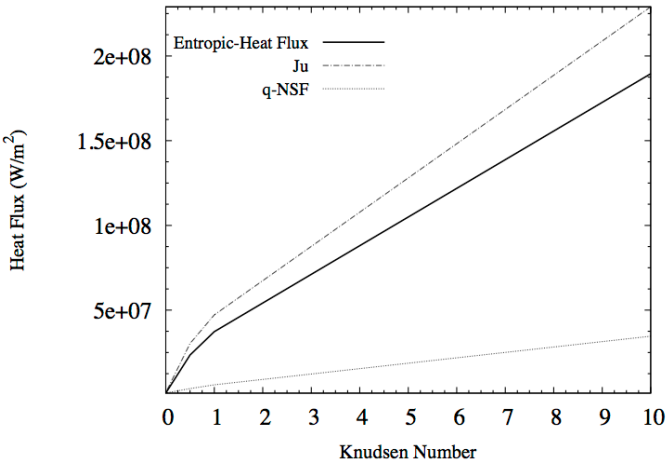

Figure 5-17 Variation of maximum heat flux with respect to Knudsen number

Figure 5.18 depict the temperature field at Kn = 0.001 along with the heat flux. Energetic heat flux and entropic heat flux for the volume diffusion model, and classical heat flux from the Navier-Stokes-Fourier are shown. We observe at that Knudsen number the same temperature contours for the three heat fluxes. The left wall is the cooling wall according to the set boundary conditions. The top right corner of the cavity has an increase in temperature due to viscous dissipation and strong non-equilibrium effects. The heat transfer is from hot-to-cold in the entire cavity.

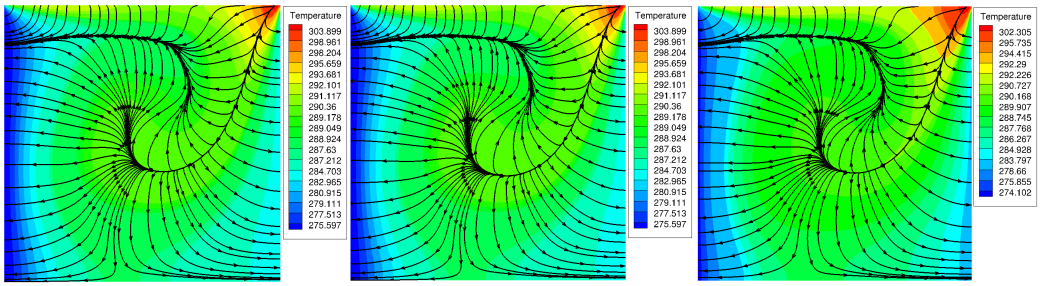

a) *b)* *c)*

Figure 5-18 Temperature distribution and heat fluxes at Kn = 0.001 for the a) energetic heat flux(J_u), b) entropic heat flux(q_{ve}) and c) heat flux conventional NSF(q_{NSF})

Contour plots for Knudsen number corresponding to the transition regime (Kn = 0.5) are in Figure 5.19. Lowest and highest temperatures as predicted by NSF and volume diffusion now differ by about 8 degrees. The temperature drop across the cavity obtained by volume diffusion is higher than that of NSF. The volume diffusion model (Fig 5.19a,b) shows the two top corners in non-equilibrium state. The lowest temperature occurs in the top left due to expansion cooling. Though, gas molecules leaving that region transport out, generally, higher translational kinetic energy. This is the indication of the direction of the energetic heat flux in Figure 5.19a in that corner. It is a demonstration of flow phenomena in which temperature is not systematically synonymous with the gas molecule translational kinetic

energy. Overall, heat transfers in Figure 5.19a are the results of combined mass diffusion and forced convection as effects of the disturbing moving lid can be seen along the top wall. Entropic heat flux in Figure 5.19b shows a flow from the top right corner, i.e. the highest temperature and non-equilibrium region, to cold areas. This is an explicit expression of the second law of thermodynamics corresponding to the configuration. From Figure 5.19a the higher temperature observed in the top right corner appears as a result of compression of gas molecules coming from the top and right walls at lower translational kinetic energy. Temperature variation predicted by the NSF is in Figure 5.19c. It simply depicts heat diffusion from higher kinetic energy region on the right, to the lower kinetic energy region on the left. Effects of the moving lid are almost non-existent in the NSF temperature contours. In contrast, in Figure 5.19a three main phenomena accompanying the energetic heat transfer process in the volume diffusion model may be stated: expansion cooling that takes place in the top left corner, compression in the right corner and the usual heat conduction transfer process.

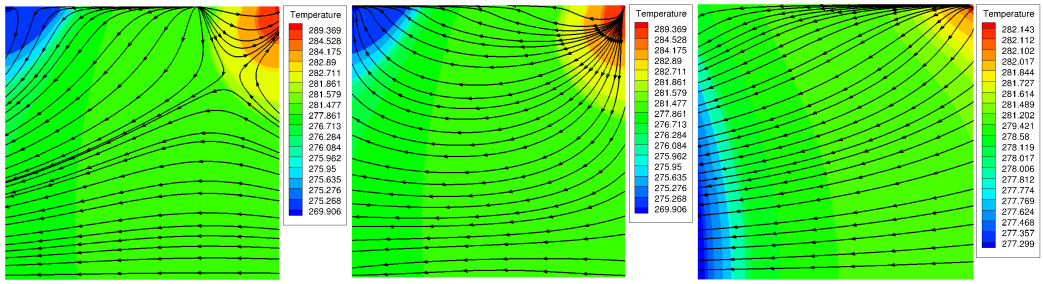

Figure 5-19 Temperature distribution and heat fluxes at Kn = 0.5 for the a) energetic heat flux (J_u), b) entropic heat flux(q_{ve}) and c) heat flux conventional NSF(q_{NSF})

Temperature contours in the high transition regime is represented by Figure 5.20 at Kn=10. Phenomena observed in the early transition regime are now fully developed. NSF displays a constant temperature across the cavity, i.e. none of the disequilibrium conditions is captured by NSF. Energetic heat flux in Figure 5.20a from the volume diffusion model shows again non-equilibrium state. An unconventional energetic heat transfer from cold-to-hot in the upper left corner as well as in the right corner occurs. The moving top lid induces these non-equilibrium effects. In Figure 5.20b, entropy flows from top right corner into the top left corner, which is again consistent with the second law.

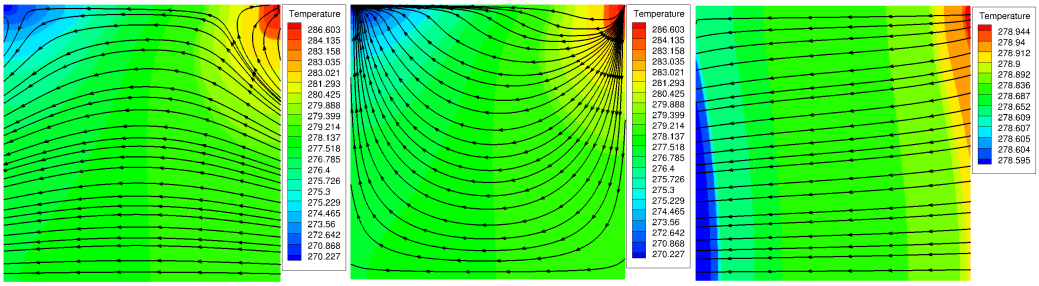

a) *b)* *c)*

Figure 5-20 Temperature distribution and heat fluxes at Kn = 10 for the a) energetic heat flux (J_u), b) entropic heat flux(q_{ve}) and c) heat flux conventional NSF(q_{NSF})

Generally, volume diffusion process in the present forced convection configuration appears physically as a counter-diffusion process. That is, a process where molecules with lower translational kinetic energy diffuse toward higher translational energy region. The movement of gas molecules from the higher translational kinetic energy toward the lower regions is driven by advection by the moving lid (viz. Figure 5.7c). This is depicted in the variation of the mass transfer Peclet number in table 3; it varies from 1346 at Kn=0.001 to 20 at Kn=10.

In order to further investigate implications of the introduction of the two different flow velocities, the mass and volume velocity profiles are plotted along centerlines of the cavity for three different Knudsen numbers in Figures 5.21 and 5.22. For the low Knudsen number the two velocities profiles are identical. The clear difference is at Kn > 0.5. The volume velocity v-component in Figure 5.21b predicts nearly double the slip in the mass velocity. In fact, as Knudsen number increases the v-component of $\boldsymbol{U_m}$ decreases and totally vanishes in the domain at Kn=10. The volume velocity becomes dominant flow velocity in the domain in the higher Knudsen number regime as the mass velocity vanishes. This is consistent with the pressure profile in Figure 5.16b. For Knudsen number 10 where the mass velocity totally vanishes, the advection of molecules into the left corner and out of the right due the moving lid are represented by the positive v-component of the volume velocity on the left wall and negative component at the right Figure 5.21c.

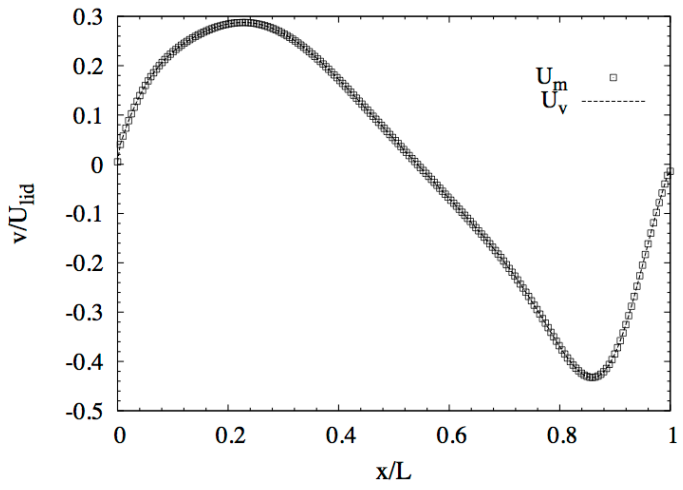

a)

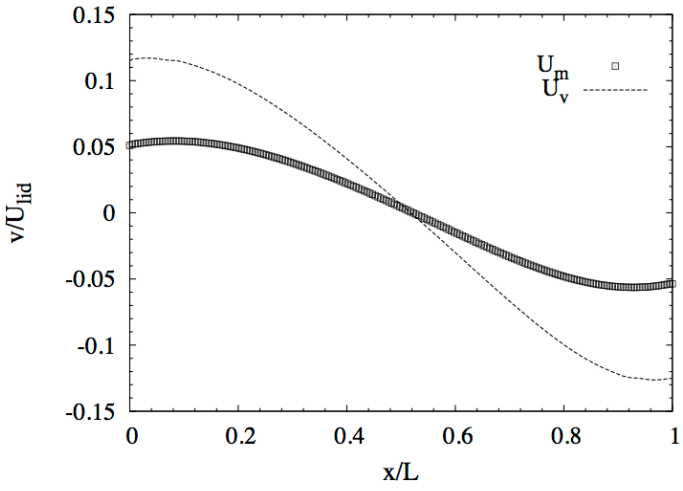

b)

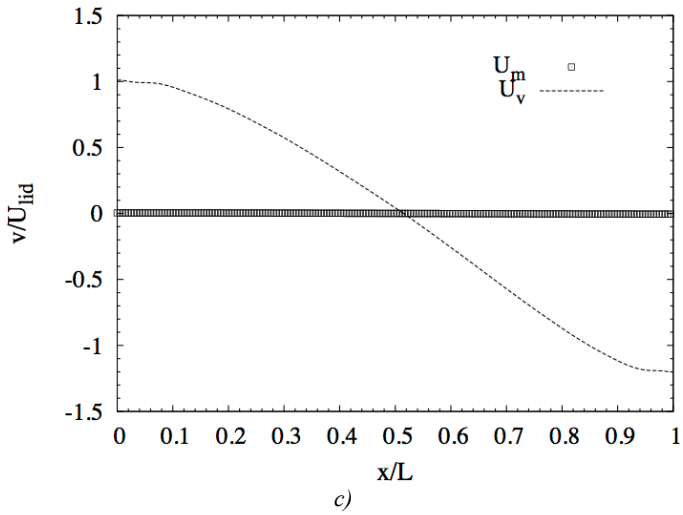

c)

Figure 5-21 Computed mass and volume v-velocity component profile plotted along a horizontal line, crossing the center of the cavity for a) Kn = 0.001, b) Kn = 0.5 and c) Kn = 10

The u-velocity profile along a vertical line crossing the cavity center is shown in Figure 5.22. At Kn=0.001 mass and volume velocities have the same profile and no clear slip is observed at walls. For Kn = 0.5 both methods have similar trend but differences exist in the amount of slip at walls. There is a higher u-velocity slip for the volume velocity compared to the amount of slip in the mass velocity. For Kn = 10 in Figure 5.21c, the normalized mass velocity is zero with no slip effects. The volume velocity shows now a reverse profile. In addition, the u-velocity slip in the volume velocity becomes large. As for the v-velocity component the volume velocity dominates the domain as the Knudsen number increases.

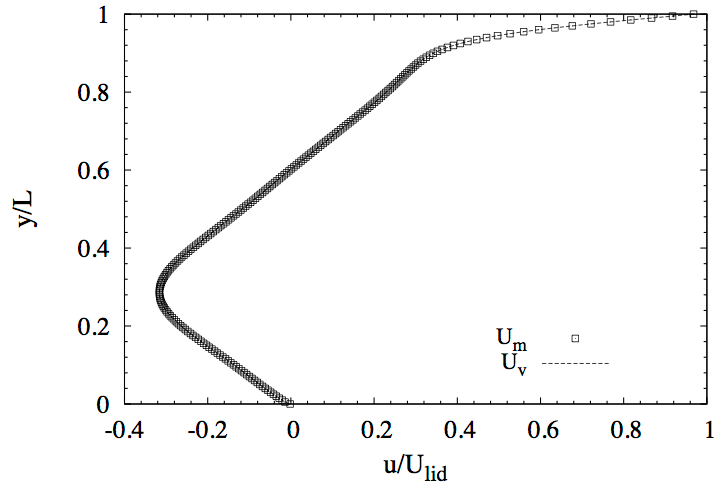

a)

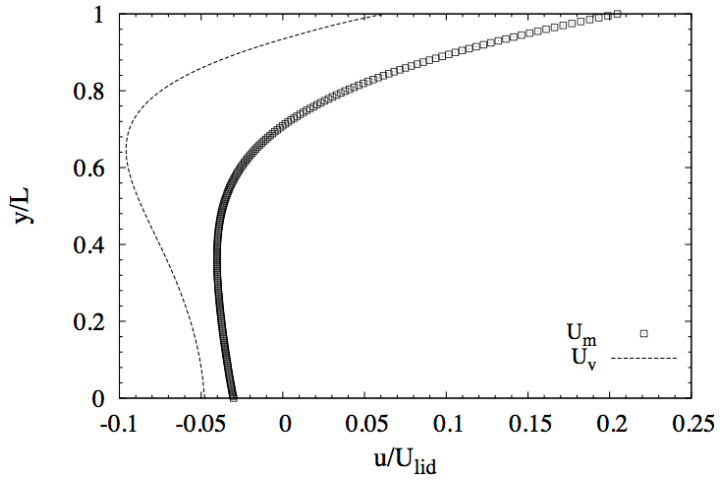

b)

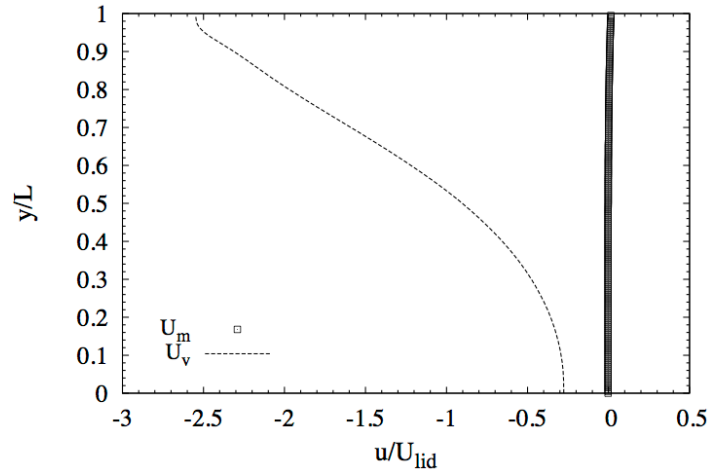

c)

Figure 5-22 Computed mass and volume v-velocity component profile plotted along a vertical line, crossing the center of the cavity for a) Kn = 0.001, b) Kn = 0.5 and c) Kn = 10

5.3. Micro-channel Poiseuille flow

The micro-channel is the only case that available experimental data will allow us to compare numerical results from the two CFD codes. The Bi-velocity and Korteweg along with NSF numerical results will be compared against the experimental data and analytical solution from Dadzie and Brenner [68]. The dimensions of the channel were accurately set to the original one from Ewart *et al* [94]. The purpose of their experiments was to complete the database of mass flow rate measurements, obtained for a gas flow in a single microchannel, ranging from the hydrodynamics regime to the near free molecular regime. Figure 23 illustrates the experimental and numerical set-up conditions for the microchannel.

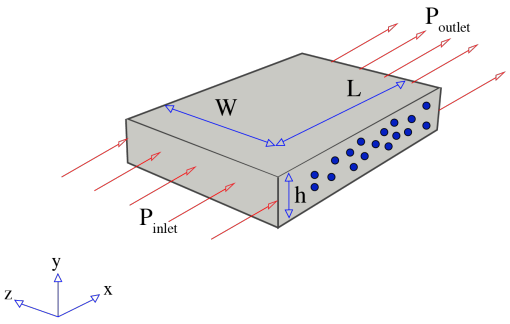

Figure 5-23 Schematic of the flow through a microchannel. The flow direction is represented by the red arrows for P_{inlet} and P_{outlet}. The blue dots show the gas molecules. Where L,W >> h

The average pressure in the experiments ranges from 67000 to 30 Pa. The experimental method that was used to measure the mass flow rate through the microchannel involves the use of two large constant volume tanks that are much larger than the volume of the microchannel. More details of the experimental procedure can be found in Ewart *et al* [94]. Their data (mass flow rate results) are used as a benchmark for our simulations. Fluid properties and physical coefficients that are used in the simulations are listed in table 5.4. The mean Knudsen number is defined:

$$Kn_{mean} = k_\lambda \frac{\mu}{\frac{P_{inlet} + P_{outlet}}{2}} \sqrt{2RT} \tag{5.2}$$

It can be noted that the length (L) and the width (W) of the micro-channel are extensively greater than its height.

Table 5-4 Fluid Properties and microchannel physical coefficients

W(m)	L(m)	h(m)	Pr	μ(Pa s)	R(J/kg k)	k_λ
4.92×10^{-4}	9.39×10^{-3}	9.38×10^{-6}	0.67	1.97513×10^{-5}	2076.942	$\sqrt{\pi/2}$

The extended boundary conditions are implemented in both methods for the full range of Knudsen number. In order to compare our simulations with experimental data and previous studies the figures are plotted in the nondimensional mass flow rate, G_m versus the mean Knudsen number. The dimensionless mass flow rate, G_m can be calculated by:

$$G_m = \dot{M} \left[\frac{wh^2}{L\sqrt{2RT}} \left(p_{inlet} - p_{outlet} \right] \right]^{-1} \tag{5.3}$$

The mass flow rate, $\dot{M}$ through the microchannel is given by:

$$\dot{M} = w \int_0^h \rho U_m dy \tag{5.4}$$

While in previous studies [68, 117] the mass flow rate was expressed as an analytical solution in the present study we focus on the calculation of the mass flow rate directly from the numerical methods based on the Korteweg and bi-velocity models. The results from simulations that are based on hydrodynamics models for mass flow rate in microchannels have not been reported earlier.

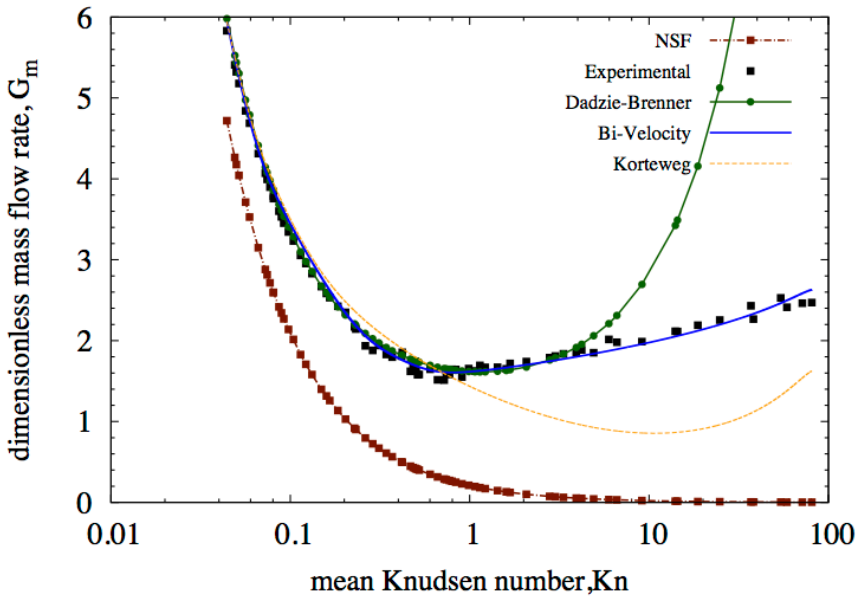

Figure 5-24 Comparison of the mass flow rate using Bi-Velocity and Korteweg against Navier-Stokes, Dadzie-Brenner and experimental data

In Figure 5.24 we can observe the comparison of the dimensionless mass flow rates from experimental data with Korteweg. Bi-velocity and standard NSF models. It is obvious that the standard Navier-Stokes fails in comparison with the experimental data in the whole range of Knudsen number that is been investigated by the experiment. Furthermore, it confirms that as the Knudsen number increases the dimensionless mass flow rate decreases. For the slip regime ($0.01 < Kn_{mean} < 0.1$) Bi-velocity, Korteweg and Dadzie-Brenner are in good agreement with the experimental data. For all methods, the normalized mass flow rate decreases as Knudsen number increases in this regime. In the early transition regime ($0.1 < Kn_{mean} < 1$) Bi-velocity and Dadzie-Brenner analytical solutions agree well with the experimental dimensionless mass flow rate. The Korteweg are close to experimental data but in not so good agreement. We can observe that the Korteweg mass flow rate diverges

from the experimental data for Kn = 0.2 - 0.6, while it has better agreement for Kn = 0.8 – 1. For the transition regime ($0.1 < Kn_{mean} < 10$) the only method that is still in a very good agreement with the experimental data is the bi-velocity model. The Dadzie-Brenner solutions which are also based on the bi-velocity hydrodynamics agree well with the experimental data for $Kn_{mean} < 5$. However, it should be noted that these results are obtained using analytical solutions and different boundary conditions. The Korteweg model agreement starts to vanish for a Knudsen number higher than the unity. For the free molecular regime ($10 < Kn_{mean} < 100$) the bi-velocity is in excellent agreement with the experiment. At this regime, the Dadzie-Brenner theoretical work over-predicts the dimensionless mass flow rate. Interestingly the Korteweg model while it decreases the mass flow rate for $Kn_{mean} < 10$, it shows an increase for $Kn_{mean} > 10$ following the experimental data and Bi-velocity trend line. This may be attributed to the contribution of the additional shear stress tensor components as it was expressed previously.

In 1909 Knudsen studied gas flows through tubes in the transition and free molecular regimes. From these results, the normalized volumetric flow rate showed a minimum at a Knudsen number near unity [118]: The *Knudsen paradox*. The present numerical solution by the Bi-velocity model and Dadzie-Brenner solution as shown in Figure 5.24 both capture the *Knudsen paradox*. This *Knudsen paradox* is usually difficult to capture using a Navier-Stokes with slip conditions [119].

In general, Figure 5.24 reveals that the two continuum hydrodynamic models which involved density gradient expressions in the shear stress constitutive equations are better in predicting this micro channel gas flow. This corroborates recent observations by Gorban and Karlin [73].

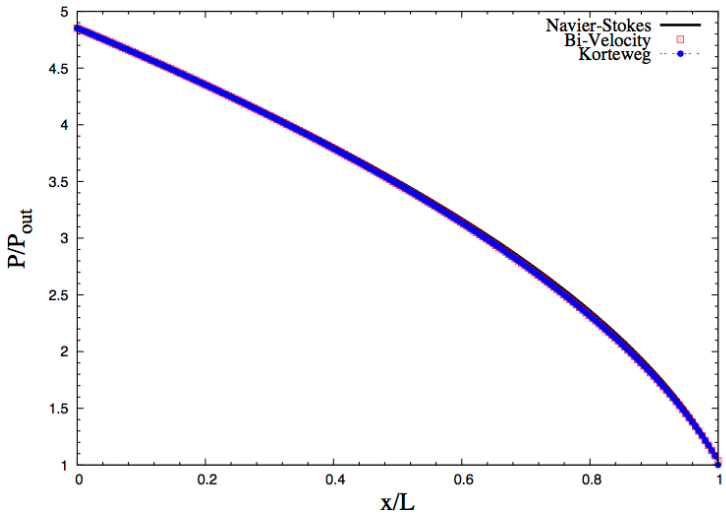

a)

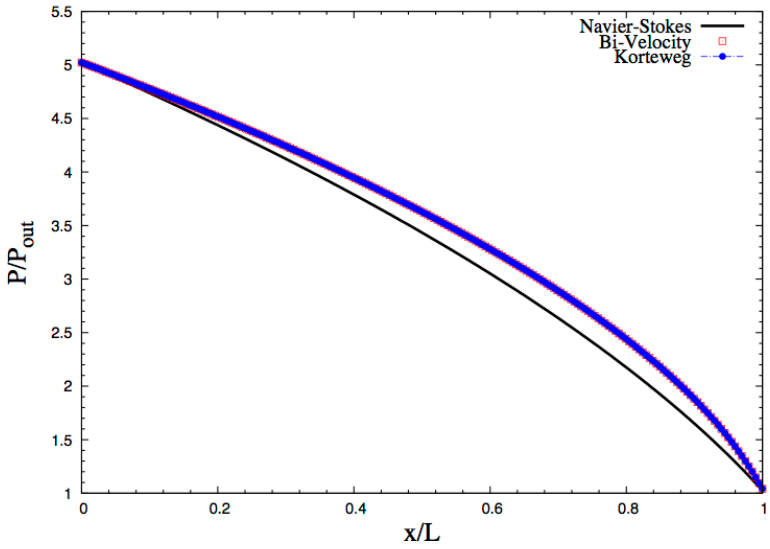

b)

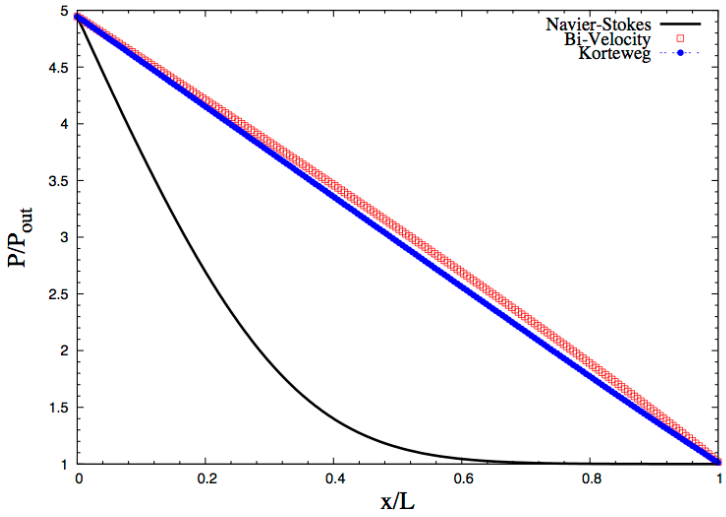

c)

Figure 5-25 Normalized pressure distribution along the steamwise direction for various Knudsen numbers a) Kn = 0.043, b) Kn = 1.07 c) Kn = 80.7

Figure 5.25 presents the normalized pressure distribution along the streamwise direction for the Bi-velocity, Korteweg and Navier-Stokes with velocity and temperature jump boundary conditions. The convex curvature is captured by the three methods identically for the low Knudsen number. Difference between Bi-velocity and Korteweg is insignificant across the Knudsen number range. This may be explained by the fact that both method constitutive equations for the shear stresses contain the density gradient capillarity effects. For a higher Knudsen number that corresponds to the free molecular regime (Kn = 80) Navier-Stokes profile may be described as unphysical compared to the other two models that appear to predict a rather monotonic variation in the profiles from the low to the higher Knudsen number.

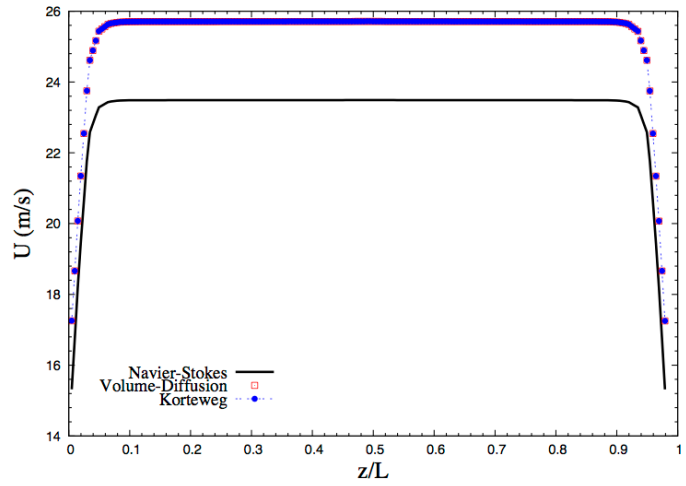

a)

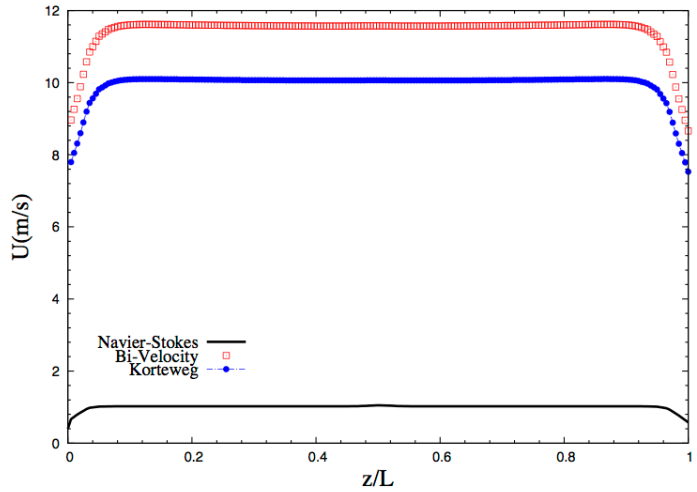

b)

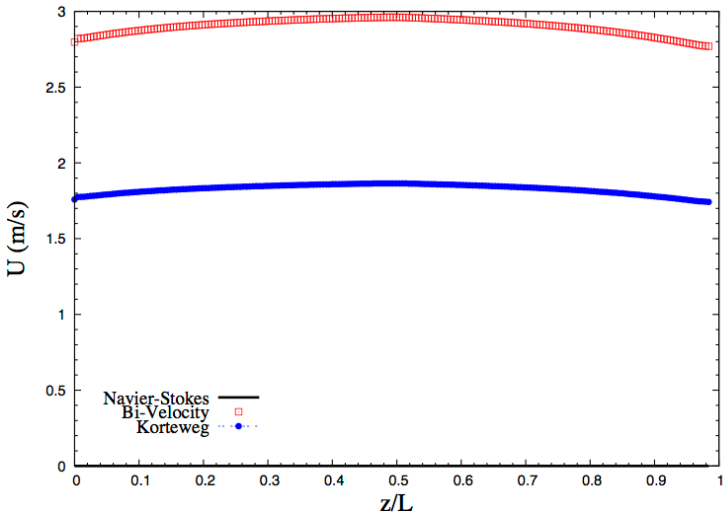

c)

Figure 5-26 Velocity Profile alon the microchannel in cross section of the flow direction a) Kn = 0.043, b) Kn = 1.07 and c) Kn = 80.7

Figure 5.26 shows velocity profile in a cross-section of the stream wise direction in the position where the flow is fully developed for all methods. For Kn = 0.043 the mass velocity as derived from the Navier-Stokes has a minor difference of 2.5m/s from Bi-velocity and Korteweg mass velocity. The velocity profile differs from the parabolic shape expected from a pure hydrodynamic regime pressure-driven flow. The mass velocity decreases as the Knudsen number increases and vanishes for the Navier-Stokes at higher Knudsen number (Figure 5.26c) which is consistent with the no mass flow predicted by this model at higher Knudsen number. Bi-velocity predicts the highest mass velocity at the highest Knudsen number which is in agreement with the mass flow rate plotted in Figure 5.24.

5.4. Computational Efficiency

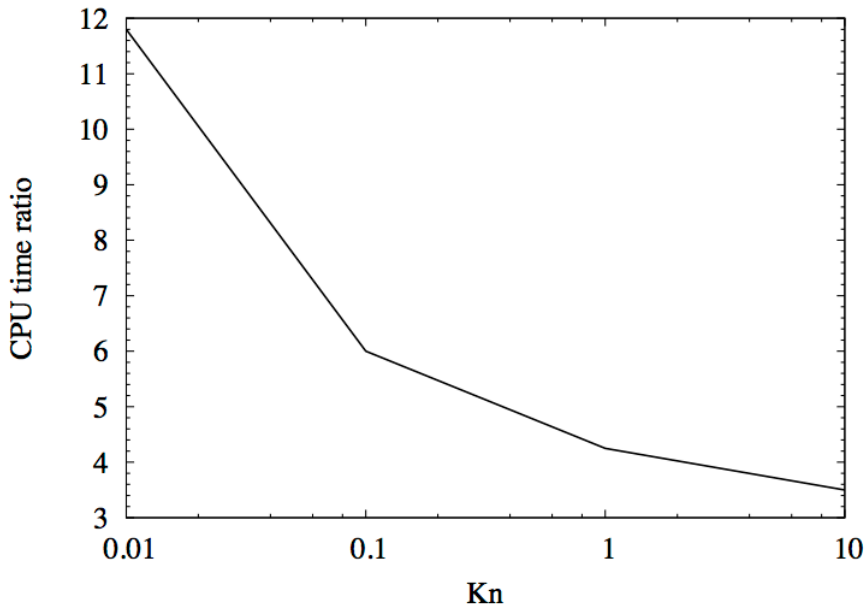

Figure 5-27 Comparison between DSMC and bi-velocity in CPU ratio with respect to Knudsen number

5.5. Summary

In this chapter, microscale rarefied gas flows have been undertaken within *HWrhoCentralFoam* and *CCrhoCentralFoam* against numerical, experimental and analytical solutions. From the present results, we have identified a very good agreement for the temperature profile in high Knudsen numbers for the *HWrhoCentralFoam.* In addition, the energetic heat flux $\boldsymbol{J_u}$ has been proved to capture anti-Fourier heat transfer under non-equilibrium conditions. For very low Knudsen numbers the heat flux from Navier-Stokes,

Bi-Velocity and DSMC agree, as it was expected. For higher Knudsen number the heat flux from Navier-Stokes still predicts a hot-to-cold heat transfer following the Fourier law. For Kn > 1 the DSMC and Volume Diffusion show a clear heat transfer from cold-to-hot.

In general Volume Diffusion appears to account of non-local equilibrium effects where Navier-Stokes fails. Volume Diffusion model predicts temperature distribution for the various Knudsen number in general agreement with DSMC for the heat transfer cavity case. While the unconventional cold-to-hot heat transfer is confirmed in high Knudsen numbers, it follows the second law of thermodynamics as the Volume Diffusion theory distinguishes between entropic heat flux and energetic heat flux. Knudsen layer is observed for all the cases while Navier-Stokes fails to predict it. A numerical overshoot related to the use of the simplified form of the volume diffusion model is observed.

Different heat transfer processes are observed for the mixed-convection problem. Volume velocity dominates the prediction of non-equilibrium effects in the upper left and right corners at high Knudsen number and affects temperature profiles across the cavity. Unconventional cold-to-hot heat transfer processes are predicted in the corners at transition regime.

In the absence of experimental data DSMC served as the benchmark method for the new proposed models. However, for the microchannel pressure driven flow all the proposed models were compared with experimental and analytical data. Results illustrate that Bi-velocity (and *HWrhoCentralFoam)* can show excellent agreement with experimental data for the whole range of Knudsen number as of the dimensionless mass flow rate. In addition, the capture of the Knudsen paradox confirms the Bi-velocity theory can capture non-equilibrium effects. Korteweg and *CCrhoCentralFoam* can show good agreement for up to Kn = 1 and provide better results than standard Navier-Stokes.

Chapter 6

6.Conclusions and Future Work

6.1. Conclusions

The development of two hydrodynamics models, Bi-velocity and Korteweg, were presented in the thesis. Two computational fluid dynamics (CFD) toolboxes in the open source software OpenFOAM were developed. The two CFD solvers are based on the pre-existing density based solver called *rhoCentralFoam.* The bi-velocity hydrodynamics solver is called *HWrhoCentralFoam* and has taken its name from the Institution that hold the current research group. The Korteweg type like solver is called *CCrhoCentralFoam* and it has taken its name from the Initials of the author and developer. Both hydrodynamic solvers were presented along with new boundary conditions mounted for each model. The two new hydrodynamics models were compared with the direct simulation Monte Carlo (DSMC) method results that are obtained through in-house DSMC solver, results available in the literature and experimental data where available. The current thesis focused on the theoretical and computational development of new theories as well as the benchmark of them (from computational perspective).

Furthermore, this thesis presented an introduction to Korteweg type hydrodynamics as presented through the past century. In addition, we have outlined the pros and cons about presenting extended hydrodynamics models that remain purely in the continuum description and are able to capture some non-equilibrium effects. From the computational time perspective, several parallel efficiency studies were run. We have used the High-Performance Computer (HPC) facility, Archie-West for over 100000 CPU hours as for the DSMC results and the *dsmcFoam* solver was found to be a very efficient but can mainly be used in HPC especially for complex cases (porous medium) on average. As for the proposed continuum based solvers (*HWrhoCentralFoam* and *CCrhoCentralFoam)* the

same cases with *dsmcFoam* were run but on standalone machines. In contrast with *dsmcFoam* we found that the continuum methods algorithms (*HWrhoCentralFoam* and *CCrhoCentralFoam)* can run effectively and efficiently in standalone machine with converged results in few hours.

Results illustrate that good agreement for micro and nano-scale test cases with results compared with DSMC and experimental data. Our numerical results were found to be in excellent agreement as for the heat flux, temperature and mass flow rate with the compared data. However, for certain problems volume diffusivity coefficient in the Bi-velocity model was found to diverge the numerical results. Through benchmark with DSMC and experimental data we were able to quantify this coefficient for consistent results in several cases and for the whole range of Knudsen number.

For rarefied gas flows the unconventional cold-to-hot heat transfer is confirmed in high Knudsen numbers, which follows the second law of thermodynamics as the Bi-velocity theory distinguishes between entropic heat flux and energetic heat flux. Knudsen layer is observed for Bi-velocity while Navier-Stokes fails to predict it.

The benchmark of the numerical method and comparison with experimental data show the ability and consistency of the present theories. The numerical approach also offers probably excellent analysis of rarefied gases, like Boltzmann equation. Generally, Korteweg and Bi-velocity equations remain inside continuum mechanics and at the same time can capture non-equilibrium effects in non-continuum regime. Based on rarefied gas flow in a microchannel Korteweg shows better performance than the standard Navier-Stokes equations and agrees well with experimental data for up to a Knudsen number near unity. Bi-velocity model is able to give excellent agreement with the experimental data as for the non-dimensional mass flow rate for the whole range of Knudsen number in the numerical method even for the free molecular regime. One of the non-equilibrium effect that is captured from the Bi-velocity model is the *Knudsen paradox.* Bi-velocity equations have shown the paradox at Knudsen number near unity as observed by other researchers. Bi-velocity model shows admirable results for the pressure and velocity distributions for the micro channel configuration. Korteweg model extends Navier-Stokes validity.

In general, the continuum based methods are extensively faster than the particle method in the whole range of Knudsen number. Results for the micro and nano scale problems illustrate that Bi-velocity model can give at least good results on average 10 times faster than DSMC. Especially, convergence of the Bi-velocity and Korteweg algorithm was found to occur very quickly in all regimes for several cases. The accuracy of the converged flow properties was found to depend on grid and cell size. This is in contrast with DSMC, where

the microscopic and macroscopic flow properties are proportional to the cell size and the time-step.

Beside our work in development of extended hydrodynamics models for rarefied gas flows we apply such method for flows in tight porous media. The type of porous medium where the flow is rarefied is in tight and shale gas reservoirs where gas flow fail in the transition and slip flow regime. To investigate the rarefied gas flow through porous medium with numerical simulations (DSMC) the microcomputer tomography (micro-CT) technology was used for the 3D representation of the rock as computational domain. According to our knowledge this was the first time that the DSMC method was used directly on micro-CT technology images. This technology, enable us to illustrate in precise way the rock where rarefied gas flow occurs. The resolution of such micro-CT rock image that was used is in the scale of some μm. Firstly, we presented a DSMC study for 3D Berea sandstone for a pressure-driven flow of methane (CH_4) at different Knudsen numbers, within the slip and transition regimes. Due to large number of computational cells, the simulations were run on a High-Performance Computer for this case as well. For a porous media with such a complex geometry, it showed that Knudsen number plays an important role for the velocity profile. The profile of the pressure and temperature show some similarities and for the three different cases. For all the Knudsen numbers, the parabolic shape is observed at the inlet and the middle of the channel. As the Knudsen number increases the parabolic shape become non-obvious at the outlet. The Klinkenberg effect is also investigated for the different Knudsen numbers for a first time with the DSMC method.

Based on the interest for tight porous we perform an in depth analytical solution for a consistent prediction of permeability in such type of reservoirs. Various correlations for quantifying the mean free path of a gas were summarized and compared in this work. Using experimental data provided by Cooper *et al.*, and Dadzie & Brenner mass flow rate theoretical model, a new alteration factor has been introduced for the mean free path to characterize gas flow in nanotubes/shale-strata in the transition flow region. The effects of this modification were explored using Knudsen number dependent permeability correlations postulated by previous investigators. Results demonstrate a considerable discrepancy in the permeability numerical value.

6.2. Future Work

The developed hydrodynamic models and algorithms as well as results from porous medium simulation that are developed and presented in this thesis shows the opportunity to carry out some future suggested work as:

Development of new hydrodynamic model as a combination of Korteweg and bi-velocity theory.

Further analysis and new boundary conditions for the hydrodynamics models.

Application of micro-CT porous media images in planetary sciences using DSMC and comparison other continuum models.

New permeability law that will be derived from bi-velocity model and non standard Navier-Stokes as Darcy law. This will enable to compare it with experimental data and permeability obtained through micro-CT. In such occasion, we may be able to understand we in our days' unconventional gas reservoirs tend to produce more than it was expected. Is that connected with Knudsen paradox? For a complete evaluation, we suggest calculating permeability with DSMC.

This work serves as a basis for further analysis of rarefied gas flows through tight porous media. In this work, we limited our analysis only on the Berea sandstone in order to investigate the flow behaviour. In order to establish a fundamental understanding of gas flow through tight porous media, more simulations on sandstone samples are required.

Finally, and most important, the application of hydrodynamics models in such type of porous media will enable possibly faster (than discrete methods) and accurate results. This will enable us to apply them in the scale of kilometres where natural gas reservoirs usually are.

References:

1. Barber, R.W. and D.R. Emerson. *A numerical investigation of low Reynolds number gaseous slip flow at the entrance of circular and parallel plate microchannels*. in *ECCOMAS Computational Fluid Dynamics Conference, Swansea, Wales, UK*. 2001.
2. Barber, R.W. and D.R. Emerson, *Challenges in modeling gas-phase flow in microchannels: from slip to transition.* Heat Transfer Engineering, 2006. **27**(4): p. 3-12.
3. Maxwell, J.C., *On Stresses in Rarefied Gases Arising from Inequalities of Temperature.* Proceedings of the Royal Society of London, 1878. **27**(185-189): p. 304-308.
4. Hilbert, D., *Mathematical problems.* 1900.
5. Shen, C., *Rarefied gas dynamics: fundamentals, simulations and micro flows*. 2006: Springer.
6. Boltzmann, L.E., *Analytischer Beweis des 2. Hauptsatzes der mechanischen Wärmetheorie aus den Sätzen über das Gleichgewicht der lebendigen Kraft*. 1871: K. Akad. der Wissensch.
7. Bird, G., et al., *Theoretical and experimental study of rarefied supersonic flows about several simple shapes.* AIAA Journal, 1968. **6**(12): p. 2388-2394.
8. Gallis, M.A., *DSMC Simulations in Support of the STS-107 Accident Investigation*. 2005, DTIC Document.
9. Grad, H., *On the kinetic theory of rarefied gases.* Communications on pure and applied mathematics, 1949. **2**(4): p. 331-407.
10. Agarwal, R.K., K.-Y. Yun, and R. Balakrishnan, *Beyond Navier–Stokes: Burnett equations for flows in the continuum–transition regime.* Physics of Fluids (1994-present), 2001. **13**(10): p. 3061-3085.
11. Struchtrup, H. and M. Torrilhon, *Regularization of Grad's 13 moment equations: derivation and linear analysis.* Physics of Fluids (1994-present), 2003. **15**(9): p. 2668-2680.
12. Mohammadzadeh, A., et al., *Thermal and second-law analysis of a micro- or nanocavity using direct-simulation Monte Carlo.* Phys Rev E Stat Nonlin Soft Matter Phys, 2012. **85**(5 Pt 2): p. 056310.
13. Gu, X.-j. and D.R. Emerson, *A high-order moment approach for capturing non-equilibrium phenomena in the transition regime.* Journal of Fluid Mechanics, 2009. **636**: p. 177-216.
14. Comeaux, K.A., D.R. Chapman, and R.W. MacCormack. *An analysis of the Burnett equations based on the second law of thermodynamics*. in *AIAA, Aerospace Sciences Meeting and Exhibit, 33 rd, Reno, NV*. 1995.
15. Bobylev, A., *Instabilities in the Chapman-Enskog expansion and hyperbolic Burnett equations.* Journal of statistical physics, 2006. **124**(2-4): p. 371-399.
16. García-Colín, L.S., R.M. Velasco, and F.J. Uribe, *Beyond the Navier–Stokes equations: Burnett hydrodynamics.* Physics Reports, 2008. **465**(4): p. 149-189.
17. Poisson, S.D., *Nouvelle théorie de l'action capillaire*. 1831: Bachelier père et fils.
18. Gibbs, J.W., *On the equilibrium of heterogeneous substances.* American Journal of Science, 1878(96): p. 441-458.
19. van der Waals, J.D., *Thermodynamische theorie der capillariteit in de onderstelling van continue dichtheidsverandering, door JD Van der Waals*. 1893: J. Müller.

20. Korteweg, D.J., *Sur la forme que prennent les équations du mouvement des fluides si l'on tient compte des forces capillaires causées par des variations de densité considérables mais continues et sur la théorie de la capillarité dans l'hypothese d'une variation continue de la densité.* Archives Néerlandaises des Sciences exactes et naturelles, 1901. **6**(1): p. 6.
21. Hadjiconstantinou, N.G., *Analysis of discretization in the direct simulation Monte Carlo.* Physics of Fluids (1994-present), 2000. **12**(10): p. 2634-2638.
22. Colin, S., *Rarefaction and compressibility effects on steady and transient gas flows in microchannels.* Microfluidics and Nanofluidics, 2005. **1**(3): p. 268-279.
23. Brenner, H. and J.R. Bielenberg, *A continuum approach to phoretic motions: Thermophoresis.* Physica A: Statistical Mechanics and its Applications, 2005. **355**(2): p. 251-273.
24. Cipolla, C.L., et al., *Reservoir Modeling in Shale-Gas Reservoirs.* 2010.
25. McNaught, A.D., *IUPAC Compendium of Chemical Terminology: The Gold Book*. 2005: International Union of Pure and Applied Chemistry.
26. Javadpour, F., D. Fisher, and M. Unsworth, *Nanoscale Gas Flow in Shale Gas Sediments.* 2007.
27. Shi, J., et al., *Diffusion and Flow Mechanisms of Shale Gas through Matrix Pores and Gas Production Forecasting*. 2013, Society of Petroleum Engineers.
28. Cercignani, C., *Rarefied gas dynamics: from basic concepts to actual calculations*. Vol. 21. 2000: Cambridge University Press.
29. Lv, Q., et al., *Determining the intrinsic permeability of tight porous media based on bivelocity hydrodynetics.* Microfluidics and Nanofluidics, 2014. **16**(5): p. 841-848.
30. Song, B. and C.A. Ehlig-Economides. *Rate-Normalized Pressure Analysis for Determination of Shale Gas Well Performance*. in *North American Unconventional Gas Conference and Exhibition*. 2011. Society of Petroleum Engineers.
31. Swami, V., C.R. Clarkson, and A. Settari, *Non-Darcy Flow in Shale Nanopores: Do We Have a Final Answer?* 2012, Society of Petroleum Engineers.
32. Darabi, H., et al., *Gas flow in ultra-tight shale strata.* Journal of Fluid Mechanics, 2012. **710**: p. 641-658.
33. Tsien, H.-S., *Superaerodynamics, Mechanics of Rarefied Gases.* Journal of the Aeronautical Sciences (Institute of the Aeronautical Sciences), 1946. **13**(12): p. 653-664.
34. Smoluchowski von Smolan, M., *Über wärmeleitung in verdünnten gasen.* Annalen der Physik, 1898. **300**(1): p. 101-130.
35. Bird, G.A., *Molecular gas dynamics and the direct simulation of gas flows*. Oxford engineering science series. 1994, Oxford: Oxford University Press.
36. Maxwell, J.C., *On the stability of the motion of Saturn's rings*. 1859.
37. Chapman, S. and T.G. Cowling, *The mathematical theory of non-uniform gases: an account of the kinetic theory of viscosity, thermal conduction and diffusion in gases*. 1970: Cambridge university press.
38. EIA, U., *Annual energy outlook 2016.* US Energy Information Administration, Washington, DC, 2016.
39. Zhang, P., et al., *Micro/nano-pore network analysis of gas flow in shale matrix.* Scientific reports, 2015. **5**.
40. Klinkenberg, L.J., *The permeability of porous media to liquids and gases.* Drilling and production practice, 1941.
41. Greenshields, C.J., et al., *Implementation of semi-discrete, non-staggered central schemes in a colocated, polyhedral, finite volume framework, for high-speed viscous flows.* International journal for numerical methods in fluids, 2010. **63**(1): p. 1-21.

42. Bird, G.A., *Approach to translational equilibrium in a rigid sphere gas.* Physics of Fluids (1958-1988), 1963. **6**(10): p. 1518-1519.
43. Oran, E., C. Oh, and B. Cybyk, *Direct simulation monte carlo: Recent advances and applications 1.* Annual Review of Fluid Mechanics, 1998. **30**(1): p. 403-441.
44. Bird, G., *Breakdown of translational and rotational equilibrium in gaseous expansions.* AIAA journal, 1970. **8**(11): p. 1998-2003.
45. Bird, G., *The structure of normal shock waves in a binary gas mixture.* Journal of Fluid Mechanics, 1968. **31**(04): p. 657-668.
46. Borgnakke, C. and P.S. Larsen, *Statistical collision model for Monte Carlo simulation of polyatomic gas mixture.* Journal of computational Physics, 1975. **18**(4): p. 405-420.
47. Bird, G., *Perception of numerical methods in rarefied gasdynamics.* Progress in Astronautics and Aeronautics, 1989. **117**: p. 211-226.
48. Pham-Van-Diep, G., D. Erwin, and E. Muntz, *Nonequilibrium molecular motion in a hypersonic shock wave.* Science, 1989. **245**(4918): p. 624-626.
49. Goldsworthy, M.J., *A GPU–CUDA based direct simulation Monte Carlo algorithm for real gas flows.* Computers & Fluids, 2014. **94**(0): p. 58-68.
50. Maxwell, J.C., *On stresses in rarified gases arising from inequalities of temperature.* Philosophical Transactions of the royal society of London, 1879: p. 231-256.
51. Cercignani, C. and M. Lampis, *Kinetic models for gas-surface interactions.* Transport Theory and Statistical Physics, 1971. **1**(2): p. 101-114.
52. Lord, R. *Application of the Cercignani-Lampis scattering kernel to direct simulation Monte Carlo calculations*. in *Proc. of 17th Int. Symp. on Rarefied Gas Dynamics*. 1991.
53. Scanlon, T.J., et al., *An open source, parallel DSMC code for rarefied gas flows in arbitrary geometries.* Computers & Fluids, 2010. **39**(10): p. 2078-2089.
54. Hadjiconstantinou, N.G., et al., *Statistical error in particle simulations of hydrodynamic phenomena.* Journal of computational physics, 2003. **187**(1): p. 274-297.
55. Breuer, K.S., E.S. Piekos, and D.A. Gonzales. *DSMC simulations of continuum flows*. in *AIAA, Thermophysics Conference, 30 th, San Diego, CA*. 1995.
56. Fan, J. and C. Shen, *Statistical simulation of low-speed rarefied gas flows.* Journal of Computational Physics, 2001. **167**(2): p. 393-412.
57. Sone, Y., *Kinetic theory and fluid dynamics*. 2012: Springer Science & Business Media.
58. Crookes, W., *Experimental Contributions to the Theory of the Radiometer.--Preliminary Notice.* Proceedings of the Royal Society of London, 1876. **25**(171-178): p. 303-314.
59. Serrin, J. and J. Dunn, *On the thermodynamics of interstitial working.* Arch. Rat. Mech. Anal, 1985. **88**(2): p. 95-133.
60. Epstein, P.S., *Zur theorie des radiometers.* Zeitschrift für Physik, 1929. **54**(7-8): p. 537-563.
61. Mehrabadi, M., S. Cowin, and M. Massoudi, *Conservation laws and constitutive relations for density-gradient-dependent viscous fluids.* Continuum Mechanics and Thermodynamics, 2005. **17**(2): p. 183-200.
62. Sone, Y., et al., *Inappropriateness of the heat-conduction equation for description of a temperature field of a stationary gas in the continuum limit: Examination by asymptotic analysis and numerical computation of the Boltzmann equation.* Physics of Fluids (1994-present), 1996. **8**(2): p. 628-638.
63. Sone, Y., S. Takata, and H. Sugimoto, *The behavior of a gas in the continuum limit in the light of kinetic theory: the case of cylindrical Couette flows with evaporation and condensation.* Physics of Fluids, 1996. **8**(12): p. 3403-3413.

64. Sone, Y., *Flows induced by temperature fields in a rarefied gas and their ghost effect on the behavior of a gas in the continuum limit.* Annual review of fluid mechanics, 2000. **32**(1): p. 779-811.
65. Brenner, H., *Is the tracer velocity of a fluid continuum equal to its mass velocity?* Physical Review E, 2004. **70**(6): p. 061201.
66. Brenner, H., *Navier–Stokes revisited.* Physica A: Statistical Mechanics and its Applications, 2005. **349**(1): p. 60-132.
67. Dadzie, S.K. and J.M. Reese, *A volume-based hydrodynamic approach to sound wave propagation in a monatomic gas.* Physics of Fluids (1994-present), 2010. **22**(1): p. 016103.
68. Dadzie, S.K. and H. Brenner, *Predicting enhanced mass flow rates in gas microchannels using nonkinetic models.* Physical Review E, 2012. **86**(3): p. 036318.
69. Brenner, H., *Fluid mechanics in fluids at rest.* Physical Review E, 2012. **86**(1): p. 016307.
70. Dadzie, S.K., *A thermo-mechanically consistent Burnett regime continuum flow equation without Chapman–Enskog expansion.* Journal of Fluid Mechanics, 2013. **716**: p. R6.
71. Christou, C., et al. *Effects of volume diffusion in heat transfer in a cavity flow in non-continuum regime*. in *AIP Conference Proceedings*. 2016. AIP Publishing.
72. Dadzie, S.K. and C. Christou, *Bi-velocity gas dynamics of a micro lid-driven cavity heat transfer subject to forced convection.* International Communications in Heat and Mass Transfer, 2016. **78**: p. 175-181.
73. Gorban, A. and I. Karlin, *Beyond Navier–Stokes equations: capillarity of ideal gas.* Contemporary Physics, 2016: p. 1-21.
74. Gorban, A.N. and I.V. Karlin, *Invariant manifolds for physical and chemical kinetics.* 2004.
75. Anderson, D. and G.B. McFadden, *A diffuse-interface description of internal waves in a near-critical fluid.* Physics of Fluids, 1997. **9**(7): p. 1870-1879.
76. Heida, M. and J. Málek, *On compressible Korteweg fluid-like materials.* International Journal of Engineering Science, 2010. **48**(11): p. 1313-1324.
77. Anderson, D.M., G.B. McFadden, and A.A. Wheeler, *Diffuse-interface methods in fluid mechanics.* Annual review of fluid mechanics, 1998. **30**(1): p. 139-165.
78. Bird, G., *Definition of mean free path for real gases.* The Physics of fluids, 1983. **26**(11): p. 3222-3223.
79. Kurganov, A. and E. Tadmor, *New high-resolution central schemes for nonlinear conservation laws and convection–diffusion equations.* Journal of Computational Physics, 2000. **160**(1): p. 241-282.
80. Christou, C. and S.K. Dadzie. *Direct Simulation Monte Carlo Method in Porous Media Through Various Knudsen Numbers*. in *SPE Reservoir Simulation Symposium*. 2015. Society of Petroleum Engineers.
81. Roy, S., et al., *Modeling gas flow through microchannels and nanopores.* Journal of applied physics, 2003. **93**(8): p. 4870-4879.
82. Amirtharaj, E., et al., *Statistical synthesis of imaging and porosimetry data for the characterization of microstructure and transport properties of sandstones.* Transport in porous media, 2011. **86**(1): p. 135-154.
83. Petrovic, A., J. Siebert, and P. Rieke, *Soil bulk density analysis in three dimensions by computed tomographic scanning.* Soil Science Society of America Journal, 1982. **46**(3): p. 445-450.
84. Dong, H. and M.J. Blunt, *Pore-network extraction from micro-computerized-tomography images.* Physical review E, 2009. **80**(3): p. 036307.

85. Raeini, A.Q., M.J. Blunt, and B. Bijeljic, *Direct simulations of two-phase flow on micro-CT images of porous media and upscaling of pore-scale forces.* Advances in Water Resources, 2014. **74**: p. 116-126.
86. Christou, C. and S.K. Dadzie, *Direct-Simulation Monte Carlo Investigation of a Berea Porous Structure.* SPE Journal, 2015.
87. OpenCFD Ltd. *OpenFOAM*. [cited 2015 20 Jul 2013]; Available from: http://www.openfoam.com/.
88. Sun, Z.-X., et al., *Proper cell dimension and number of particles per cell for DSMC.* Computers & Fluids, 2011. **50**(1): p. 1-9.
89. Firouzi, M. and J. Wilcox, *Slippage and viscosity predictions in carbon micropores and their influence on CO2 and CH4 transport.* The Journal of chemical physics, 2013. **138**(6): p. 064705.
90. Darcy, H., *Les fontaines publiques de la ville de Dijon: exposition et application*. 1856: Victor Dalmont.
91. Civan, F., *Effective Correlation of Apparent Gas Permeability in Tight Porous Media.* Transport in Porous Media, 2010. **82**(2): p. 375-384.
92. Florence, F.A., et al. *Improved permeability prediction relations for low permeability sands*. in *Rocky mountain oil & gas technology symposium*. 2007. Society of Petroleum Engineers.
93. Bird, G.A., *Definition of mean free path for real gases.* Physics of Fluids (1958-1988), 1983. **26**(11): p. 3222-3223.
94. Ewart, T., et al., *Mass flow rate measurements in a microchannel, from hydrodynamic to near free molecular regimes.* Journal of fluid mechanics, 2007. **584**: p. 337-356.
95. Cooper, S.M., et al., *Gas transport characteristics through a carbon nanotubule.* Nano Letters, 2004. **4**(2): p. 377-381.
96. Guo, C., et al. *Study on Gas Flow in Nano Pores of Shale Gas Reservoir*. in *SPE Unconventional Resources Conference Canada*. 2013. Society of Petroleum Engineers.
97. Karniadakis, G., A. Beşkök, and N.R. Aluru, *Microflows and nanoflows : fundamentals and simulation*. Interdisciplinary applied mathematics. 2005, New York, NY: Springer. xxi, 817 p.
98. Cercignani, C., *Theory and application of the Boltzmann equation*. 1975: Scottish Academic Press.
99. Xue, H., Q. Fan, and C. Shu, *Prediction of micro-channel flows using direct simulation Monte Carlo.* Probabilistic Engineering Mechanics, 2000. **15**(2): p. 213-219.
100. Mizzi, S., et al., *Effects of rarefaction on cavity flow in the slip regime.* Journal of computational and theoretical nanoscience, 2007. **4**(4): p. 817-822.
101. Akhlaghi, H., E. Roohi, and S. Stefanov, *A new iterative wall heat flux specifying technique in DSMC for heating/cooling simulations of MEMS/NEMS.* International Journal of Thermal Sciences, 2012. **59**: p. 111-125.
102. White, C., et al., *A DSMC investigation of gas flows in micro-channels with bends.* Computers & Fluids, 2013. **71**: p. 261-271.
103. Liu, H., et al., *Monte Carlo simulations of gas flow and heat transfer in vacuum packaged MEMS devices.* Applied Thermal Engineering, 2007. **27**(2–3): p. 323-329.
104. John, B., X.-J. Gu, and D.R. Emerson, *Effects of incomplete surface accommodation on non-equilibrium heat transfer in cavity flow: A parallel DSMC study.* Computers & Fluids, 2011. **45**(1): p. 197-201.
105. Akhlaghi, H., et al., *Wall heat transfer effects on the hydro/thermal behaviour of Poiseuille flow in micro/nanochannels.* Physics of Fluids (1994-present), 2014. **26**(9): p. 092002.

106. Scanlon, T., et al., *Open souce DSMC chemistry modelling for hypersonic flows.* AIAA Journal, 2014.
107. Alexander, F.J., A.L. Garcia, and B.J. Alder, *Cell size dependence of transport coefficients in stochastic particle algorithms.* Physics of Fluids (1994-present), 1998. **10**(6): p. 1540-1542.
108. John, B., X.-J. Gu, and D.R. Emerson, *Investigation of Heat and Mass Transfer in a Lid-Driven Cavity Under Nonequilibrium Flow Conditions.* Numerical Heat Transfer, Part B: Fundamentals, 2010. **58**(5): p. 287-303.
109. Gusarov, A.V. and I. Smurov, *Gas-dynamic boundary conditions of evaporation and condensation: numerical analysis of the Knudsen layer.* Physics of Fluids, 2002. **14**(12): p. 4242-4255.
110. Koplik, J. and J.R. Banavar, *Corner flow in the sliding plate problem.* Physics of Fluids (1994-present), 1995. **7**(12): p. 3118-3125.
111. Patterson, J.C. and S. Armfield, *Transient features of natural convection in a cavity.* Journal of Fluid Mechanics, 1990. **219**: p. 469-497.
112. Iwatsu, R., J.M. Hyun, and K. Kuwahara, *Mixed convection in a driven cavity with a stable vertical temperature gradient.* International Journal of Heat and Mass Transfer, 1993. **36**(6): p. 1601-1608.
113. Ghasemi, B. and S. Aminossadati, *Mixed convection in a lid-driven triangular enclosure filled with nanofluids.* International Communications in Heat and Mass Transfer, 2010. **37**(8): p. 1142-1148.
114. Cheng, T. and W.-H. Liu, *Effects of cavity inclination on mixed convection heat transfer in lid-driven cavity flows.* Computers & Fluids, 2014. **100**: p. 108-122.
115. Haworth, D. and T. Poinsot, *Numerical simulations of Lewis number effects in turbulent premixed flames.* Journal of fluid mechanics, 1992. **244**: p. 405-436.
116. Bergman, T.L. and F.P. Incropera, *Fundamentals of heat and mass transfer*. 2011: John Wiley & Sons.
117. Lv, Q., et al., *Analytical solution to predicting gaseous mass flow rates of microchannels in a wide range of Knudsen numbers.* Physical Review E, 2013. **88**(1): p. 013007.
118. Knudsen, M., *Die Gesetze der Molekularströmung und der inneren Reibungsströmung der Gase durch Röhren.* Annalen der Physik, 1909. **333**(1): p. 75-130.
119. Arlemark, E.J., S.K. Dadzie, and J.M. Reese, *An extension to the Navier–Stokes equations to incorporate gas molecular collisions with boundaries.* Journal of Heat Transfer, 2010. **132**(4): p. 041006.